

Experimental Validation of Dose Distributions Predicted by a Treatment Planning System for Complex Models

by


Gregory Allen Gallant
B.Sc., University of Alberta, 1993

A Thesis Submitted in Partial Fulfillment of the
Requirements for the Degree of


MASTER OF APPLIED SCIENCE

in the Department of Electrical and Computer Engineering


We accept this thesis as conforming
to the required standard




Dr. J. Scrimger, Supervisor (Department of Electrical and Computer Engineering)



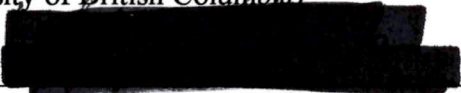
Dr. M. Stuchly, Co-Supervisor (Department of Electrical and Computer Engineering)



Dr. G.R. Mason, Outside Member (Department of Physics and Astronomy)



Dr. C. Ludgate, Additional Member (Department of Surgery, Faculty of Medicine,
University of British Columbia)



Dr. L.P. Robertson, External Examiner (Department of Physics and Astronomy)

© Gregory Allen Gallant, 1995
University of Victoria

All rights reserved. This Thesis may not be reproduced in whole or in part, by photocopy or other means, without the permission of the author.

Supervisors: Dr. J. Scrimger and Dr. M. Stuchly


ABSTRACT


The trend towards dose escalation in radiation therapy creates the need for non-coplanar beam arrangements to help minimize healthy tissue morbidity in the proximity of treatment volumes. Treatment planning software packages are able to generate external beam non-coplanar isodose distributions, but this aspect of the software available in this centre has not been experimentally verified.


Kodak XV film was used to measure the relative dose within various tissue equivalent phantoms for comparison with the distributions predicted by the G.E. Target treatment planning software. The results confirm that Target is able to predict the isodose distribution for coplanar and non-coplanar beams incident on patient equivalent phantoms containing relatively large, semi-infinite inhomogeneities well enough to warrant its implementation into routine clinical use. However, we have found that Target may not be able to adequately predict dose distributions around smaller inhomogeneous inclusions. Further work will be required to investigate this possibility.


Key Words: Radiation, Treatment Planning, Dosimetry, Film Dosimetry, Conformal Therapy

Examiners:


Dr. J. Scrimger, Supervisor (Department of Electrical and Computer Engineering)


Dr. M. Stuchly, Co-Supervisor (Department of Electrical and Computer Engineering)


Dr. G. R. Mason, Outside Member (Department of Physics and Astronomy)


Dr. C. Ludgate, Additional Member (Department of Surgery, Faculty of Medicine, University of British Columbia)



Dr. L.P. Robertson, External Examiner (Department of Physics and Astronomy)

TABLE OF CONTENTS

ABSTRACT	ii
TABLE OF CONTENTS	iii
LIST OF TABLES	v
LIST OF FIGURES	vi
ACKNOWLEDGEMENTS	xiv
1. INTRODUCTION	1
2. GENERAL BACKGROUND	3
2.1 External Beam Radiation Therapy	3
2.2 Treatment Planning	9
3. TREATMENT PLANNING SYSTEM AND GENERAL ELECTRIC TARGET 2 ALGORITHMS	10
3.1 The Milan/Bentley Photon Beam Model	10
3.2 Corrections for Curvature, Obliquity and SSD	14
3.3 Dose Calculations for Multiple and Non-Coplanar Beam Arrangements	19
3.4 Inhomogeneity Corrections	20
3.4.1 Equivalent Path Length Corrections	23
3.4.2 Power Law Corrections	25
3.4.3 Equivalent Tissue Air Ratio (ETAR) Method	27
3.4.4 Other Correction Methods	29
4. FILM DOSIMETRY	30
4.1 Fundamentals	30
4.2 Optical Density Measurements	31
5. EXPERIMENTAL METHODS AND MATERIALS	35
5.1 Film Calibration	35
5.2 Phantoms	37
5.3 Target Generated Dose Distributions	43
6. ERROR ANALYSIS	45
6.1 Film Errors	45
6.1.1 Calibration Curve Errors	45
6.1.2 Scanner Errors	47
6.1.3 Reproducibility Errors	47
6.1.4 Total Error for the Film Isodose Curves	48

6.2 Target Errors	49
6.2.1 Measured Data	49
6.2.2 Errors Associated with the Milan/Bentley Algorithm	51
6.2.2.1 CAX Errors	52
6.2.2.2 Off-Axis Profile Errors	55
6.2.2.3 Dose at a point	55
6.2.2.4 Dose Matrix Resolution	56
6.2.3 Total Error in the Target Isodose Distributions	57
7. RESULTS	59
7.1 Film Calibration	59
7.2 Phantom A: The Homogeneous Phantom	60
7.3 Phantom B: Inhomogeneous Phantom (Lung Equivalent Inclusions)	60
7.4 Phantom C: Inhomogeneous Phantom (Bone Equivalent Inclusions)	61
7.5 Phantom D: Inhomogeneous Phantom (Air Cavities)	62
8. DISCUSSION	92
9. CONCLUSIONS	96
REFERENCES	99
APPENDIX A: BEAM GENERATING HARDWARE	101
Cobalt Teletherapy Unit	102
Medical Linear Accelerator	103
APPENDIX B: TISSUE AIR RATIO DETERMINATION	108
APPENDIX C: GLOSSARY	112
APPENDIX D: COPYRIGHT PERMISSION	113

LIST OF TABLES

Table 5-1: Table identifying the tissue inhomogeneity that is included in each phantom and the materials that were used to approximate the enclosed inhomogeneity	39
Table 5-2: Treatment parameters for all coplanar measurements	42
Table 5-3: Treatment parameters for all non-coplanar measurements	42
Table 6-1: Results from statistical analysis of CAX beam data for the Vancouver Island Cancer Centre Linac 6.	54
Table 7-1: Table identifying the range of field sizes used to illustrate the validity of the film calibration curves.	60
Table 7-2: Table relating figure number to inhomogeneity correction algorithm for the coplanar beam arrangement and Phantom B.	61
Table 7-3: Table relating figure number to inhomogeneity correction algorithm for the non-coplanar beam arrangement and Phantom B.	61
Table 7-4: Table identifying the Target inhomogeneity correction algorithms used for the three field coplanar beam arrangement for Phantom C.	62
Table 7-5: Table identifying which inhomogeneity correction algorithm was used for the three field coplanar beam arrangement and Phantom D.	62

LIST OF FIGURES

Figure 2-1: Isodose curve for a 10 cm x 10 cm Cobalt beam in water.	4
Figure 2-2: Central axis depth dose curves for Cobalt (1.25 MeV) and 10 MeV photon beams. These curves were obtained using a square (10 cm x 10 cm) open field beam, perpendicularly incident on a flat water surface (depth = 0 cm).	5
Figure 2-3: Beam profile for a 10 cm x 10 cm Cobalt beam, SSD = 80 cm, Depth = 0.5 cm in water.	6
Figure 3-1: Fan line representation of a typical data set.	12
Figure 3-2: Arbitrary beam and patient outline arrangement.	15
Figure 3-3: First step of coordinate transformation: rotation and translation of the patient outline until the patient reference frame (X_{patient} , Y_{patient}) is aligned with the reference frame of the beam model (X_{beam} , Y_{beam}).	16
Figure 3-4: Final stage of transformation process.	17
Figure 3-5: Extended SSD situation showing where the user defined field size (FS_1) lies in relation to the actual field size at the patient surface (FS_2) and the relevant SSD values.	18
Figure 3-6: Illustration of a phantom containing a low density inhomogeneity. Various dose calculation points are identified.	21
Figure 3-7: Diagram illustrating three regions with different densities.	24

Figure 3-8: Diagram illustrating the power law correction method geometry for a calculation point, P, situated below three material boundaries.	27
Figure 4-1: Diagram of the Wellhofer Film Densitometer.	32
Figure 4-2: Illustration of the detector arrangement.	33
Figure 5-1: Diagram illustrating a piece of film sandwiched between pieces of solid water and irradiated by a beam.	36
Figure 5-2: Illustration of the circular phantom components and how they fit together with nylon pins to form a cylindrical phantom.	38
Figure 5-3: Diagram illustrating cross sectional detail for Phantom A.	40
Figure 5-4: Diagram illustrating the cross sectional detail for Phantom B.	40
Figure 5-5: Diagram illustrating the cross sectional detail of Phantom C.	41
Figure 5-6: Diagram illustrating the cross sectional detail for Phantom D.	41
Figure 6-1: Calibration curve for Kodak film batch number 162-20-1. Generated using the Victoria Cancer Clinic 6 MeV linear accelerator for a 10 cm x 10 cm open field perpendicularly incident on solid water at SSD = 100 cm.	46
Figure 6-2: Illustration of the typical spread in isodose curves due to film reproducibility errors. For clarity, only the 30%, 70%, and 95% isodose curves have been included. ...	50

- Figure 6-3: The complete set of CAX depth dose curves for the Vancouver Island Cancer Centre 6 MeV photon beam. 53
- Figure 7-1: Isodose curve for a 6 MV 6 cm x 6 cm open field perpendicularly incident on solid water at SSD = 100 cm. The Target isodose distribution is indicated by the dashed lines. Film isodose distribution is indicated with solid lines. 63
- Figure 7-2: Isodose curve for a 6 MV 8 cm x 8 cm open field perpendicularly incident on solid water at SSD = 100 cm. The Target isodose distribution is indicated by the dashed lines. Film isodose distribution is indicated with solid lines. 64
- Figure 7-3: Isodose curve for a 6 MV 12 cm x 12 cm open field perpendicularly incident on solid water at SSD = 100 cm. The Target isodose distribution is indicated by the dashed lines. Film isodose distribution is indicated with solid lines. 65
- Figure 7-4: Isodose curve for a 6 MV 15 cm x 15 cm open field perpendicularly incident on solid water at SSD = 100 cm. The Target isodose distribution is indicated by the dashed lines. Film isodose distribution is indicated with solid lines. 66
- Figure 7-5: Isodose curve for a 6 MV 20 cm x 20 cm open field perpendicularly incident on solid water at SSD = 100 cm. The Target isodose distribution is indicated by the dashed lines. Film isodose distribution is indicated with solid lines. 67
- Figure 7-6: Odd isodose distribution for Phantom A as a result of a three field coplanar arrangement. Film distribution is indicated by the solid lines. The Target distribution is identified by the dashed lines. No correction algorithm has been employed, since this phantom is homogeneous. 68

Figure 7-7: Even isodose distribution for Phantom A as a result of a three field coplanar arrangement. Film distribution is indicated by the solid lines. The Target distribution is identified by the dashed lines. No correction algorithm has been employed, since this phantom is homogeneous. 69

Figure 7-8: Odd isodose distribution for Phantom A as a result of a three field non-coplanar arrangement. Film distribution is indicated by the solid lines. The Target distribution is identified by the dashed lines. No correction algorithm has been employed, since this phantom is homogeneous. 70

Figure 7-9: Even isodose distribution for Phantom A as a result of a three field non-coplanar arrangement. Film distribution is indicated by the solid lines. The Target distribution is identified by the dashed lines. No correction algorithm has been employed, since this phantom is homogeneous. 71

Figure 7-10: Odd isodose distribution for Phantom B as a result of a three field coplanar arrangement. Film distribution is indicated by the solid lines. The Target distribution is identified by the dashed lines. The equivalent path length correction algorithm has been employed in an attempt to correct for the presence of the inhomogeneous structures. 72

Figure 7-11: Even isodose distribution for Phantom B as a result of a three field coplanar arrangement. Film distribution is indicated by the solid lines. The Target distribution is identified by the dashed lines. The equivalent path correction algorithm has been employed in an attempt to correct for the presence of the inhomogeneous structures. 73

Figure 7-12: Odd isodose distribution for Phantom B as a result of a three field coplanar arrangement. Film distribution is indicated by the solid lines. The Target distribution is identified by the dashed lines. The power law correction algorithm has been employed in an attempt to correct for the presence of the inhomogeneous structures. 74

Figure 7-13: Even isodose distribution for Phantom B as a result of a three field coplanar arrangement. Film distribution is indicated by the solid lines. The Target distribution is identified by the dashed lines. The power law correction algorithm has been employed in an attempt to correct for the presence of the inhomogeneous structures. 75

Figure 7-14: Odd isodose distribution for Phantom B as a result of a three field non-coplanar arrangement. Film distribution is indicated by the solid lines. The Target distribution is identified by the dashed lines. The equivalent path correction algorithm has been employed in an attempt to correct for the presence of the inhomogeneous structures. 76

Figure 7-15: Even isodose distribution for Phantom B as a result of a three field non-coplanar arrangement. Film distribution is indicated by the solid lines. The Target distribution is identified by the dashed lines. The equivalent path correction algorithm has been employed in an attempt to correct for the presence of the inhomogeneous structures. 77

Figure 7-16: Odd isodose distribution for Phantom B as a result of a three field non-coplanar arrangement. Film distribution is indicated by the solid lines. The Target distribution is identified by the dashed lines. The power law correction algorithm has been employed in an attempt to correct for the presence of the inhomogeneous structures. 78

Figure 7-17: Even isodose distribution for Phantom B as a result of a three field non-coplanar arrangement. Film distribution is indicated by the solid lines. The Target distribution is identified by the dashed lines. The power law correction algorithm has been employed in an attempt to correct for the presence of the inhomogeneous structures.

..... 79

Figure 7-18: Target generated isodose distributions for the power law and ETAR inhomogeneity corrections for Phantom B and a three field, coplanar beam arrangement. The solid lines represent the ETAR distribution. The dashed lines represent the Power Law distribution. 80

Figure 7-19: Target generated isodose distributions for the power law and ETAR inhomogeneity corrections for Phantom B and a three field, coplanar beam arrangement. The solid lines represent the ETAR distribution. The dashed lines represent the Power Law distribution. 81

Figure 7-20: Odd isodose distribution for Phantom C as a result of a three field coplanar arrangement. Film distribution is indicated by the solid lines. The Target distribution is identified by the dashed lines. The equivalent path correction algorithm has been employed in an attempt to correct for the presence of the inhomogeneous structures.

..... 82

Figure 7-21: Even isodose distribution for Phantom C as a result of a three field coplanar arrangement. Film distribution is indicated by the solid lines. The Target distribution is identified by the dashed lines. The equivalent path correction algorithm has been employed in an attempt to correct for the presence of the inhomogeneous structures.

..... 83

Figure 7-22: Odd isodose distribution for Phantom C as a result of a three field coplanar arrangement. Film distribution is indicated by the solid lines. The Target distribution is identified by the dashed lines. The power law correction algorithm has been employed in an attempt to correct for the presence of the inhomogeneous structures. 84

Figure 7-23: Even isodose distribution for Phantom C as a result of a three field coplanar arrangement. Film distribution is indicated by the solid lines. The Target distribution is identified by the dashed lines. The power law correction algorithm has been employed in an attempt to correct for the presence of the inhomogeneous structures. 85

Figure 7-24: Target generated isodose distributions for the power law and ETAR inhomogeneity corrections for Phantom C and a three field, coplanar beam arrangement. The solid lines represent the ETAR distribution. The dashed lines represent the Power Law distribution. 86

Figure 7-25: Target generated isodose distributions for the power law and ETAR inhomogeneity corrections for Phantom C and a three field, coplanar beam arrangement. The solid lines represent the ETAR distribution. The dashed lines represent the Power Law distribution. 87

Figure 7-26: Odd isodose distribution for Phantom D as a result of a three field coplanar arrangement. Film distribution is indicated by the solid lines. The Target distribution is identified by the dashed lines. The equivalent path correction algorithm has been employed in an attempt to correct for the presence of the inhomogeneous structures. 88

Figure 7-27: Even isodose distribution for Phantom D as a result of a three field coplanar arrangement. Film distribution is indicated by the solid lines. The Target distribution is identified by the dashed lines. The equivalent path correction algorithm has been employed in an attempt to correct for the presence of the inhomogeneous structures.

..... 89

Figure 7-28: Odd isodose distribution for Phantom D as a result of a three field coplanar arrangement. Film distribution is indicated by the solid lines. The Target distribution is identified by the dashed lines. The power law correction algorithm has been employed in an attempt to correct for the presence of the inhomogeneous structures. 90

Figure 7-29: Even isodose distribution for Phantom D as a result of a three field coplanar arrangement. Film distribution is indicated by the solid lines. The Target distribution is identified by the dashed lines. The power law correction algorithm has been employed in an attempt to correct for the presence of the inhomogeneous structures. 91

Figure A-1: Illustration of the components that make up a typical medical linear accelerator or a cobalt unit. The illustration is actually a representation of a linac, but the components are common to both linac and cobalt teletherapy units (with Antolak's permission (Antolak 1992). 101

Figure A-2: Cobalt 60 decay scheme. 102

Figure A-3: Diode gun. 105

Figure A-4: Cross sectional view of a typical linear accelerator head. 106

Figure B-1: Diagram illustrating the relevant quantities that are needed to discuss Tissue Air Ratio. 108

Acknowledgments

I would like to acknowledge some of the people who have provided support and guidance over the past couple of years. First I would like to thank my advisors Dr. John Scrimger and Dr. Maria Stuchly. Dr. Scrimger has been a mentor and a role model. His words of encouragement and advice, in conjunction with his vast knowledge of medical physics are a constant source of inspiration. Dr. Stuchly's encouragement and enthusiasm for this project is greatly appreciated. I would also like to thank her for allowing me to act as a teaching assistant for her ELEC 395 course.

Various organizations and private individuals have graciously supplied financial assistance for this project. Specifically, I would like to thank Mr. and Mrs. John Newton, Mrs. Constance Gibson, Mr. and Mrs. Peter Allan, Mr. and Mrs. Isaac, Mr. and Mrs. Huber, as well as the Norgaard Foundation. In addition, I would like to thank General Electric Medical Systems for research funding and the Vancouver Island Cancer Centre for the space and equipment to conduct this research.

There are various individuals within the clinic who's help and advise is greatly appreciated. In particular, I would like to thank the senior medical physicists Dr. Dave Linekin and Mr. Fan-Shih Chen for their willingness to describe, define and discuss various aspects of medical physics. A note of thanks is also due to the clinical electronics staff, Mr. Glen Owen, Mr. Mark Goldie, and Mr. Dave Sauter for sharing their technical expertise and taking the time to explain various devices. In addition, I would like to thank the Vancouver Island Cancer Centre machinist, Mr. John Schneider, for constructing all of the phantoms used in this project.

Finally, I would like to acknowledge my family. Without the love and support of my parents, Allen and Verna, my sister and brother-in-law, Allana and Roy, and their boys, Jarin and Mikhial, as well as the rest of the aunts, uncles and cousins that make up this clan of ours, I would not have had the courage to chase the dream.

To all of you, a very sincere thank you.

Gregg Gallant

Nov. 95

1. INTRODUCTION

In the clinical management of cancer, there exist a number of methods to treat diagnosed malignancies. These include surgery, chemotherapy, and radiation therapy. In the case of radiation therapy, patients are treated with beams of ionizing radiation. These beams are arranged in such a way that a curative tumorcidal dose is delivered to the diseased tissue while the dose delivered to the healthy tissue surrounding the malignancy is kept to a minimum.

The diseased tissue that is to be treated is commonly referred to as the target or, more precisely, the target volume. Various studies indicate that dose escalation to the target volume is warranted to improve the chances of local control of tumor growth and spread (Porter et al 1994, Benk et al 1993, Beard et al 1993, Sandler 1993, Zelefsky et al 1993, Hanks 1993, Epstein et al 1993, Armstrong et al 1993, Sandler et al 1992, Sandler et al 1992, Leibel et al 1991, Tait 1990). Unfortunately, as the dose to tumor tissue is escalated, the dose that is delivered to the healthy tissue surrounding the tumour is also increased. The amount of radiation that a healthy tissue can tolerate varies from tissue to tissue. But, once this limit has been exceeded tissue damage can result in serious consequences. In order to protect the healthy tissue, a technique termed conformal external beam radiation therapy, which will be described in detail below, is employed for administering treatment. Generally, conformal therapy techniques make use of various beam shaping devices and complex beam arrangements to help minimize the amount of radiation that the healthy tissue is exposed to during the course of treatment. The goal of this technique is to “conform” the radiation to the target. Traditional conformal techniques, using various block and wedge combinations for coplanar beams, have been used successfully for some time.

The further development of conformal techniques requires that the beam arrangement repertoire be expanded to include non-coplanar arrangements. Although the treatment planning software packages available today are able to generate such plans, but the dose deposition patterns predicted by the algorithms have not been experimentally verified.

This thesis presents the work that has been done to experimentally investigate the validity of the external beam coplanar and non-coplanar aspects of a commercially available treatment planning software package. The software package studied here is the General Electric Target 2 treatment planning system. Although only a single system is investigated, it is felt that the experimental methods developed in this thesis can be applied to validate others which utilize similar algorithms.

2. GENERAL BACKGROUND

2.1. External Beam Radiation Therapy

External beam radiation therapy is one method used for the treatment of cancer. This type of therapy employs a beam of ionizing radiation, which has been generated outside of the body, to control the growth and/or spread of cancerous cells within the body. Control may be achieved by delivering a prescribed amount of energy per unit mass to the group of cells that are to be treated. The group of cells that are identified as those to be subjected to the prescribed amount of radiation are referred to as the target.

Since the target is located inside the body, radiation must pass through healthy tissue before it reaches the target. Consequently, energy is deposited along the path to, and in the area around the target. The amount and location of this deposited energy depends on several parameters. These parameters include the type of radiation, the size of the beam cross section, the presence of any beam shaping devices such as wedges or blocks, the distance that the surface of the body is placed from the source of the radiation, and the composition of the tissues that lie in the path of the radiation.

There are various types of beams that can be used for external beam radiation therapy treatment, including photons, electrons, neutrons, and heavy particles. The most common types of radiation beams used are either electrons or photons. Two types of machines that are used to generate these radiation beams are cobalt machines, which contain a source of ^{60}Co which generates photons as the cobalt decays, and linear accelerators (linacs) which are used to generate photons or electrons. Descriptions of the cobalt machine and the linac can be found in Appendix A: Beam Generating Hardware.

Treatment targets tend to be of various shapes and sizes. Consequently, beam cross sections need to be easily adjustable. Collimators are used to obtain a rectangular beam of appropriate size. Further shaping of the beam may be accomplished using wedges, blocks, or, more recently, multi-leaf collimators. All of these beam shaping devices are contained in the treatment head, located at the patient end of the treatment machines.

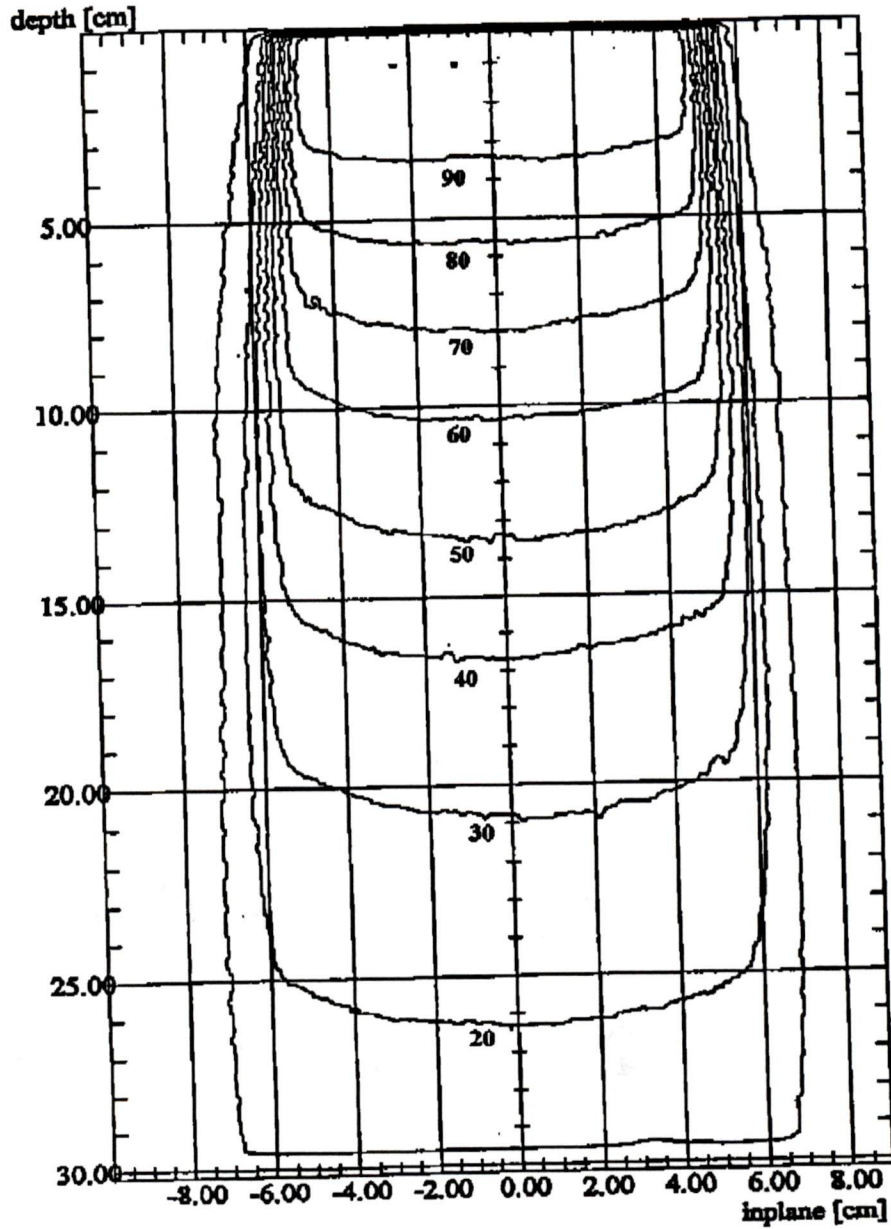


Figure 2-1: Isodose curve for a 10 cm x 10 cm Cobalt beam in water, normalized to maximum.

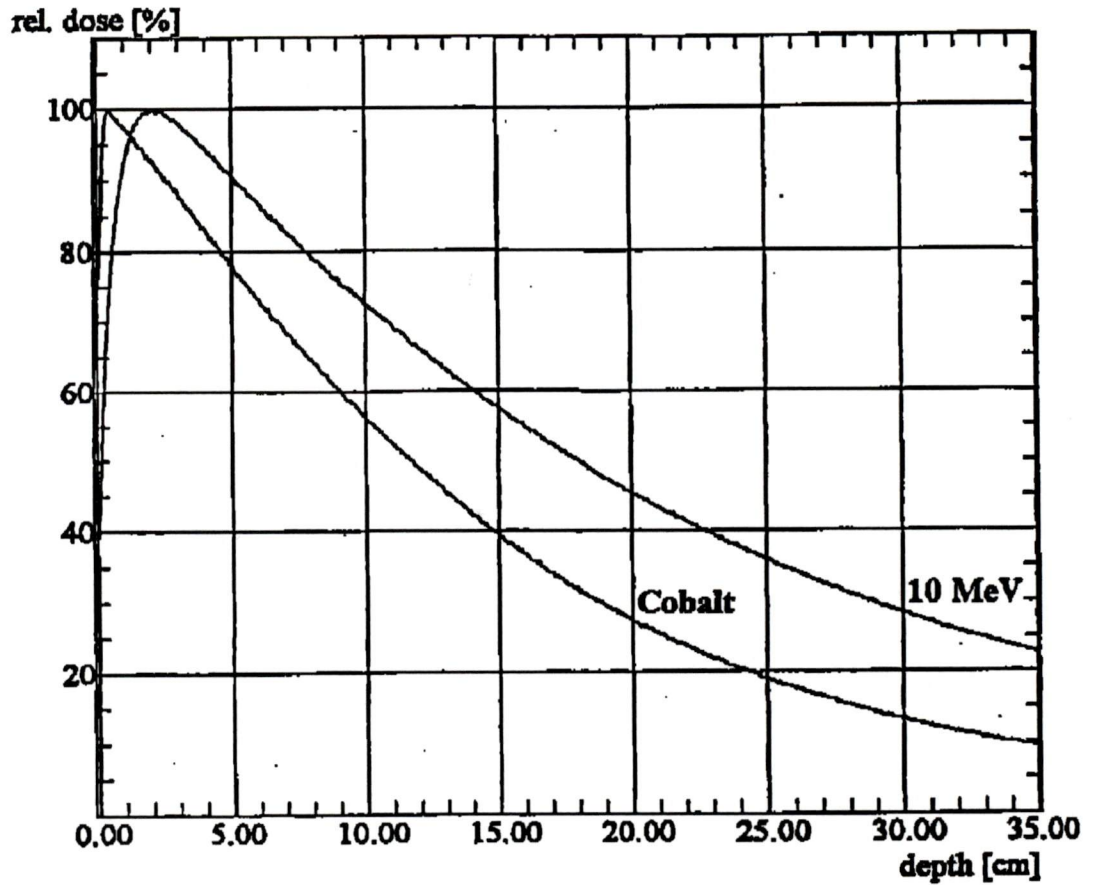


Figure 2-2: Central axis depth dose curves for Cobalt (1.25 MeV) and 10 MeV photon beams. These curves were obtained using a square (10 cm x 10 cm) open field beam, perpendicularly incident on a flat water surface.

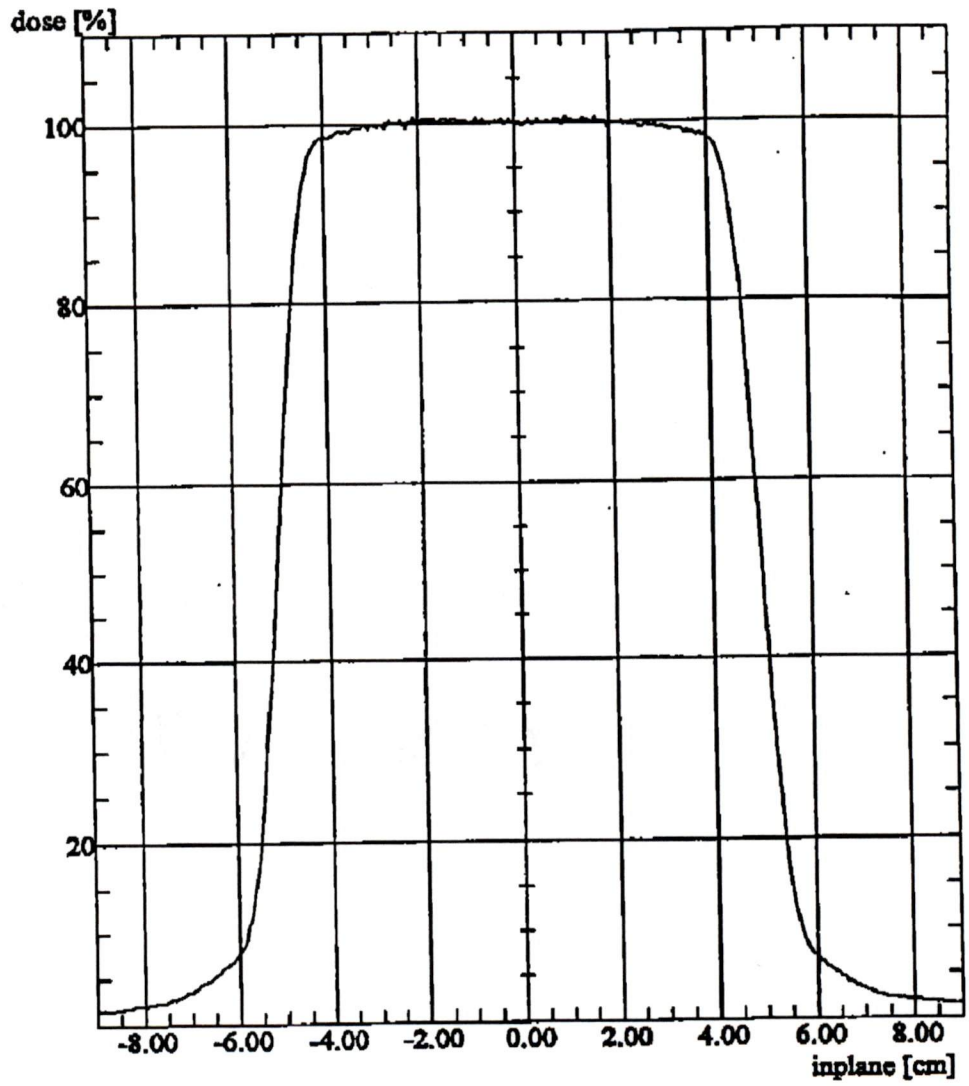


Figure 2-3: Beam profile for a 10 cm x 10 cm Cobalt beam, SSD = 80 cm, Depth = 0.5 cm in water.

As the beam of radiation enters the body, it is absorbed and scattered by the material of the body. The photons undergo Compton interactions with this material. The amount of scatter depends on the size and energy of the beam as well as the composition of the body. Consider a 10 cm x 10 cm square field generated by a cobalt machine that strikes a water surface located 80 cm from the source (source to surface distance, SSD, = 80 cm). Figure 2-1 shows the energy deposition pattern which occurs in a plane containing the central axis (CAX) of the beam. Each line in this figure represents lines of equal energy deposited per unit mass. In radiation physics, energy deposited per unit mass is referred to as dose. The unit of dose is the Gray (Gy), which is defined as 1 joule per kilogram. Since the lines in Figure 2-1 represent lines of equal dose, they are referred to as isodose lines. Isodose lines can be expressed in relative terms. This means that they are normalized to specific points. In the above case they are normalized to the points of maximum dose. If the point of maximum dose is defined to be 100%, all other points are then expressed as a percentage of the maximum, as in Figure 2-1. Notice how the beam spreads out as it penetrates the water. The spreading out of the beam is due, in part, to the above mentioned scatter, but it is mostly due to the geometrical divergence associated with the position of the source relative to the beam collimators in the head of the machine.

The energy deposition patterns can be modified by placing blocks and wedges in the field to selectively attenuate portions of the field. This provides a method of shaping the beam so that it conforms more closely to the target that is to be treated.

The dose versus depth along the central axis (CAX) of a set of isodose curves is shown in Figure 2.2. In fact, the curve labeled Cobalt, in Figure 2-2, can be constructed from the set of isodose curves shown in Figure 2-1. The curves illustrated in Figure 2-2 are referred to as central axis depth dose curves. Both sets of curves indicate that once we get past a certain depth, the amount of energy deposited falls off with depth from the surface in an exponential fashion. However, at very shallow depths, from the water surface to about 0.5 cm, for the Cobalt curve, we see that the dose delivered increases with depth. This is because energy deposition from photon beams is a two step process. At the surface, the photons will interact with the water and pass their energy on to electrons. It is these liberated electrons which then travel through the water and ultimately

deposit their energy downstream from the site of the initial interaction. The increase in dose with depth for the shallower depths is due to the fact that all of the liberated electrons travel a short distance before some of them begin to deposit their energy.

All photon beam central axis depth dose curves have the classic shape, illustrated by the ^{60}Co curve in Figure 2-2. However, the depth at which the maximum dose is achieved will vary depending on the photon energy. The depth at which the maximum dose is delivered is referred to as d_{max} . Figure 2-2 illustrates that the value of d_{max} increases with increasing photon beam energy and increasing field size. Notice that cobalt beams (1.25 MeV) have a $d_{\text{max}} = 0.5$ cm, a 10 MeV photon beam has a $d_{\text{max}} = 2.5$ cm.

Consider again Figure 2-1. If the dose values along a line that is perpendicular to the central axis are plotted against the distance from the central axis for various depths, a third set of curves characterizing the radiation beam can be plotted. A single such curve is called a beam profile. Figure 2-3 illustrates a beam profile for a 10 cm x 10 cm Cobalt beam at a depth of 0.5 cm.

Beam profiles provide an indication of the beam flatness at different depths as well as a way of examining the penumbra. Again notice that the dose values are expressed as a percentage of the maximum dose value.

Before any of the beams that can be generated are used to treat patients, it is very important to characterize the beam so that the energy deposition pattern throughout the body can be determined with confidence. This is done by measuring beam profiles and depth dose curves for representative combinations of beam size and available wedge angles. These measurements are usually done in a water phantom.

The energy deposition pattern in the water would be very much like that resulting in the human body if the body were composed entirely of water. However, inhomogeneities, such as lung and bone, alter the shape of the dose deposition pattern. There are various methods of changing the measured dose distributions due to the presence of inhomogeneities. These corrections are made as part of the treatment planning process. A detailed discussion of these methods will be deferred to the section that discusses the G.E. Target treatment planning algorithms.

2.2. Treatment Planning

Treatment planning consists of using the beam information to determine the best method of delivering a specific amount of radiation to the volume of tissue to be treated. The radiation oncologist identifies the size and location of the target volume and the total dose that is to be delivered to the target. The total amount of radiation is normally delivered in a number of fractions. The radiation oncologist also indicates the presence of any sensitive tissue which cannot be subjected to more than a certain dose. Once this information is obtained, it is the responsibility of the physics group who, with the help of computerized treatment planning software, decides the best combination of beams, beams sizes, etc. that will accomplish the goal of the treatment.

3. EXTERNAL BEAM TREATMENT PLANNING SYSTEM AND THE GENERAL ELECTRIC TARGET 2 ALGORITHMS

Generally, an external beam treatment planning software system consists of a beam characterization model and various algorithms for predicting the dose distribution that would result, within the patient, from a particular beam arrangement. The software should be able to support both electron and photon beams. The user should be allowed to define, examine and modify the data that are used to characterize the beams. Beam defining parameters such as field size, source to surface distance, the angle of incidence between the beams and the patient, as well as the position, composition and shape of any blocks or wedges that will be used to alter the beam cross section should be defined by the user. Additionally, the software should be able to accept specific patient parameters such as the various tissue densities associated with the target and the surrounding volume. Such parameters should be able to be provided to the software via a variety of imaging modalities, such as CT slices, or explicitly defined from the keyboard.

The General Electric Target 2 treatment planning software package provides the user with options that cover all of the previously mentioned external beam treatment planning requirements as well as algorithms for generating dose deposition patterns for interstitial and intracavitary brachytherapy applications.

Since this project is primarily concerned with the validation of photon beam algorithms, this section will only discuss the photon beam model and the algorithms employed by the General Electric (G.E.) Target 2 treatment planning software package.

3.1. The Milan/Bentley Photon Beam Model

The General Electric treatment planning software, known as Target, uses the Milan/Bentley method for characterizing photon beams (G.E. Target 2 Physics Manual). This model was originally developed at the Royal Marsden Hospital, UK, in the early 1970s (Milan and Bentley 1974). The Milan/Bentley model uses measured central axis depth dose curves and a series of measured beam profiles to characterize a range of beam parameters that may be required for treatment purposes. Since an unreasonable amount of

memory would be required to store all of the data required to represent all of the possible combinations of beam parameters which may arise in clinical situations, Milan and Bentley devised a method where by a minimal amount of beam data are stored for a set of beams covering the range of clinically relevant beam parameters. The beam characterization data that are stored are carefully chosen to ensure that linear interpolation between the stored data sets can be used to obtain valid beam characteristics for beams which have not been explicitly stored.

The data set for each of the stored beams represent the relative dose deposited at points on a grid which just covers the central plane of the beam. A typical Target data set consists of central axis data points as well as beam profile data points, also referred to as off-axis ratios, for five profiles. Each profile consists of 47 off axis ratios; 23 to the left and 23 to the right of the central axis value which, by definition, is assigned a value of unity. The measured profiles are chosen to correspond with the central axis points identified as 1, 5, 9, 13, and 17 (see Figure 3-1). The profile points are selected so that the off-axis distances will increase with increasing depth, to account for beam divergence. Hence, any beam data set can be thought of as a collection of divergent fan lines, as illustrated in Figure 3-1. The spacing of the data points along each of the profiles is chosen so that the 47 fan lines, if projected backwards, will intersect at the effective beam source.

In this model, data sets are only stored for square fields. If a data set is required for a rectangular field, the equivalent square field value (EQS) is determined according to:

$$EQS = \frac{2WL}{W + L} \text{ (cm)}$$

Equation 3-1

(Target Physics Manual P. A1-2)

where W is the beam width and L is the beam length. Linear interpolation is then carried out between the stored data sets to generate the appropriate set of beam data.

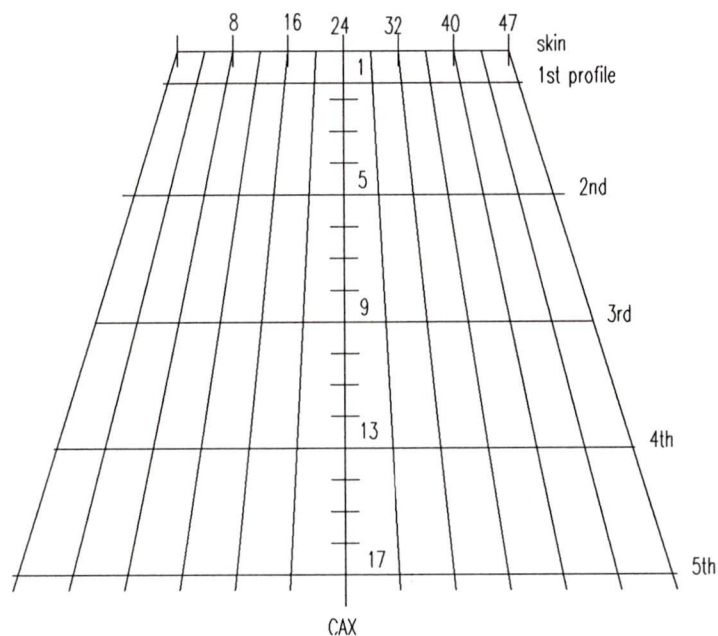


Figure 3-1: Fan line representation of a typical data set.

Seventeen central axis (CAX) values are stored for each beam. These values are obtained from equally spaced central axis depth dose measurements that extend from a depth of d_{max} to a user definable maximum depth. To be clinically useful, the maximum depth should extend to 30 or 40 cm.

The user provides central axis percent depth dose information that corresponds to the measured source to surface distance (SSD), to be used with the General Electric software. The software then converts this data to infinite SSD for storage. This is done to generalize the data set so that it is easier to use the data in a variety of SSD situations. Examples of such situations would be isocentric beam arrangements or extended SSD techniques. The conversion to infinite SSD is accomplished by removing the inverse square dependence from the data set. To do this the depth dose value associated with the measurement SSD at a particular depth, $DD(\text{SSD}, d)$, is converted to an infinite SSD value associated with the same depth, $DD(\infty, d)$, according to:

$$DD(\infty, d) = DD(SSD, d) * \left(\frac{SSD + d}{SSD + d_{\max}} \right)^2$$

Equation 3-2

(Target Physics Manual P. A1-2)

The central axis percent depth dose value that is stored for depth d , $CAX(d)$, is obtained from the infinite SSD depth dose value according to:

$$CAX(d) = \frac{DD(\infty, d)}{100} * \text{CAX value representing 100\%}$$

Equation 3-3

(Target Physics Manual P. A1-2)

CAX data points that are required for depths that lie within the stored CAX data set are found by linear interpolation. Points that lie beyond the last CAX data point are found by linear extrapolation through CAX points 16 and 17, and is valid down to a minimum dose value of about 2%.

Notice that there is no CAX information stored between the surface and the d_{\max} central axis percentage depth dose value. This region is referred to as the build-up region. To obtain CAX values within the build-up region, linear interpolation is done between a user-defined surface dose value and a modified depth value. The modified depth value is based on a cubic approximation. For example, if the CAX value is required for a depth, d , within the build-up region, a linear interpolation will be done between the user defined surface dose value and the dose value that corresponds to the modified depth, d' , where:

$$d' = d_{\max} - \frac{(d_{\max} - d)^3}{d_{\max}^2}$$

Equation 3-4

(Target Physics Manual P. A1-3)

The width of the data set is defined at the surface of the skin and should extend far enough so that the 1% dose level of the penumbral region is included. The Target software provides the user with a default table width value, based on:

$$\text{Table Width} = (\text{field width} * 1.2) + 10 \text{ mm}$$

Equation 3-5

(Target Physics Manual P. A1-3)

for field widths defined in millimeters. Although the user may define any value for the table width, it is recommended that the table widths for any given beam model increase linearly with field width. This will ensure that the linear interpolation between field sizes remains valid.

3.2. Corrections for Curvature, Obliquity, and SSD

Recall that the beam data sets represent a model for a photon beam that is normally incident on a flat water surface. We will now examine how the Target software is able to manipulate the data set to provide dose distributions in realistic situations where the beams are obliquely incident on a curved patient outline. Figure 3.2 illustrates such a situation for an arbitrary beam and patient outline arrangement. The points defining the patient outline are referenced by standard cartesian coordinates. The objective here is to illustrate how the Target software is able to manipulate the stored beam data set and the patient outline so that the dose to point Q, within the patient outline, can be obtained. Simple cartesian geometry is used to convert the stored beam data to an array of output data that will represent dose points within the patient.

Initially, the Target software defines the patient outline in terms of a set of points within a rectangular grid that is just large enough to cover the entire outline. The grid is set up so that the grid points have the same spacing in the x and y directions. The total number of grid points does not exceed 512, and is not less than 50. Relatively few dose points are used so that the dose distribution can quickly be determined and displayed on the monitor. However, the density of the grid is increased so that a total of up to 4096 points are generated for hard copy output. There is also a zoom option available that

allows the user to confine the 512 point matrix to any subset of the patient outline, increasing the dose resolution within this area.

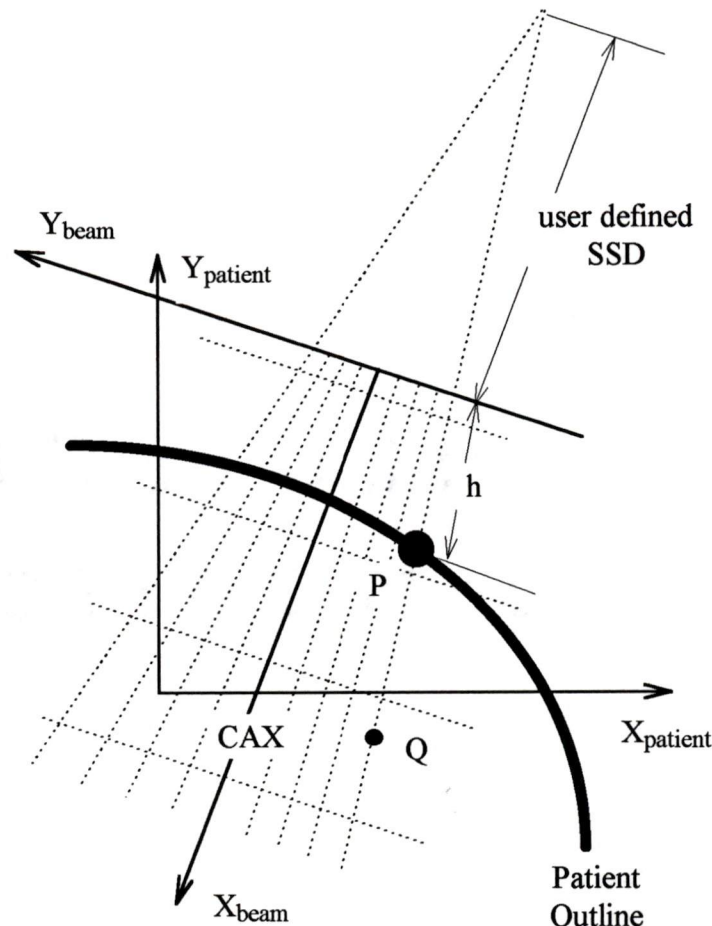


Figure 3-2: Arbitrary beam and patient outline arrangement.

Once the grid has been set up, the dose to each grid point is calculated. The key to this process is the determination of the difference between the user defined SSD and the actual SSD for every fan line. This value, h , illustrated in Figure 3-2, has to be calculated for each fan line. In order to determine the h values, the points of intersection between the fan lines and the patient outline must be determined. An example of such an intersection point, labeled P, can be seen in Figure 3-2 for an arbitrary beam and patient profile arrangement.

The first step in determining h consists of rotating and translating the patient outline, and its associated coordinate system, so that the patient axis (X_{patient} , Y_{patient}) becomes co-linear with the beam axis (X_{beam} , Y_{beam}). Figure 3-3 illustrates what has been accomplished by this translation and rotation step.

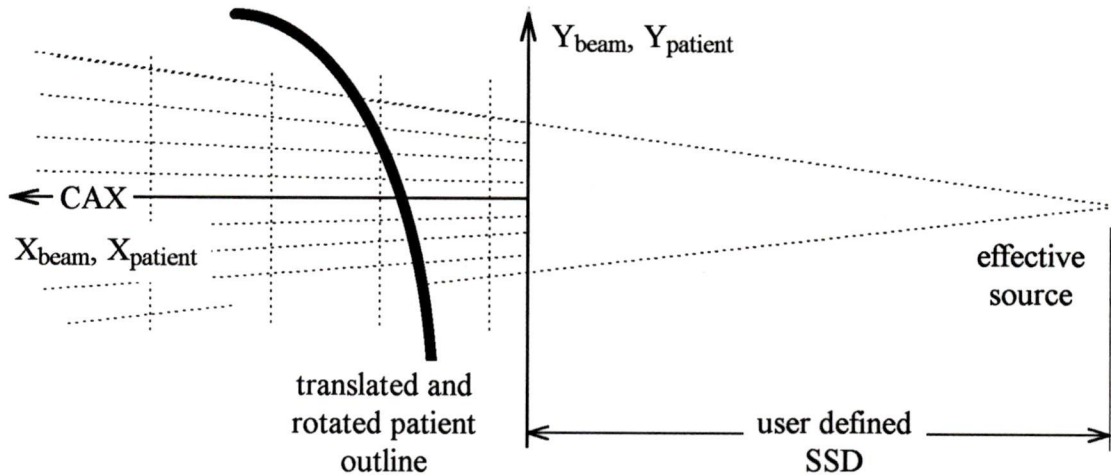


Figure 3-3: First step of coordinate transformation: rotation and translation of the patient outline until the patient reference frame (X_{patient} , Y_{patient}) is aligned with the reference frame of the beam model (X_{beam} , Y_{beam}).

Recall that the beam data points lie on fan lines that extend from the effective source. In order to facilitate the process of determining the points of intersection between the fan lines and the patient outline, the y coordinate of each patient outline point is multiplied by the divergence factor, $\frac{\text{SSD}}{\text{SSD} + x}$. This forces the fan lines into a parallel configuration, as seen in Figure 3-4.

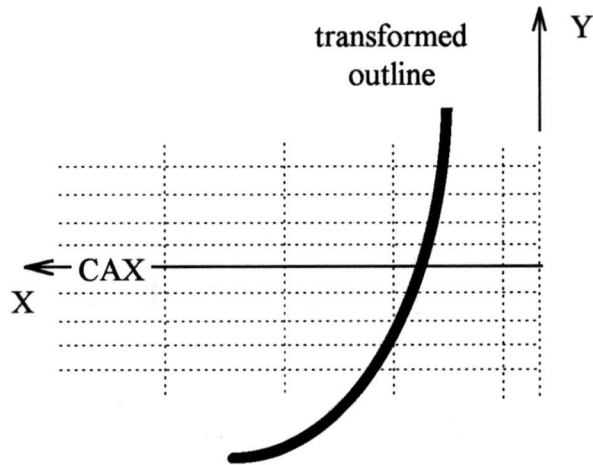


Figure 3-4: Final stage of transformation process.

At this point, the determination of the points of intersection is simply a matter of searching the patient outline y co-ordinates for points which lie on opposite sides of the fan line coordinates. The h-value is then the x co-ordinate that corresponds to the patient outline y coordinate.

Now that the points of intersection between the patient outline and the fan lines, the h-values, have been obtained, the dose at any x and y point, $D(x,y)$, within the patient outlining rectangle will be given by:

$$D(x,y) = CAX(d) * R(d,y) * \left(\frac{SSD + d_{max}}{SSD + x} \right)^2$$

Equation 3-6

(Target Physics Manual P. B1-2)

where d = depth of the point, Q , below the patient surface.

h = the difference between the actual SSD and the user defined SSD.

$x = d + h$, where x is the X coordinate.

Note that x , d , and h are parallel to the central axis.

$R(d,y)$ = two way linear interpolation between the four grid points nearest point P, using the off-axis ratios and CAX values.

$CAX(d)$ = the central axis depth dose at depth d , obtained by linear interpolation from the values stored for infinite SSD. It is the central axis data set corresponding to the field size at the patient surface, rather than the one associated with the user defined field size.

Field sizes are initially defined by the user and are usually defined to be the standard SSD value (i.e.: $SSD = 100$ cm for a linac that has an isocenter at 100 cm). However, there are situations where the actual SSD at the patient surface will not be the standard value. An example of such a situation would be extended SSD, or isocentric treatment regimes. In this situation the software will not use the beam data set that is associated with the user defined field size, but will use the appropriate data set corresponding to the actual field size at the surface. Figure 3-5 illustrates a typical extended SSD situation showing the field size, FS_1 , at the standard source to surface distance, SSD_1 , and the actual field size, FS_2 , at the patient surface where the source to surface distance is SSD_2 .

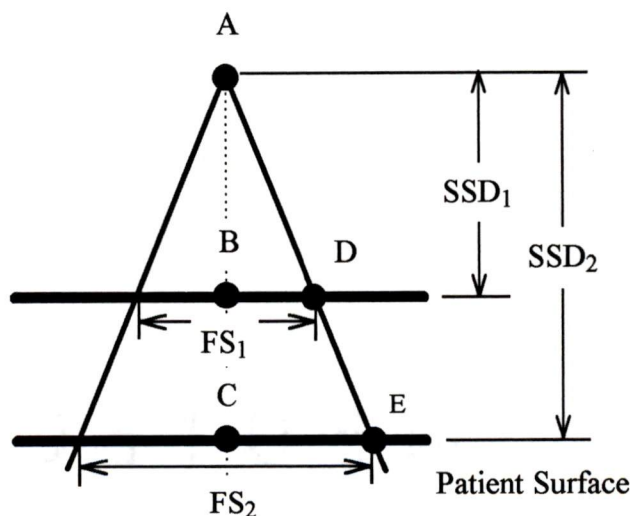


Figure 3-5: Extended SSD situation showing where the user defined field size (FS_1) lies in relation to the actual field size at the patient surface (FS_2) and the relevant SSD values.

Simple similar triangle geometry, based on triangles ABD and ACE, can be used to express the field size that the software will use, FS_2 , expressed as a function of the three other available parameters:

$$FS_2 = FS_1 * \left(\frac{SSD_2}{SSD_1} \right)$$

Equation 3-7

It is the CAX values associated with field size FS_2 that are used in the above expression for $D(x,y)$.

3.3. Dose Calculations for Multiple and Non-Coplanar Beam Arrangements

The previous section described the method that was used to arrive at the relative dose values for each point in the matrix covering the patient outline for a single beam. Recall that the relative dose at each matrix point was defined to be:

$$D(x,y) = CAX(d) * R(d,y) * \left(\frac{SSD + d_{max}}{SSD + x} \right)^2$$

Equation 3-8

(Target Physics Manual P. B1-3)

Exactly the same method is used to determine the relative dose values for the matrix when multiple co-planar beams are used. The relative dose that is contributed to each matrix point from the individual beams is determined. The total resulting dose is simply the sum of the contributions from each individual beam.

However, if the central axis of the beam does not lie in the same plane as the dose matrix, the above dose equation must be modified. The modification that is needed essentially consists of an off-axis value, $Rl(d,z)$, corresponding to the distance that the dose matrix calculation point is from the central axis, z , of the beam, at the required depth,

d. In fact, the existing beam profile data file is used to obtain this off-axis value. The relative dose value at the matrix point in this case can be obtained from:

$$D(x, y) = CAX(d) * R(d, y) * Rl(d, z) * \left(\frac{SSD + d_{max}}{SSD + x} \right)^2$$

Equation 3-9

(Target Physics Manual P.B1-3)

Note that by using this method of calculating off-axis relative dose values, the beam model assumes that the beam cross sections, for any given depth, are isotropic and can accurately be modeled using a single profile.

The G.E. Target software allows for up to ten beams from as many as three different treatment machines to be used for a single plan.

3.4. Inhomogeneity Corrections

The method for predicting dose distributions that was presented in section 3.3 is based on beam data that was obtained from measurements made in a homogeneous water phantom. As a result, such predictions will be most accurate for regions that are composed of tissues of high water content. In realistic clinical situations, the volume to be treated does not always consist of homogeneous water-like tissue. Sometimes this volume contains, or is in proximity to, structures that are not water equivalent. The presence of such structures, referred to as inhomogeneities, will perturb the dose distribution predicted by the Milan/Bentley model. These perturbations arise from complex processes that take place in the irradiated materials. However, the general concepts affecting the over all dose distribution for points in or near inhomogeneous structures can be illustrated by referring to Figure 3-6.

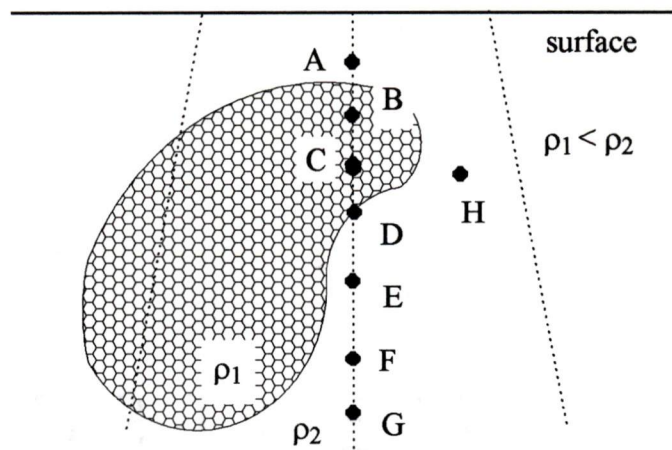


Figure 3-6: Illustration of a phantom containing a low density inhomogeneity. Various dose calculation points are identified.

In this figure, a beam is incident on a section of water like material that contains a low density inhomogeneity. In the discussion that follows, it is important to keep in mind that the dose delivered to any point within the material can be considered as having two components. There is a primary component and a secondary, scatter component. The primary dose arises from the energy that is deposited at a point by a photon that has not been scattered as it traveled from the source to the point. The secondary, or scattered component is the dose that is deposited by photons, or electrons that result from at least one scattering event.

Points that lie upstream of the inhomogeneity, like point A, will receive a primary dose that has not been altered by the presence of the inhomogeneity. However, the amount of secondary radiation that is deposited at A will be reduced due to the proximity of the low density inhomogeneity. Recall that the dominant interaction process between clinically relevant photon beams (beams with energies between about 0.1 MeV and 10 MeV) and tissue is the Compton interaction. The Compton interaction has a direct dependence on the electron density of the irradiated material. Consequently, materials with low relative electron densities, will produce less scattered radiation than materials with higher electron densities. Since the region below point A is composed of low density material, less backscatter radiation will be available to deposit dose at A.

Notice that point B lies within the low density inhomogeneous material. As a result of the decreased attenuation of the beam as it traverses the low density material, the primary dose at B will be greater than it would be if the inhomogeneity were not present. However, because point B lies in the low density region, the dose due to scattered radiation will be decreased.

The overall effect of the dose delivered to points within inhomogeneous regions will depend on the size of the inhomogeneity and where the point lies within it. Points, like point B, which lie near the upstream end of the low density inhomogeneity may have their dose unaltered or slightly reduced. Points deep within low density regions, like point C, will see an increase in delivered dose due to the under attenuated primary radiation reaching it.

The situation becomes fairly complicated for points that lie on the boundary, like point D, between low density and high density materials. In regions around such interfaces, electronic equilibrium may no longer exist. Electronic equilibrium is crucial to the assumption that the dose deposited by a beam of photons is proportional to the number of photons which cross a small area, the photon fluence, at the point of interest (Johns and Cunningham 1983). There is no practical method of calculating the dose that is delivered to points in regions that are not characterized by electronic equilibrium.

Points E, F, and G will receive an increased dose due to the under attenuating effect of the inhomogeneity on the primary radiation. But, due to the relative proximity of each of these points to the inhomogeneous material, each point will receive different amounts of scattered radiation. However, the net effect will be an increase in the dose delivered to all of these points.

Notice that the location of point H indicates that the amount of primary radiation reaching it will not be affected by the presence of the inhomogeneity. However, the local proximity of the low density material implies that there will be a reduction in the amount of scattered radiation that reaches this point.

Clearly the presence of inhomogeneities can have a significant influence on the dose that is delivered to points lying within the irradiated volume. Many methods exist for correcting the dose deposited at points influenced by the proximity of inhomogeneous

materials. The following subsections describe the inhomogeneity corrections that have been incorporated into the General Electric Target 2 software package. This will be followed by a brief description of a couple of other correction methods that exist, but are not incorporated into the G.E. Target system. These methods are included in this discussion to give the reader a sample of some of the methods that are currently under development and will possibly see widespread use as computing power becomes more affordable.

3.4.1. Equivalent Path Length Correction

The simplest of the inhomogeneity corrections is the Equivalent Path Length Correction. In this method, the presence of inhomogeneous materials along the path of the radiation is simulated by replacing the length of the inhomogeneous material with an equivalent length of water. The equivalent length of water is calculated by multiplying the path length through the inhomogeneity by the density correction factor for the inhomogeneous material. The density correction factor is defined as the electron density of the appropriate tissue relative to the electron density of water.

To illustrate this concept consider Figure 3-7. This figure will be used to show how the equivalent path length correction method can be used to calculate the dose to point P. Notice that point P lies at a depth d below the surface and that there are three regions along the path from the source to the calculation point. The density correction factors for the regions are identified as ρ_1 , ρ_2 , and ρ_3 . The first two regions have a thickness t_1 and t_2 associated with them. The point P lies at a distance t_3 within the third region. In this case, the equivalent path length, d' , is expressed as $d' = t_1\rho_1 + t_2\rho_2 + t_3\rho_3$.

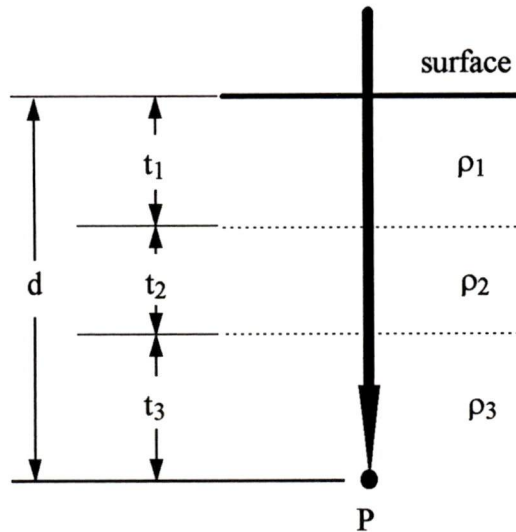


Figure 3-7: Diagram illustrating three regions with different densities.

In general, if there are N different regions of inhomogeneous materials, each of which have a density correction factor, ρ , assigned to them, the equivalent path length, d' , may be expressed as a weighted sum:

$$d' = \sum_{i=1}^N t_i \rho_i$$

Equation 3-10

(Target Physics Manual P.B1-8)

In the Target implementation the equivalent path length, d' , is used to obtain the appropriate central axis (CAX) value for dose calculations. The true depth, d , is used in the determination of any SSD corrections that are required as well as in the determination of the off-axis values. Thus, when the equivalent path length correction algorithm is employed, the percent depth dose (PDD) value is obtained from:

$$PDD(d') = CAX(d') * \left(\frac{SSD + d_{\max}}{SSD + d} \right)^2$$

Equation 3-11

(Target Physics Manual P. B1-8)

The G.E. Target implementation of this correction method can be used for both coplanar and non-coplanar beam arrangements.

This method of correcting for the presence of inhomogeneous materials has obvious advantages associated with its simplicity. However, there are also some significant disadvantages.

The equivalent path length method only attempts to compensate for the effect that inhomogeneous materials have on the primary radiation that is deposited at the calculation point. There is no attempt to correct for the change in the amount of scattered radiation that reaches calculation points due to the influence of inhomogeneous materials that do not lie on a direct path between the source and the point of interest. Examples of such situations can be seen in Figure 3-6. The equivalent path length method will predict an erroneous value for the dose deposited at all points shown in the figure. The error in the predicted dose delivered to point A will result from the loss of backscatter from the low density inhomogeneity downstream of the calculation point. The predicted dose to points B through G will be in error due to reduced side scatter in the inhomogeneous material.

Another disadvantage of the equivalent path length correction method is that it does not account for the distance that the calculation point lies from the inhomogeneity. Points E, F, and G of Figure 3-6 would be effected by errors associated with this disadvantage.

3.4.2. Power Law Correction

A method that does account for the distance between the calculation point and the boundary of the inhomogeneity is the power law correction method. This method, as it is incorporated in the Target software, is based on the empirical relationship that was developed by Batho (Batho 1964).

The general Batho equation for predicting the dose to a point, P, that lies along the path of the radiation at a depth d_1 below the surface of an N layer material can be expressed as:

$$D_P(d_1) = D_W(d_1) K_N \prod_{m=1}^N T(d_m) \frac{\mu_m - \mu_{m-1}}{\mu_0}$$

Equation 3-12

(Target Physics Manual P. B1-12)

where $T(d_m)$ is the tissue air ratio at a depth, d_m . Appendix B describes the concept of the tissue air ratio. $D_w(d_1)$ is the dose that is delivered to a depth of d_1 within a water phantom. μ_m is the linear attenuation coefficient of the m^{th} layer and μ_0 is the linear attenuation coefficient of water. The correction factor K_N is included to account for differences in the mass energy absorption coefficients between the layers. It is defined as the ratio of mass energy absorption coefficient of the N^{th} material layer, $\left(\frac{\mu_{\text{en}}}{\rho}\right)_N$, and

the mass energy absorption coefficient of water, $\left(\frac{\mu_{\text{en}}}{\rho}\right)_0$:

$$K_N = \frac{\left(\frac{\mu_{\text{en}}}{\rho}\right)_N}{\left(\frac{\mu_{\text{en}}}{\rho}\right)_0}$$

Equation 3-13

(Target Physics Manual P. B1-12)

Where μ_{en} is the linear attenuation energy absorption coefficient and ρ is physical density. The G.E. Target implementation of this inhomogeneity correction method can be applied to both coplanar and non-coplanar beam arrangements.

To illustrate the geometry involved here, consider Figure 3-8. The calculation point, P, lies at a distance d_1 below the surface of a phantom that is made up of three layers. Each layer has different linear attenuation coefficients, designated μ_1 , μ_2 , μ_3 , respectively. The calculation point lies at a distance d_3 from the boundary between

material 2 and material 3. It also lies at a distance d_2 below the boundary between material 1 and material 2.

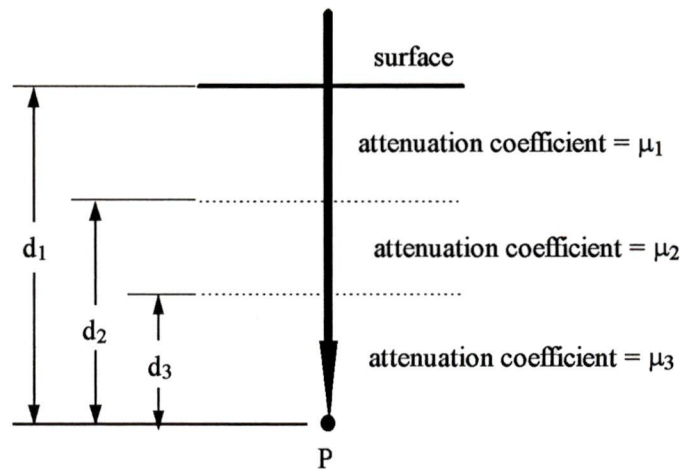


Figure 3-8: Diagram illustrating the power law correction method geometry for a calculation point, P, situated below three material boundaries.

Applying the general Batho equation to this geometry leads to the following expression:

$$D_P(d_1) = D_W(d_1) K_3 \left[T(d_1) \frac{\mu_1 - \mu_0}{\mu_0} * T(d_2) \frac{\mu_2 - \mu_1}{\mu_0} * T(d_3) \frac{\mu_3 - \mu_2}{\mu_0} \right]$$

Equation 3-14

This method of calculating the dose delivered to points below inhomogeneities gives good results. However, it does not account for the shape of the inhomogeneity. Specifically, it does not account for the change in scatter that occurs for points that lie above or beside the inhomogeneous structure. All of the points illustrated in Figure 3-6 will be effected to some degree by this change in scatter.

3.4.3. Equivalent Tissue Air Ratio (ETAR) method

The equivalent tissue air ratio (ETAR) method is the most advanced method of correcting for the presence of inhomogeneities that is included in the G.E. Target software. The Target implementation of ETAR is based on the method devised by Sontag

and Cunningham (Sontag and Cunningham 1977). CT scan data are used to correct for changes in the amount of scattered radiation reaching the calculation point from inhomogeneities that are present within the irradiated volume. In this way, the shape and proximity of inhomogeneous structures can be taken into account when determining the dose delivered to a point.

As with all the other correction methods, the underlying principle behind the ETAR method is that the dose that is delivered to calculation points that are in the vicinity of inhomogeneities can be related to equivalent points in a homogeneous phantom. In this case, if the calculation point lies at a real, physical depth d below the surface of the inhomogeneous phantom where the field size is w , then the dose delivered to this point will be equivalent to a the dose delivered to a point that lies at a depth d' below the surface of a homogeneous phantom where the field size is w' . In the Target implementation of ETAR, the equivalent depth value, d' , is taken to be the equivalent path length associated with the location of the point as it is situated with respect to the overlying inhomogeneous structures. The effective field size, w' , of the beam is determined by estimating the effective relative density at the calculation point using the CT data.

The general form of the ETAR equation that is implemented by the Target software can be expressed as:

$$D_{\text{phantom}}(x, y) = R(d, y) * \left(\frac{\text{SSD} + d_{\text{max}}}{\text{SSD} + d} \right)^2 * \frac{\text{CAX}(d', w')}{\text{CAX}(d_{\text{max}}, w')} * \frac{B(w')}{B(w)} * \text{CAX}(d_{\text{max}}, w)$$

Equation 3-15

(Sontag and Cunningham 1977)

where:

d = depth of calculation point below the surface of the phantom.

$R(d, y)$ = off axis ratio (interpolated if necessary) at depth d and a distance of y from the central axis.

$\text{CAX}(a, b)$ = central axis value (interpolated if necessary) associated with depth a and field width b .

$B(b)$ = backscatter factor (see appendix B) associated with field width b .

The G.E. Target implementation of ETAR only supports coplanar beam arrangements.

3.4.4. Other Correction Methods

As we have seen in the previous section, the inhomogeneity correction methods contained in the GE Target software system are only approximations. To date, there are only two methods which are able to completely define the dose distribution in the presence of inhomogeneous materials. They are the convolution and Monte Carlo methods.

The convolution method uses measured, or calculated dose kernels. The kernels represent narrow beam dose distribution patterns and are linac specific. These narrow beam patterns are convolved across the mathematical representation of the surface and tissues to be treated. The resulting dose distribution is an accurate representation of the dose deposition that would be measured experimentally. This method of inhomogeneity correction is available in some treatment planning software packages.

The Monte Carlo methods have their origin in high energy physics research, but have recently found their way into medical physics applications. These methods use the well known probabilities for the various types of particle interactions and the distances that these particles travel between interactions. Individual photons, or charged particles are followed as they make their way through a tissue. Various parameters can be scored, such as energy deposited, number and type of interactions, etc. If the amount and location of energy deposited is scored, an isodose distribution can be obtained. The drawback to this method, is that in order to obtain statistically significant distributions a lot of histories must be generated. The time required to generate a Monte Carlo simulation for typical clinical situations is just too long to be of practical use. Consequently, this method is only used in research situations.

4. FILM DOSIMETRY

4.1. Fundamentals

Generally, photographic film consists of a cellulose base upon which a layer of gelatin has been attached. The gelatin contains grains of silver bromide (AgBr). When radiation is allowed to interact with the film, some of the silver ions within the grains become susceptible to the chemical process in which silver ions (Ag^+) are converted to elemental silver (Ag). Such grains are said to compose a latent image. The latent image can be brought out of the film by chemical processing.

The first step in chemical processing is to subject the exposed film to a developing agent. The developing agent will eventually convert all Ag^+ ions to elemental Ag . However, the grains that make up the latent image are able to convert their Ag^+ to Ag at a faster rate than the unaffected grains. Therefore, if the film is left in contact with the developer for a short period of time, only the grains making up the latent image will have their Ag^+ converted to Ag . The process of converting the ionic silver to elemental silver is then stopped by placing the film in a stop bath solution. Once the conversion of ionic silver has been stopped, the film is placed in a "fixing" solution. The fixer is used to remove any AgBr that is not part of the latent image. The result is that the grains containing the latent image have been converted to opaque grains of silver. The film is then rinsed and air dried.

The density of silver that remains on the developed film depends on the dose to which the film has been exposed. The greater the dose, the denser the silver. Therefore, films that have been exposed to beams of radiation can be used as a dosimeter by measuring the optical density of the developed film. The optical density is related to dose values through calibration. The calibration process consists of exposing film to known doses and then relating the resultant optical density to these doses.

One of the largest drawbacks for film dosimetry is the non-linear relationship between the optical density and dose. However, there is a region where the optical density does vary linearly with dose. Problems associated with the non-linear film

response can be avoided if care is taken to ensure that the film is only exposed to radiation levels that correspond to this linear response region.

Another disadvantage is the sensitivity of film optical density to temperature variation in the chemicals used for film processing. Inadequate temperature control affects the reproducibility of optical density for films that are exposed to the same dose levels. These days, automated processing with regular quality assurance testing of these developers ensure reproducibility.

One of the primary considerations for any dosimeter is spatial resolution. Since all film contains microscopic grains of silver bromide (typically 10^{10} Ag^+ ions per grain), and it is the conversion of Ag^+ to Ag within these grains that determines the optical density of the film, excellent spatial resolution is possible. The resolution is limited by the ability of the device that is used to read the optical density, rather than the film itself.

The process of measuring the optical density does not have any effect on the distribution of the silver grains. Therefore, film is essentially a permanent record. However, fading of the latent image, on undeveloped film, can occur if exposed film is subjected to high temperatures and humidity before it is developed. This problem can be avoided by developing the film as soon as possible after irradiation.

4.2. Optical Density Measurements

The optical density values for all films were obtained using the Wellhofer Film Densitometer system. This system consists of the Wellhofer film densitometer, a system controller unit, and an IBM compatible personal computer (Wellhofer Dosimetrie).

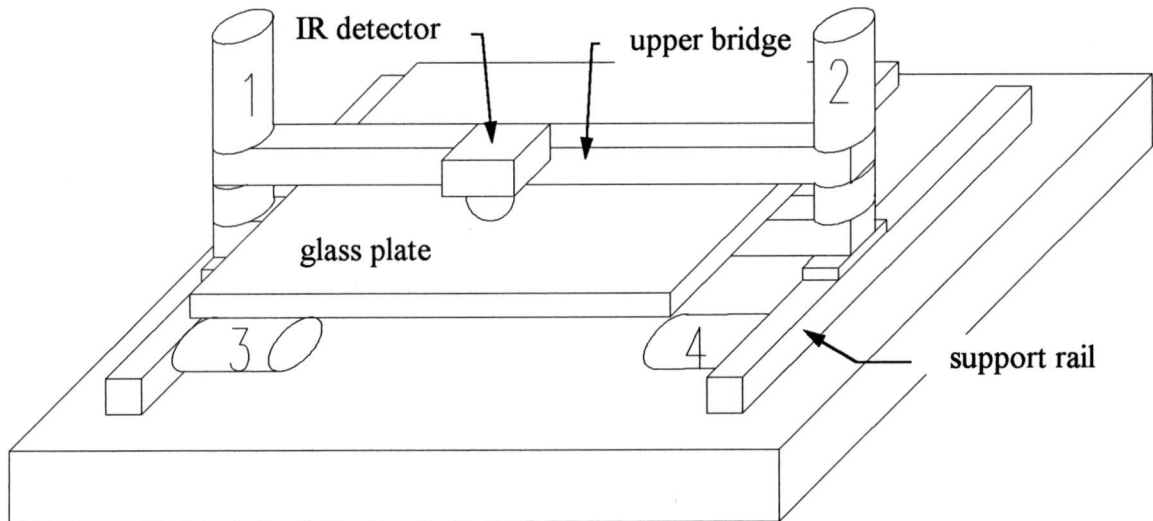


Figure 4-1: Diagram of the Wellhofer Film Densitometer.

Figure 4-1 illustrates the film densitometer and identifies some of its major components. This device consists of a glass plate attached to a support structure. The film that is to be scanned is attached to the glass plate. The detector mechanism straddles the glass plate (IR source below the plate and the detector above the plate) and is supported by a pair of bridges that span the width of the plate. This bridge structure is supported by a pair of rails, one on each side of the plate. The densitometer is able to scan a maximum area of 450 x 480 mm.

Two dimensional detector movement is accomplished by using 4 DC motors (labeled 1, 2, 3, and 4). Two of these motors, mounted at either end of the bridge, allow the detector to be moved along the bridge. The other two motors drive the bridge along the rails and are mounted at the rail end, one motor per rail. Each motor has a potentiometer to supply positional information. This combination of motors and potentiometers are able to achieve 0.5 mm positional accuracy.

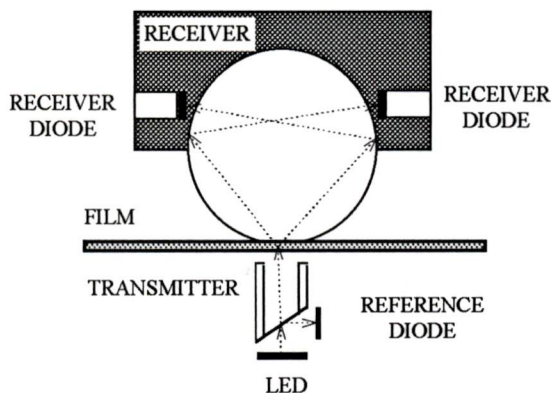


Figure 4-2: Illustration of the detector arrangement.

Optical density resolution is dependent on the detector arrangement. Figure 4.2 illustrates the detector configuration that is used by the Wellhofer densitometer. Detector spatial resolution (0.8 mm) is defined by the diameter of the infra-red (IR) beam as it leaves the transmitter. The IR beam is transmitted through the film and enters the 50 mm diameter spherical chamber of the receiver. The inside wall of the spherical chamber is coated with a reflective material. The light entering the chamber will undergo multiple reflections from the wall and eventually strike one of the four receiver diodes that are arranged symmetrically around the chamber equator. This arrangement of LED and detector eliminates the need for exact alignment between the IR source and the detector and is able to provide long-term stability without adjustment or calibration. This configuration of light source and detector diode is able to provide a resolution of ± 0.01 optical density units.

The light source is an IR diode that generates a 950 nm regulated, pulsed beam of light. The rise time of the detection diodes is dependent on the range of densities that the densitometer has been set for. If the optical density range extends from 0 to 3, the receiver diode has a 10 ms rise time. If the optical density range is expanded to cover a 0 to 4 range, the diode has a 30 ms rise time associated with it. The densitometer provides an analog output of 1 volt per density unit that is fed into the Wellhofer System Controller (Wellhofer Dosimetrie).

The System Controller acts as an interface between the PC and the densitometer. The analog data generated by the densitometer are digitized (up to 1800 conversions per second) and intercomparison (every 10 msec) of the detected and reference signals is

performed. 20 data points are then sent to the computer every second. The data points have a maximum separation of 0.75 mm. Typically, a 20 cm scan takes less than 14 seconds and provide more than 260 data points.

Data obtained from the System Controller are stored in a PC. The Wellhofer software is a very versatile and easy to use. It runs in Microsoft Windows 3.1. During data collection, the software provides the user with real time display of the detector signal vs. scanner position.

Additional features include on-screen definition of data source modules, automatic detection of the central axis position and automatic correction of the user defined setup. The user has the ability to vary the scanning speed at any time during the scan. During measurement, the distance between points of measurement is automatically varied based on the gradient of the density distribution. Also, at the completion of the scan, a user rotatable three dimensional representation of the measured distribution is available to help visualize, for example, field perturbations due to the presence of inhomogeneous structures. The conversion process for extracting dose values from optical density data is achieved by means of user defined conversion tables.

5. EXPERIMENTAL METHODS AND MATERIALS

This section describes the methods and materials used to evaluate the ability of the G.E. Target software to predict the dose distribution from non-coplanar beams incident on inhomogeneous phantoms. All of the dose distributions presented in section 7 were obtained using film. Recall that a calibration curve is required in order to relate optical density to dose. This section will begin with a description of the procedure that was used to obtain the calibration curve and the checks that were performed to ensure that the curve could be used for a variety of field sizes. This is followed by a description of the homogeneous and non-homogeneous phantoms that were used. To ensure that the phantom-film combination and the experimental setup is able to provide reliable and reproducible results, a series of coplanar measurements were performed. Coplanar measurements were chosen to test the experimental method because it is this method of administering treatment that is currently the most common method used in the clinical setting. Also, the results predicted by Target for such an arrangement have been validated by extensive use. Consequently, if the film data and the Target data match for the coplanar arrangements, it can be assumed that the experimental method is acceptable and the setup can then be modified to include non-coplanar beam arrangements.

5.1. Film Calibration

Film calibration is required in order to relate optical density to relative dose deposited for films that have been exposed to photon beams. The method of film calibration employed in this investigation made use of slabs of water equivalent material, known as “solid water”. The solid water that was used is provided by RMI¹. The setup that was used to obtain the calibration film is shown in figure 5-1. In this setup, a sheet of film is sandwiched between pieces of solid water. The exact chemical composition is proprietary information, but the specification sheet identifies that it has a density of 1.035 g/cm³ and an electron density of 1.00 in relation to liquid water. Solid water is the material of choice for film calibration because it is not only easier to use than liquid water,

¹ RMI: Radiation Measurements Incorporated, Madison, WI., U.S.A.

it also allows easy support for sheets of film while having densitometric and radiologic properties that are virtually identical to liquid water.

A single batch of film was used for all trials in order to eliminate the discrepancy that is associated with using different batches of film. Horton predicts that there can be as much as a 10% discrepancy between batches of film (Horton 1987). Kodak XV (10" x 12") film was used for all measurements. In order to cover the expected range of optical densities for the experimental setup, 60 cGy were delivered to the d_{\max} point for the setup shown in Figure 5-1.

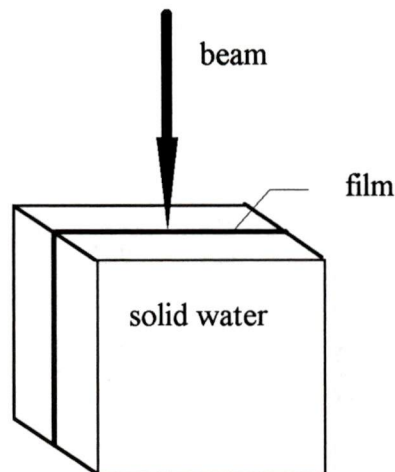


Figure 5-1: Diagram illustrating a piece of film sandwiched between pieces of solid water and irradiated by a beam.

The Wellhofer densitometer was used to obtain the optical density at specific central axis points below the water surface. The CAX depths chosen correspond to the depths that are contained in the percent depth dose tables in the British Journal of Radiology (BJR), Supplement No. 17: Central Axis Depth Dose Data for Use in Radiotherapy is considered to be the industry standard for central axis percent depth dose values measured in water or equivalent media. Therefore, relating the appropriate BJR percent depth dose data to the measured optical density obtained from a film that has been exposed to a 10 cm x 10 cm open field allows us to generate a calibration curve.

Confirmation of the validity of the calibration curve was obtained by using it to generate a set of isodose curves for a 10 cm x 10 cm field, arranged as in Figure 5-1, and comparing this set of curves to the set generated by the Target software for a similar 10

cm x 10 cm field size. Once we were satisfied that the calibration curve could be used to accurately generate isodose curves from the irradiated film for the 10 cm x 10 cm field size, we then used the same calibration curve to generate isodose curves for a variety of other field sizes to ensure that the calibration could be used for a range of field sizes.

The method used to obtain the films was identical to that used for the 10 cm x 10 cm field. A piece of XV film was sandwiched between slabs of solid water and irradiated with an open field. The developed film was then scanned with the Wellhofer film scanner. The raw optical density data was converted to dose values using the conversion curve and a series of isodose curves were generated from the scanned data. These isodose curves were then compared to the corresponding isodose curves generated by the Target software.

Once we had established the range of field sizes over which the calibration curve could be used, we proceeded to the next phase of the project. In that phase, we needed to design clinically relevant phantoms. We also needed to establish that the phantoms we had designed could be used with film to generate isodose curves that could be compared to the Target predicted isodoses for coplanar beam arrangements.

5.2. Phantoms

Four phantoms were used over the course of this investigation. All four phantoms have a common exterior geometry consisting of a right circular cylinder that is 30 cm in diameter and about 22 cm in length. A cylindrical phantom was chosen because it is the simplest geometrical shape that is “patient-like”. A cylinder is patient like in that it has a rounded surface with no sharp corners. The rounded surface also allows us to use incident beams from any direction without having to consider phantom corner effects on the dose deposition pattern.

All phantoms basically consist of a volume of homogeneous material that surrounds inhomogeneous structures. The phantoms differ with regard to the shape and composition of the inhomogeneities that are contained in the homogeneous material. The homogeneous material used for all phantoms is called “pressed wood”. This material has

virtually identical dosimetric and radiological properties to water. Hence, it is an acceptable material for patient modeling.

The cylindrical phantoms are made up of a series of circular slabs which are fitted together with nylon pins. Having the phantom composed of circular slabs makes it easy to place film between the slabs in order to determine the dose deposition in planes perpendicular to the long axis of the phantom. Figure 5-2 illustrates the way the circular disks are combined to form a cylindrical phantom using the nylon pins. The two end pieces are common to all phantoms and do not contain inhomogeneous materials. The central disks differ from phantom to phantom, depending on the type of inhomogeneity desired.

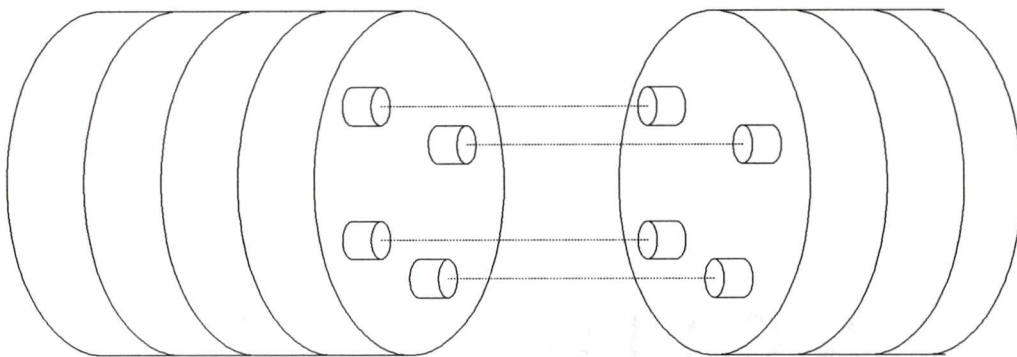


Figure 5-2: Illustration of the circular phantom components and how they fit together with nylon pins to form a cylindrical phantom.

Figure 5-3, 5-4, 5-5 and 5-6 show representative cross sections indicating the shape of the inhomogeneity for all the phantoms that were used. Table 5-1 describes the inhomogeneity inclusion present in each phantom and the materials that were used to model them. Phantom A does not contain any inhomogeneous materials. It can be considered as a cylinder of water. Phantom B contains lung-like inhomogeneities. Cork was chosen as lung-like material because it has a similar electron density to real lungs. Phantom C contains bone-like inhomogeneities. Aluminum rods were used to represent bone like material, since aluminum has similar electron density to bone. Phantom D consists of the same cylindrical inhomogeneities as phantom C except that the aluminum

rods have been removed to leave air cavities. These small air cavities are similar to the air cavities found in such regions as the trachea or air filled sections of the intestine.

Phantom Identifier:	Tissue inhomogeneity inclusion:	Materials used to approximate the tissue-like inclusion:
A	not applicable	not applicable
B	Lung	Cork
C	Bone	Aluminum
D	Air	Air

Table 5-1: Table identifying the tissue inhomogeneity that is included in each phantom and the materials that were used to approximate the enclosed inhomogeneity.

The first phantom used to gather data was Phantom A, the homogeneous phantom. A sheet of XV film was loaded into the center of the phantom. The phantom was then positioned on the bed so that the center of the phantom lies at the isocenter of the machine and the long axis lies in the same plane as the long axis of the treatment couch. Three square open fields, equally spaced around the perimeter of the phantom and in a coplanar beam arrangement were used to “treat” the phantom. Table 5-2 specifies the table, collimator, and gantry angles that define the three coplanar beams as well as the number of monitor units used.

The monitor unit is the parameter that defines how much radiation is delivered by a linear accelerator. At the Vancouver Island Cancer Centre, the linacs have been calibrated so that one monitor unit will deliver 1 cGy to the d_{max} point in a water phantom where the water surface is 100 cm from the source and the field size is 10 cm x 10 cm.

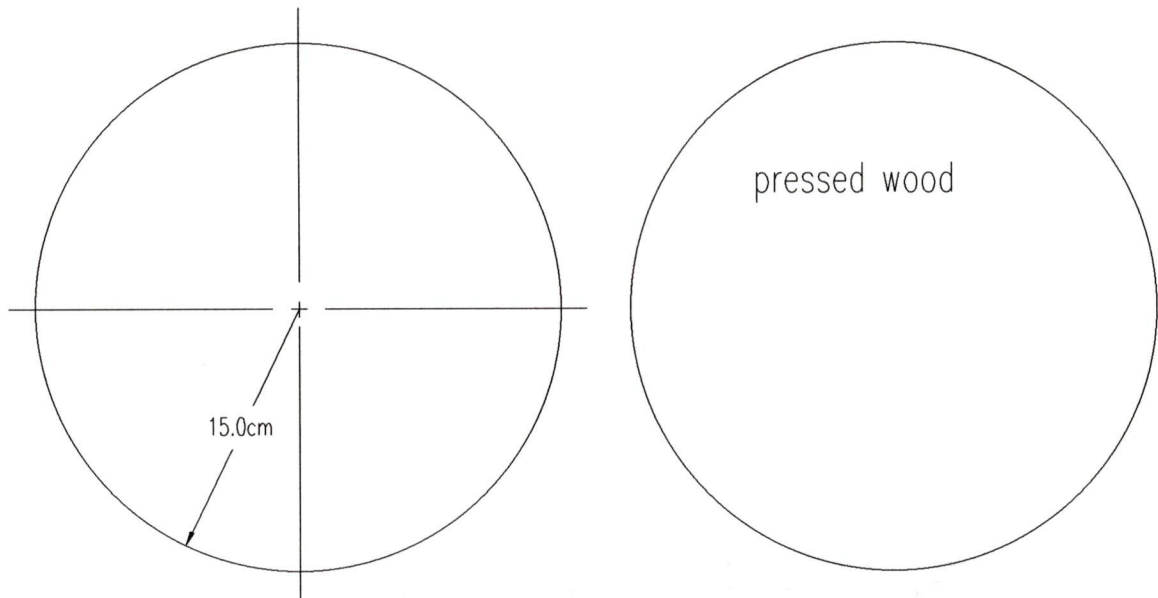


Figure 5-3: Diagram illustrating cross sectional detail for Phantom A .

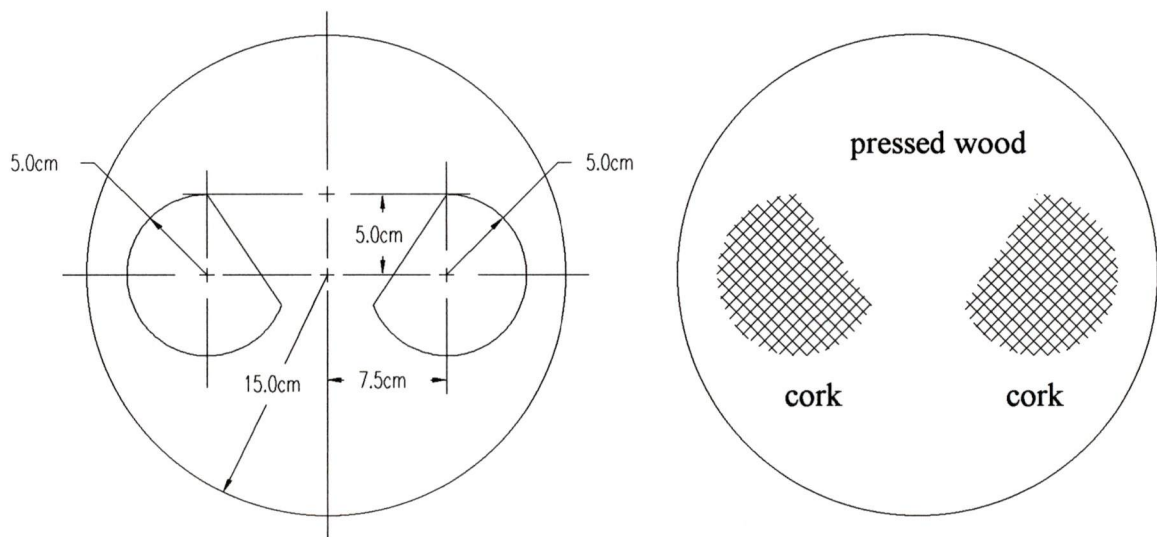


Figure 5-4: Diagram illustrating the cross sectional detail for Phantom B.

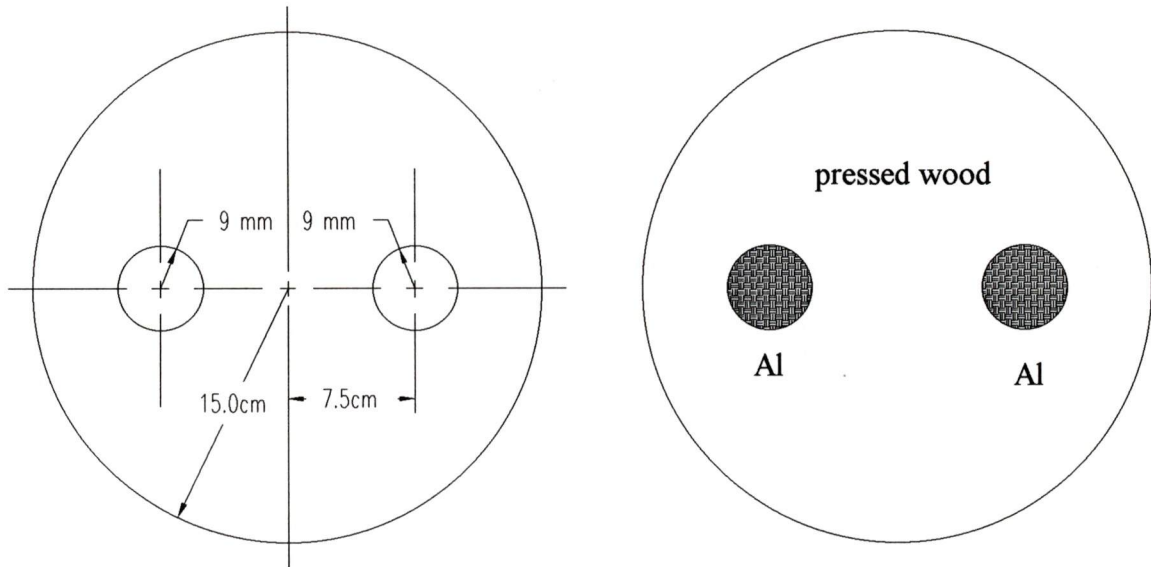


Figure 5-5: Diagram illustrating the cross sectional detail of Phantom C.

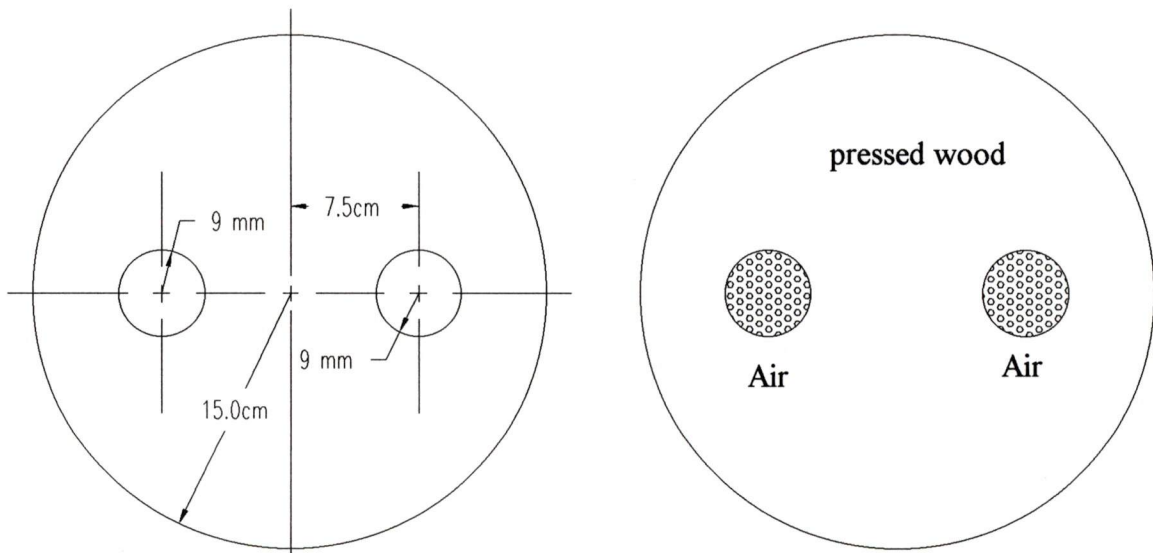


Figure 5-6: Diagram illustrating the cross sectional detail for Phantom D.

BEAM NUMBER:	TABLE ANGLE:	COLLIMATOR ANGLE:	GANTRY ANGLE:	MONITOR UNITS:
1	0	90	180	20
2	0	90	300	20
3	0	90	60	20

Table 5-2: Treatment parameters for all coplanar measurements

The developed film was scanned by the Wellhofer densitometer and the raw optical density information converted to relative dose deposited using the correction curve for the XV film. The resulting isodose curves were compared with the Target generated isodose curves for the same experimental configuration to establish the validity of the experimental method and to confirm that the Target software was able to accurately predict the dose distribution in this coplanar situation.

Once it was confirmed that this experimental setup was able to generate films of acceptable quality and that the Target software was able to predict the dose deposition pattern for this relatively simple situation, the same setup was used to obtain dose deposition patterns for the same three beams, but in a non-coplanar arrangement. Table 5-2 specifies the treatment table, collimator, and gantry angles defining the three non-coplanar beams as well as the monitor units used for each beam. Again, comparing the measured dose deposition pattern to the Target generated pattern allowed us to determine if the experimental setup would work to obtain films for non-coplanar beam arrangements in homogeneous phantoms.

BEAM NUMBER:	TABLE ANGLE:	COLLIMATOR ANGLE:	GANTRY ANGLE:	MONITOR UNITS:
1	340	90	300	20
2	20	90	60	20
3	90	90	160	20

Table 5-3: Treatment parameters for all non-coplanar measurements.

Dose deposition patterns for the three inhomogeneous phantoms were experimentally obtained using the same methodology. Initially, a three field coplanar beam arrangement was used to obtain a film which could be used in comparing dose deposition patterns with the Target software. Then, a three field, non-coplanar film was obtained and compared to the dose deposition pattern predicted by Target.

Coplanar measurements were made for all four phantoms, but non-coplanar isodose distributions were obtained for only phantom A and phantom B.

5.3. Target Generated Dose Distributions

Before the G.E. Target software can predict the dose distributions that would result from user defined beam arrangements, it must be provided with phantom details. Essentially, these details include phantom geometry and the density information of each type of material making up the phantom. Normally, in the every day clinical environment, this information is provided to the treatment planning software via CT scans. However, the G.E. Target software also allows the user to define the phantom geometry using a digitizer and to provide density information by hand from the keyboard. Since the phantoms used in this project are relatively simple with no variation in the structure of the inhomogeneity from slice to slice, the digitizer/keyboard method was used to define the phantom for the software.

The entire phantom geometry was defined by digitizing in a series of slices, perpendicular to the long axis of the phantom. Each slice included the outside border of the phantom and the outline of any inhomogeneous structure contained within the phantom outline. The software also prompts the user for density information as well as labels which are used to identify structures which are common to a number of slices.

Once all of the slices have been entered, the user validates the entire outline set for 3-D. In doing this, the software will work through all the slices to ensure that it can identify structures common to more than one slice and that the densities remain constant for structures common to adjacent slices.

Having completed this, the user is then free to define and align the beams that are required to “treat” the phantom. Once the beams have been defined and positioned

relative to the phantom, the user can ask the software to predict the isodose distributions that would result from the beam arrangement. At this point, the user also has the option of defining which method should be used to correct for the presence of any inhomogeneous materials within the phantom.

All four phantoms and the beams that were used to treat them, both coplanar and non-coplanar, were defined in this way. The target software was used to generate dose distributions for the same experimental configurations that were used with the phantom and film configurations described above. All three of the inhomogeneity correction algorithms provided by the Target software were used when inhomogeneities were present.

6. ERROR ANALYSIS

Any experimental or theoretical data, determined by measurement or calculation, always has some error associated with it. The data obtained in this investigation is presented mostly in the form of isodose curves. Recall that isodose curves represent the spatial distribution of the relative dose deposited across a given plane. Consequently, the errors associated with isodose curves can be considered as having two, not necessarily independent, components. The first component consists of errors in the positioning of the specific isodose curves. This is the error that is associated with identifying the precise spatial location for a given isodose curve within the plane. The second component is the error in the relative dose deposited at any given position on the plane. In this section, errors that have been identified with the use of film to measure relative dose deposition within the phantoms, and those inherent in the G.E. Target calculation of dose deposition patterns are presented.

6.1. Film Errors

Errors have been identified in the experimental data that was obtained using film. These include reproducibility, film calibration, and errors associated with the Wellhofer film scanner.

6.1.1. Calibration Curve Errors

The film calibration curve is used to relate optical density to dose. A separate calibration curve is required for each photon beam energy and for each batch of film used to measure the dose deposition pattern. In the experimental work presented here, a single photon beam energy and a single batch of film was used. The method used to obtain the calibration curve was presented in section 5.1. The calibration curve was generated using the Victoria Cancer Centre 6 MV linear accelerator and a 10 cm x 10 cm open field, perpendicularly incident on solid water at SSD=100cm. The magnitude of the errors associated with the calibration can be obtained from the spread of data obtained as a result of producing a number of calibration curves. Ten curves were used to obtain a range of

density values for each optical density point. These values were then converted to dose and included with the calibration curve as error bars. The calibration curve for all film that was used in this project can be seen in Figure 6-1.

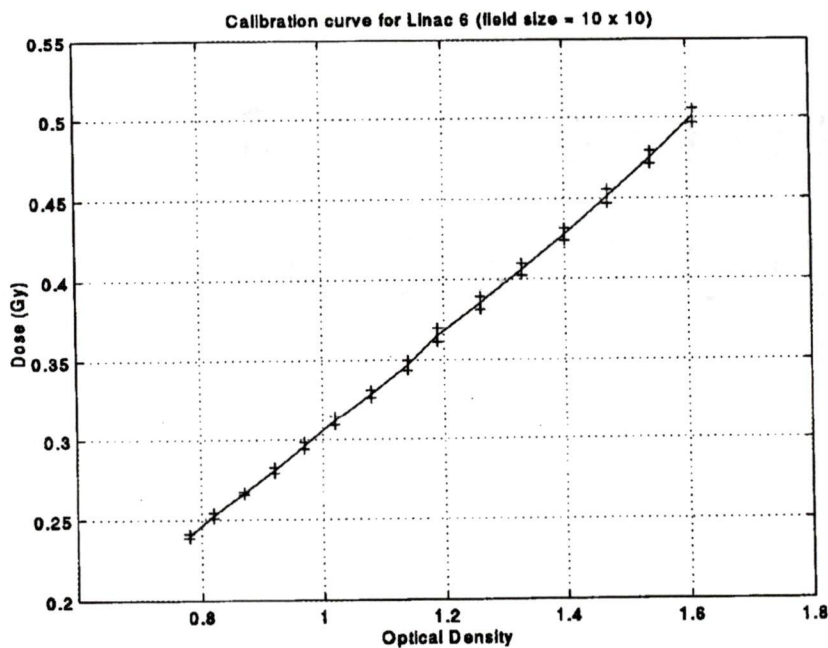


Figure 6-1: Calibration curve for Kodak film batch number 162-20-1. Generated using the Victoria Cancer Centre 6 MV linear accelerator for a 10 cm x 10 cm open field perpendicularly incident on solid water at SSD = 100 cm.

The magnitude of the error bars represents the discrepancy that is inherent in using films from the same batch, since there is virtually no setup error for the simple setup used to obtain the calibration curves. This magnitude, as seen in figure 6-1, is about $\pm 1\%$. This is in agreement with the precision, as stated by Horton (Horton 1987), of 3% between films of the same batch, processed at the same time.

6.1.2. Scanner Errors:

Scanner errors are those that can be attributed to the Wellhofer densitometer system. The drive mechanism for the Wellhofer densitometer has 0.5 mm positional accuracy. The densitometer transmitter/receiver combination yields 0.8 mm spatial resolution, due to the diameter (spot size of the beam on the film) of the infrared beam. Together, these two sources of error will provide a total (added in quadrature) of 0.94 mm error in the determination of the spatial location of the isodose curves. Additionally, the light source/detector diode arrangement is able to measure optical density to within ± 0.01 density units. Since the errors associated with the densitometer are very small, it is unlikely that they will contribute to visible error bars on the isodose plots for the phantoms as seen in the next section.

6.1.3. Reproducibility Errors:

Film reproducibility is associated with the errors that are inherent in the experimental setup. In essence, these errors are associated with positioning the phantom in exactly the same location, with respect to the beams, for subsequent measurements. The overall error, which has been identified as reproducibility errors, have components that arise from a number of sources. Contributing to the reproducibility error is the difference between films of the same batch, the fact that the table is not physically able to rotate around an exact point, the fact that the isocenter of the linac is not an exact point but rather an oblate sphere, and the difficulty associated with manually getting the geometrical center of the phantom to coincide with the machine isocenter for repeated measurements.

The difference between films of the same batch will be the most insignificant of these sources of error, but will be the predominant source of error for the calibration curve, as discussed previously. The contribution to the overall error due to the mechanical rotations of the table and gantry in combination with the error due to the manual alignment of the phantom geometrical center with the machine isocenter will be the largest error. The magnitude of the error associated with reproducibility was obtained by using seven films and a 15 cm x 15 cm, three field coplanar beam arrangement incident on phantom D. Figure 6-2 illustrates the spread in the isodose distribution. For clarity, only the 30 %, 70 %, and 95% isodose curves have been included. A similar spread is seen for the other isodose curves. The spread in the 50% values has a magnitude that is the same as the 30% values, the magnitude of the spread in the 90% isodose curve has a magnitude that is similar to the spread seen in the 95% isodose distribution. Notice, for the 70% isodose distribution, the magnitude of the reproducibility error depends on where, spatially, the point of interest lies within the plane of the phantom. For example, there is a large reproducibility error in the region corresponding to a cross plane distance of 5.00 cm and a depth of 23.00 cm. Points in this region lie in the penumbral region for all three beams. In the penumbral regions, a small error in spatial location (e.g.: off axis distance) will lead to a large uncertainty in the percent dose deposited. A similar isodose plot for the even curves revealed that all even curves have a reproducibility error that is similar in magnitude to the 30% lines shown in Figure 6-2.

6.1.4. Total Error for the Film Isodose Curves

The total error in the location of the isodose curves that are obtained from the exposed films has essentially three components. These components are the errors in the calibration curve, the errors that can be attributed to using the Wellhofer film scanner to acquire film density information, and reproducibility errors that are inherent in the experimental setup. Of these three, the reproducibility error component was found to be the dominant one. Recall that it is the combination of errors associated with the mechanical movements of the linac table and gantry positioning as well as the errors in the alignment of the phantom with the beam that contribute to the reproducibility error. We

were able to quantify the size of this error by obtaining multiple films, using the same setup. This method of determining the size of the reproducibility error also includes the error in the calibration curve since it was determined that the calibration curve error was primarily due to using films from the same batch.

The overall error attributed to using the Wellhofer film scanner is just over 1 mm. Since this error is dominated by the reproducibility/calibration curve error, the overall error for the film generated isodose curves will have the positional dependence shown in Figure 6-2. The error bars which arise due to this error are superimposed on the isodose distributions shown in the results section that follows. However, only a few error bars are included to present the trends and to keep the diagrams from becoming too crowded.

6.2. Target Error

The errors that are associated with the isodose distributions generated by the G.E. Target software arise from two sources. The first is due to the error that is inherent in the method used to measure the central axis depth dose curve and profiles that are directly stored as the Target beam model. The second is due to the fact that the Target generated isodose distributions are derived from the Milan/Bentley model and output from the software is in the form of a dose matrix that is used to create an isodose distribution.

6.2.1. Measured Data

The data that was obtained for the G.E. Target beam data files was measured using the Wellhofer water tank and ion chambers. The Wellhofer water tank drive mechanism, used to position the ion chamber within the water tank, is identical to the drive mechanism used by the film densitometer. This drive mechanism is able to position the ion chamber with a spatial accuracy of 0.5 mm along each of the principal axis. The ion chambers have a discrepancy of $\pm 0.5\%$ associated with their use. Additionally, there will be an error associated with the experimental setup of the water tank with respect to the machine isocenter. The effect that these measurement errors have on the Target output is

considered to be negligible since, in total, they will not be any greater than the line thickness of the isodose curves.

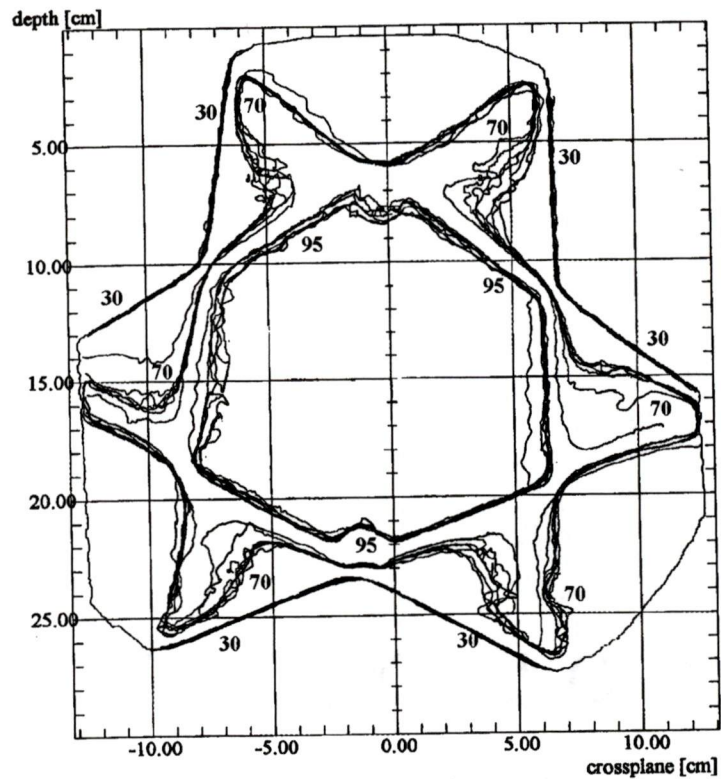


Figure 6-2: Illustration of the typical spread in isodose curves due to film reproducibility errors. For clarity, only the 30%, 70%, and 95% isodose curves have been included.

6.2.2. Errors Associated with the Milan/Bentley Algorithm

Recall that the G.E. Target beam models are based on the Milan/Bentley formalism, and are generated from 17 CAX values and five profiles, with each profile consisting of 47 points, for square fields only. Beam data that is required and is not explicitly stored is obtained by linearly interpolating between the stored values. The beam data is used to calculate the dose that is distributed within a dose matrix. There are two sizes of dose matrices that are used. The first matrix contains 512 points. This relatively coarse matrix is used for video display purposes only. A finer dose matrix consisting of 4096 points is used for hard copy output. Errors that can be attributed to the use of this type of beam modeling algorithm will consist of two general categories. The first is due to the errors that result from interpolating the stored data files (the central axis depth dose curves and the beam profiles). The second will be errors associated with linearly interpolating an output dose matrix that is of a finite size to obtain isodose distributions.

For example, the following interpolation steps may be performed for any given dose computation:

1. Linear interpolation of CAX values between field sizes to obtain a set of CAX values for the required field size.
2. Linear interpolation between these CAX values to obtain the CAX at the required depth.
3. Linear interpolation of all the off axis values between field sizes to obtain a set of off axis values for the required field size.
4. Linear interpolation between these profiles of off axis values to obtain a profile at a required depth.
5. Linear interpolation within this profile to obtain the off axis value at the required distance from the central axis.

Once these interpolations have been completed for each point in the dose matrix covering the patient outline, the isodose curves that are output to hard copy is determined by linearly interpolating the output dose matrix values.

Mott (Mott 1994) has studied the effect that these interpolations have on the final dose distribution that are determined by the G.E. Target software. The following

discussion of error propagation through the Milan/Bentley model is based on Mott's work. Selected portions of his analysis have been reproduced for the beam data that is used at the Vancouver Island Cancer Center to illustrate that the results obtained by him can be applied to our 6 MeV beam, as modeled by our data.

6.2.2.1. CAX Errors

The complete set of central axis depth dose curves that are stored for the Vancouver Island Cancer Centre 6 MeV beam is illustrated in Figure 6-3. The central axis depth dose curves for 11 square field sizes have been stored ranging from 4.0 cm to 6.0 cm in steps of 1.0 cm, then from 8.0 cm to 12.0 cm in steps of 2.0 cm, and from 15.0 cm to 30.0 cm in steps of 5.0 cm, and finally CAX values are stored for a 40.0 cm field. To estimate the errors that arise from linearly interpolating the central axis data, a complete set of CAX values is obtained by linearly interpolating between nearest neighbors in both the depth and field size directions. These values can then be compared to the measured values at each of the interpolation points and a pair of difference arrays, one for the interpolation in the depth direction and one for interpolation in the field size direction, can be constructed. Each of these arrays contains 11 x 17 points (11 CAX curves with 17 points per curve).

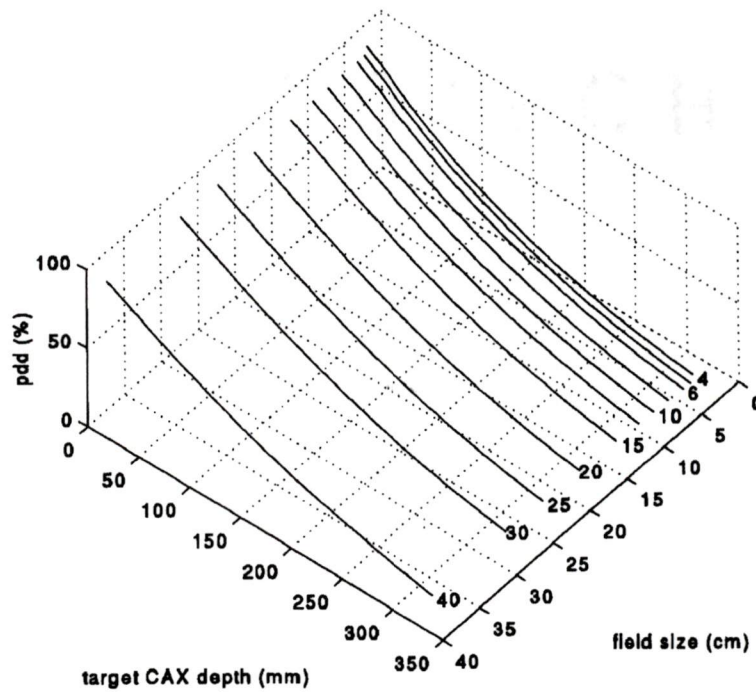


Figure 6-3: The complete set of CAX depth dose curves for the Vancouver Island Cancer Centre 6 MeV photon beam.

The following table presents the mean interpolation error and the standard deviation of the interpolated errors for both the field interpolation and the depth interpolation.

	Mean Interpolation Error (% depth dose units)	Standard Deviation of the Interpolated Errors (% depth dose units)
Field Interpolation	0.049	±0.111
Depth Interpolation	-0.160	±0.082

Table 6-1: Results from statistical analysis of CAX beam data for the Vancouver Island Cancer Centre Linac 6.

According to Mott, the mean interpolation error is principally dependent on the errors introduced by the interpolation process. The standard deviation is mainly related to the inherent noise in the beam data set. Notice that the mean depth interpolation has a larger magnitude than the mean field interpolation error. This gives the impression that, on average, the interpolation along the CAX will produce a value that will be 0.16% below the value that would be measured at that same CAX point for each beam modeled by the Target software. However, this absolute error of -0.16% will not have any effect on the dose distributions obtained in this project. Recall that dose distributions here are relative distributions, normalized to the maximum dose point. Any absolute error associated with the dose points making up the distribution will have no effect on the relative doses delivered to each point. The same can be said for the effect this type of error will have on patient plans in the clinical setting because beam time calculations are primarily based on an in-house system, rather than the output from the Target software. To this end, the G.E. Target software is used to generate relative dose distributions and beam weightings.

The standard deviation of the interpolated errors, essentially our ability to precisely require measured values that are close to the average value, is also shown in table 6-1. Notice that the largest standard deviation is associated with interpolation between field sizes. Based on the relative magnitudes of the standard deviations for the two interpolation processes, interpolation in the field direction will be the largest contributor to error in determining central axis values. However, the combined error of the two interpolation processes is still less than 0.2% . An error of this magnitude is too small to have any visible effect on the resulting target output.

6.2.2.2. Off-Axis Profile Errors

Since the results of the CAX error analysis for the Vancouver Island Cancer Centre 6 MeV photon beam data are, in general, similar to the analysis performed by Mott, it is assumed that the off axis profile error results also will be similar. Mott's off axis profile analysis consists of a comparison between the 90% off axis distance value for the interpolated profiles and the true 90% off axis distance. Two interpolation profiles were obtained. One by interpolation in the field direction and the other by interpolating between profiles for a given field size. This analysis shows that errors associated with off axis profile interpolation are insignificant.

6.2.2.3. Dose at a point

The dose to a point is the product of the CAX value and the off-axis ratio. Since the error in the off-axis ratios is negligible, it will be the error in the CAX that will dominate. Recall that the CAX errors are due to both interpolation errors and beam data errors. From the data presented in table 6-1, we see that the interpolation error will be half the sum of the mean field error and the mean depth error, or -0.060%. The beam data error is found by taking the root mean square sum of the two standard deviation interpolation error values presented in Table 6-1 and is found to be 0.138%. Taking the absolute sum of these two error values will give us the maximum percentage error that will be associated with any isodose curve. This sum, 0.157%, can be used to obtain the fractional uncertainty that is associated with any isodose value.

Mott performed an extensive evaluation of the effect that such an error has on the spatial location of isodose curves. The method employed was to increase and decrease the profile values by 0.005, 0.010, and 0.015 and determine the error in the spatial location of the 90% point on each profile. He found that although the spatial errors follows the shape of the profile, with the error increasing when the 90% point lies above the shoulder, in the low gradient section, spatial errors are generally less than 1 mm unless the fractional error in the CAX values is greater than 0.01. For our uncertainty of 0.157%, we can expect a spatial error less than 1 mm per beam for all isodose curves above the 15% level. Consequently, since a maximum of 3 beams were used in this project, the Target error

bars, associated with the Milan/Bentley data sets will not be much larger than the thickness of the line used to plot the isodose curve.

6.2.2.4. Dose Matrix Resolution

The G.E. Target software maintains a pair of dose matrices, one for displaying the isodose lines on a video monitor and one for hard copy output. The video display matrix contains 512 points, the hard copy output matrix contains 4096 points. Recall that the Target software will arrange the matrix points in a regular fashion over a rectangle which is just large enough to cover the calculation plane. In our case, all phantoms have a 300 mm cross sectional diameter. The Target software will arrange the 4096 hard copy output points on a 300 mm x 300 mm square grid having 64 rows and 64 columns. Therefore, for hard copy output, the spatial resolution will be about 4.7 mm/point ($300 \text{ mm} / 64 \text{ points} = 4.69 \text{ mm/point}$).

To investigate the effect that dose matrix resolution has on the spatial variation in isodose line location consider a typical set of profiles that are used to model a photon beam. Each beam model consists of 5 profiles, each of which is made up of 47 equally spaced points. The first profile of the beam data set is located at the d_{\max} depth for the particular beam energy. As an example, consider the profile data set for the 10 cm x 10 cm, 6 MV photon beam at the Vancouver Island Cancer Centre. For this particular beam, d_{\max} is 15 mm below the water surface. The profile data points were measured with the water surface 1000 mm from the effective source of the linear accelerator. There is 80 mm separating the five profiles that make up this particular beam data set. The data points were collected so that the fan line separation along the first profile is 2.81 mm. Since 47 fan lines implies that there are 46 spaces between the fan lines, the table width, or the width of the first profile, is $46 \times 2.81 \text{ mm} = 129.26 \text{ mm}$. From similar triangles, we can show that a fan line separation of 2.81 mm along the first profile yields a profile width of 170.02 mm for the deepest, or fifth, profile.

Therefore the beam data resolution along the profiles will range from 2.81 mm for the first profile to 3.79 mm ($= 170.02 \text{ mm} / 46$) along the fifth profile. Recall that our 30 cm diameter phantom has a Target hard copy output matrix resolution of 4.76 mm

(=300mm/63). Therefore, the Target output matrix will under sample the off axis profile data.

Mott investigated this typical under sampling of the profile data by increasing the number of data points making up the Target profile, sampling this off-axis profile data using a typical dose matrix spatial resolution to produce a sampled profile, and comparing the location of the 90% off-axis distance of the sampled profile to a best estimate of the actual location of the 90% point for a variety of profile resolutions and beam sizes.

His analysis of the spatial error associated with the resolution of the dose matrix reveals that if the matrix resolution is at least 4 mm, the spatial errors associated with the location of the isodose curves is within 1 mm. He also found that if the spatial resolution reaches 5 mm, the maximum spatial error is 1.25 mm with a 25% probability of an error greater than 1 mm, for a 10 cm x 10 cm beam. Therefore, for our spatial resolution of just under 5 mm, we expect a maximum spatial error of just over 1 mm due to the dose matrix resolution.

6.2.3. Total Error in Target Isodose Distributions

The errors that are contained in the Target generated isodose distributions have been identified as coming from two sources. The first source can be attributed to the error associated with using the Wellhofer water tank and ion chamber to measure the beam model data. The second is the error that is inherent in the beam model itself.

The beam model used by the G.E. Target system is based on the one proposed by Milan and Bentley. In this model a relatively sparse matrix of measured data is used as the beam model. Relative dose values for points that have not been explicitly stored are determined by linear interpolation of the stored data. Analysis of these errors follows the ideas that have been presented by Mott.

Analysis of the measurement error due to using the Wellhofer system to gather the beam data shows that a spatial error of 0.5 mm and about a 1% error in the magnitude of the relative dose value is expected. Any error in the setup of the water tank itself is insignificant, since the Wellhofer software will position the chamber at the center of the field before it proceeds to gather data. Therefore, as long as the center of the beam is

close to the center of the water tank, any error in the position of the water tank from one measurement time to another will not have any effect on the data that is gathered.

The error in the determination of dose to a point is made up of a CAX linear interpolation error and an off-axis profile linear interpolation error. Subsequently, the relative dose distribution presented to the user at the end of the interpolation process comes in the form of an isodose curve that has been generated from a dose matrix. Mott found that the error in the Milan/Bentley algorithm is primarily due to the resolution of the dose matrix with an error of just over 1 mm expected for a matrix resolution on the order of 5 mm. We have shown that the 30 cm diameter phantom used in this project will yield a dose matrix resolution of just under 5 mm. Consequently, the combined spatial error, due to data measurement and Target algorithm will be on the order of 1.5 mm. Since the line width of the plotted isodose curves is 1 mm, there will not be any error bars visible for the isodose curves that are output from the Target software.

7. RESULTS

This section presents the experimental results which were obtained from measurements using film and the results provided by the Target software. The calibration curve has already been presented as Figure 6-1. The series of isodose curves for a variety of field sizes, indicating that the calibration curve generated can be used for a range of field sizes.

The isodose curves, for both the film distributions and the Target distributions, corresponding to coplanar and non-coplanar beam arrangements for the four phantoms used in this project are also presented in this section. Recall that non-coplanar measurements were only made for phantoms A and B. The complete set of results for each phantom are presented in turn. The isodose distributions are presented for the coplanar and the non-coplanar cases for a given phantom before the results for the next phantom are presented. In all cases the complete set of isodose curves (10%, 20%, ..., 90%, 95%, 100%) is broken into two figures. The odd isodose curves are presented first, followed by the even isodose curves. This was done to keep the figures from becoming too cluttered, and masking trends in the data. Isodose curves for phantom A, the homogeneous phantom, are presented first, with the coplanar distribution preceding the non-coplanar distribution. This is followed by the results for the phantom with the lung-like inclusion, phantom B, organizes as for phantom A. Phantom C isodose distributions are presented next. Recall phantom C contains the aluminum rods. Finally, the results for phantom D are presented. A discussion of the results, presented in this section, is given in the following section.

7.1. Film Calibration

The calibration that was used to convert the optical density to relative dose deposited for all of the films that were used in this project has been previously been presented as Figure 6-1.

Figure 7-1 to Figure 7-5 shows the isodose curves for a 6 MV photon beam that are generated by the Target software (the dashed lines) and those obtained using film (the solid lines) for the following field sizes:

Figure Number:	Field Size (cm):
7-1	6 x 6
7-2	8 x 8
7-3	12 x 12
7-4	15 x 15
7-5	20 x 20

Table 7-1: Table identifying the range of field sizes used to illustrate the validity of the film calibration curve.

7.2. Phantom A: The Homogeneous Phantom

Figure 7-6 and Figure 7-7 present the isodose distributions that were obtained for phantom A, the homogeneous phantom using a three field coplanar beam arrangement. Figure 7-6 illustrates the depicts the odd isodose curves while figure 7-7 shows the even curves.

Figure 7-8 and Figure 7-9 illustrate the isodose distributions using a three field non-coplanar beam arrangement. The odd isodose curves can be seen in Figure 7-8, while the even isodose curves are shown in Figure 7-9.

In all cases, the film isodose curves are solid and the Target isodose curves are dashed.

7.3. Phantom B: Inhomogeneous Phantom (Lung Equivalent Inclusions)

Figure 7-10 to Figure 7-19 illustrates the isodose distributions that were obtained using Phantom B for coplanar and non-coplanar beam arrangements and inhomogeneity dose corrections. Table 7-2 describes the Target correction algorithm corresponding to the Phantom B coplanar beam arrangement isodose distributions. Table 7-3 identifies the Target inhomogeneity correction algorithm that was used for the non-coplanar beam arrangements.

In all cases, the film isodose curves are solid and the Target isodose curves are dashed.

Figure Number:	Isodose Curves:	Inhomogeneity Correction Algorithm:
7-10	odd	equivalent path
7-11	even	equivalent path
7-12	odd	power law
7-13	even	power law

Table 7-2: Table relating figure number to inhomogeneity correction algorithm for the coplanar beam arrangement and Phantom B.

Figure Number:	Isodose Curves:	Inhomogeneity Correction Algorithm:
7-14	odd	equivalent path
7-15	even	equivalent path
7-16	odd	power law
7-17	even	power law

Table 7-3: Table relating figure number to inhomogeneity correction algorithm for the non-coplanar beam arrangement and Phantom B.

Figures 7-18 and 7-19 illustrate that the isodose distributions for the ETAR and the power law inhomogeneity correction methods are essentially identical.

7.4. Phantom C: Inhomogeneous Phantom (Bone Equivalent Inclusions)

Figure 7-20 to Figure 7-25 presents the film isodose curves (solid lines) and the Target generated isodose curves (dashed lines) for the three field coplanar beam arrangement incident on Phantom C. Table 7-4 identifies the Target correction algorithm that was employed to generate the isodose distributions for these figures.

In all cases, the film isodose curves are solid and the Target isodose curves are dashed.

Figure Number:	Isodose Curves:	Inhomogeneity Correction Algorithm:
7-20	odd	equivalent path
7-21	even	equivalent path
7-22	odd	power law
7-23	even	power law

Table 7-4: Table identifying the Target inhomogeneity correction algorithm used for the three field coplanar beam arrangement for Phantom C.

Figures 7-24 and 7-25 illustrate that the isodose distributions for the ETAR and the power law inhomogeneity correction methods are essentially identical.

7.5. Phantom D: inhomogeneous Phantom (Air Cavities)

Figure 7-26 to Figure 7-29 illustrates the isodose distributions that were obtained using a three field coplanar beam arrangement. The film generated isodose curves are the solid lines and the dashed lines are the Target generated isodose distributions. In this case, the field size was 15 cm x 15 cm for and 15 mu/beam for all beams. Table 7-5 identifies the Target inhomogeneity correction algorithm that was used for each figure.

In all cases, the film isodose curves are solid and the Target isodose curves are dashed.

Figure Number:	Isodose Curves:	Inhomogeneity Correction Algorithm:
7-26	odd	equivalent path
7-27	even	equivalent path
7-28	odd	power law
7-29	even	power law

Table 7-5: Table identifying which inhomogeneity correction algorithm was used for the three field coplanar beam arrangement and Phantom D.

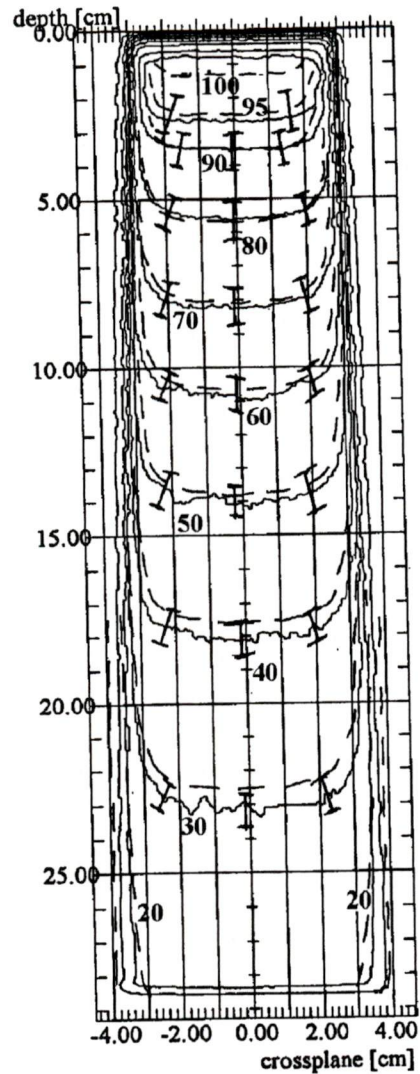


Figure 7-1: Isodose curve for a 6 MV 6 cm x 6 cm open field perpendicularly incident on solid water at SSD = 100 cm. The Target isodose distribution is indicated by the dashed lines. Film isodose distribution is indicated with solid lines.

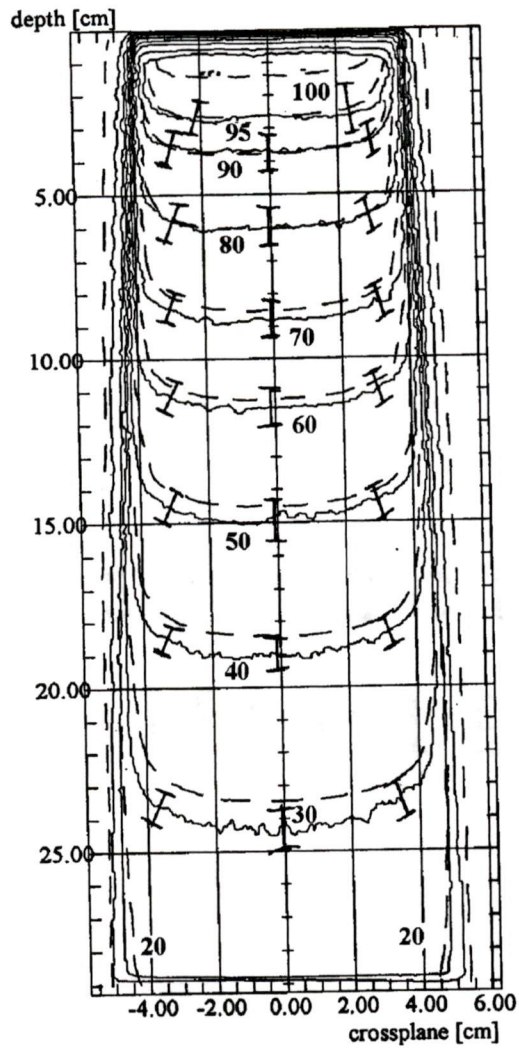


Figure 7-2: Isodose curve for a 6 MV 8 cm x 8 cm open field perpendicularly incident on solid water at SSD = 100 cm. The Target isodose distribution is indicated by the dashed lines. Film isodose distribution is indicated with solid lines.

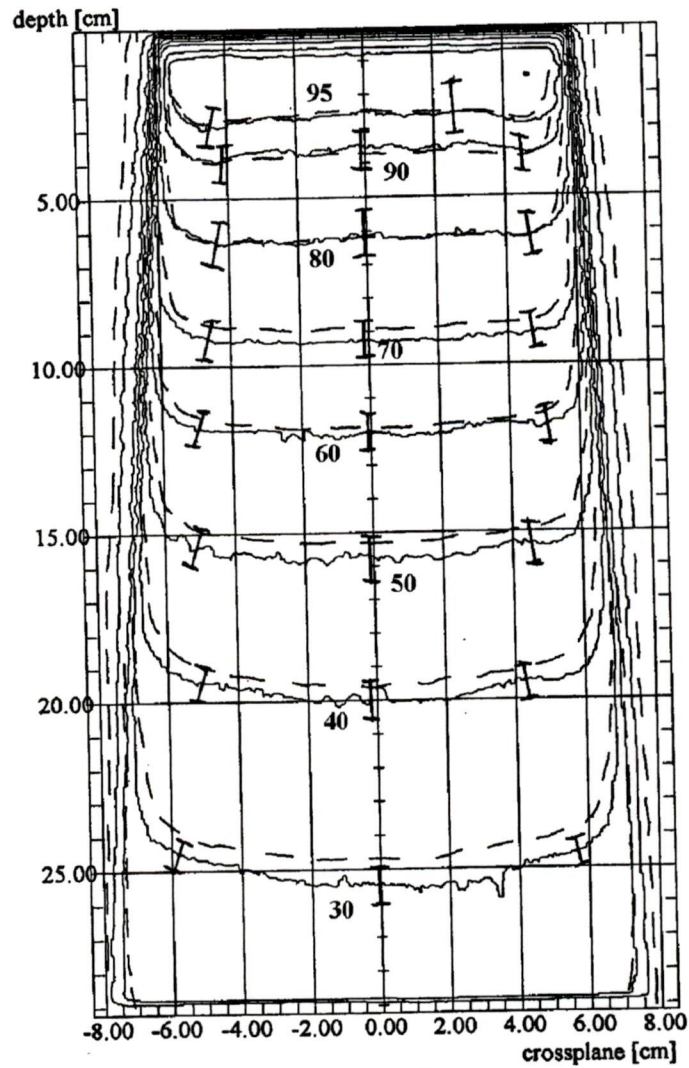


Figure 7-3: Isodose curve for a 6 MV 12 cm x 12 cm open field perpendicularly incident on solid water at SSD = 100 cm. The Target isodose distribution is indicated by the dashed lines. Film isodose distribution is indicated with solid lines.

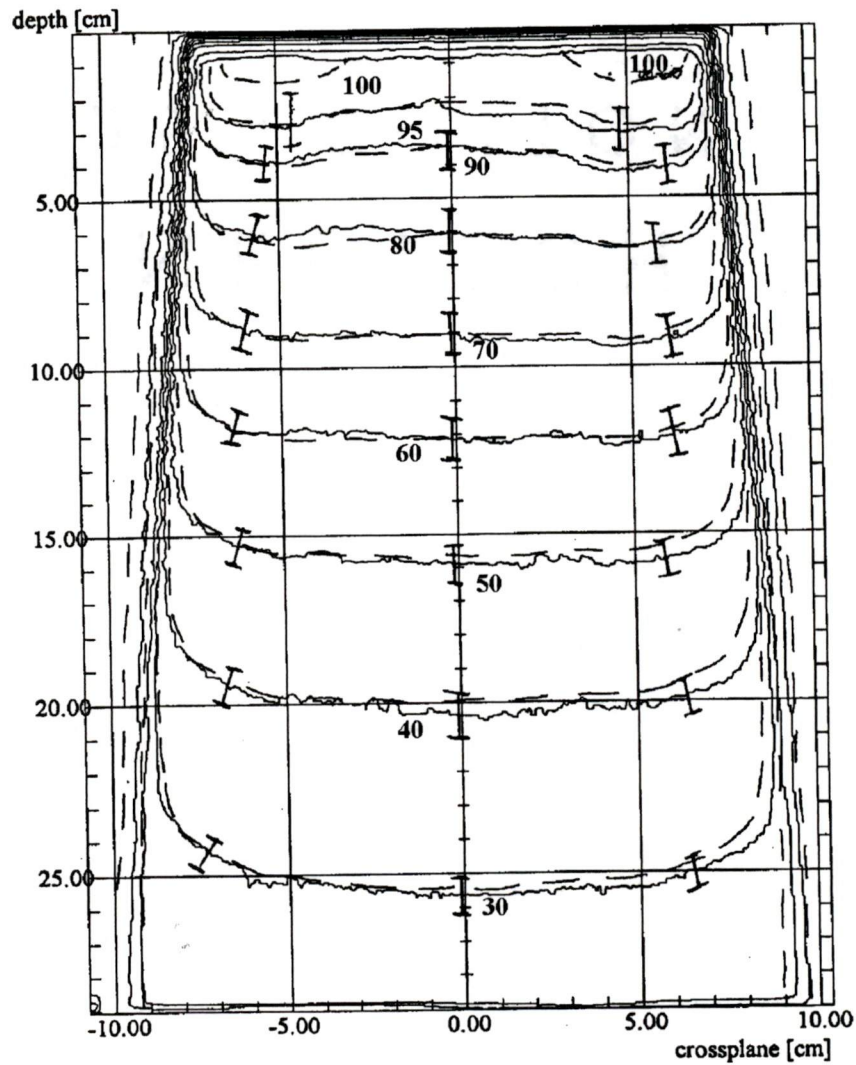


Figure 7-4: Isodose curve for a 6 MV 15 cm x 15 cm open field perpendicularly incident on solid water at SSD = 100 cm. The Target isodose distribution is indicated by the dashed lines. Film isodose distribution is indicated with solid lines.

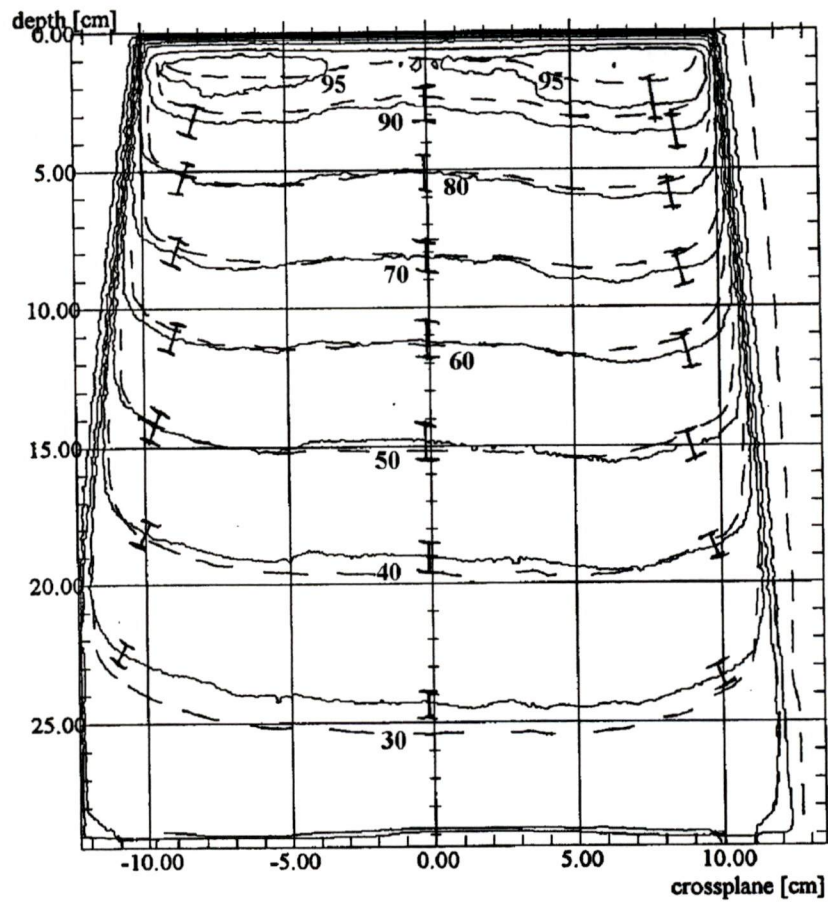


Figure 7-5: Isodose curve for a 6 MV 20 cm x 20 cm open field perpendicularly incident on solid water at SSD = 100 cm. The Target isodose distribution is indicated by the dashed lines. Film isodose distribution is indicated with solid lines.

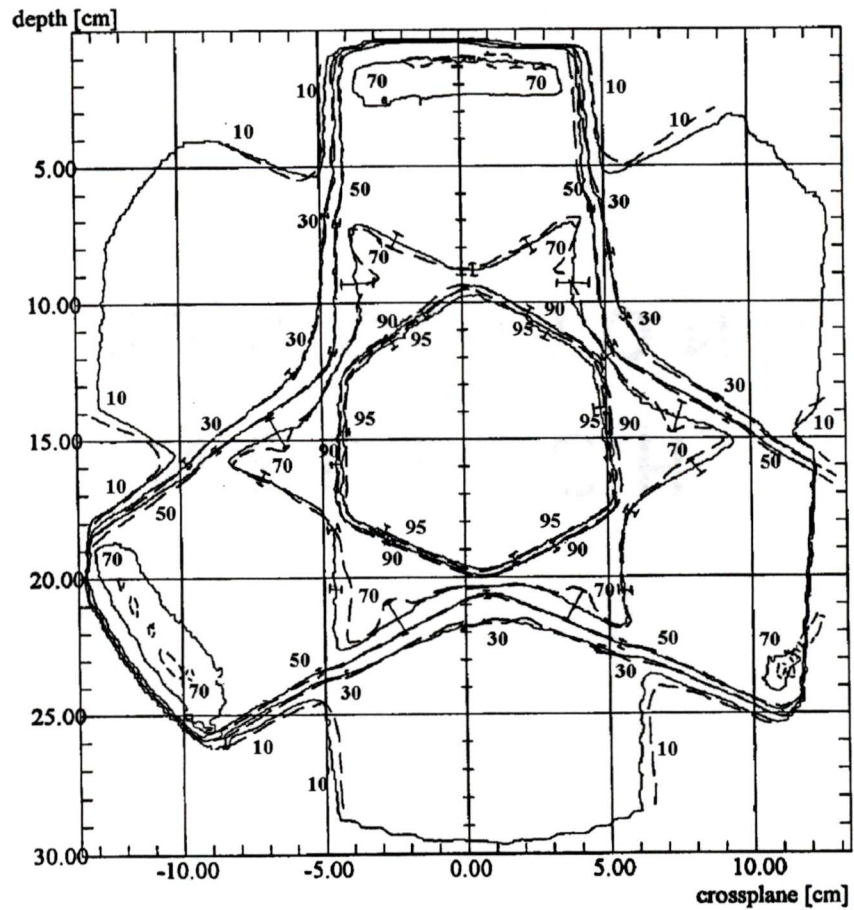


Figure 7-6: Odd isodose distribution for Phantom A as a result of a three field coplanar arrangement. Film distribution is indicated by the solid lines. The Target distribution is identified by the dashed lines. No correction algorithm has been employed, since this phantom is homogeneous.

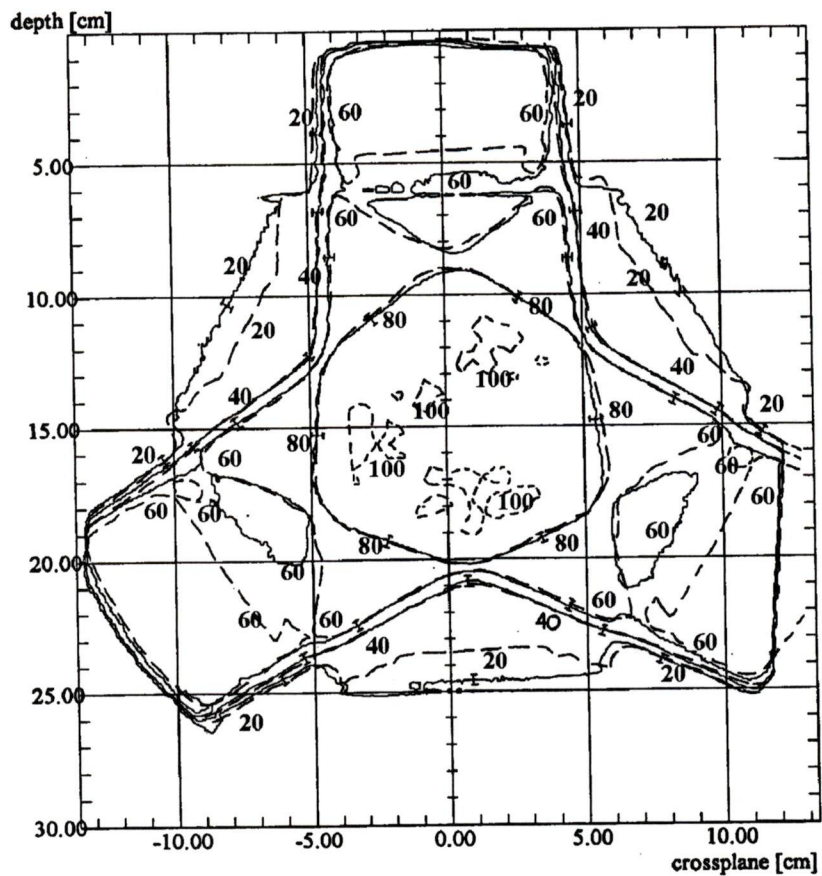


Figure 7-7: Even isodose distribution for Phantom A as a result of a three field coplanar arrangement. Film distribution is indicated by the solid lines. The Target distribution is identified by the dashed lines. No correction algorithm has been employed, since this phantom is homogeneous.

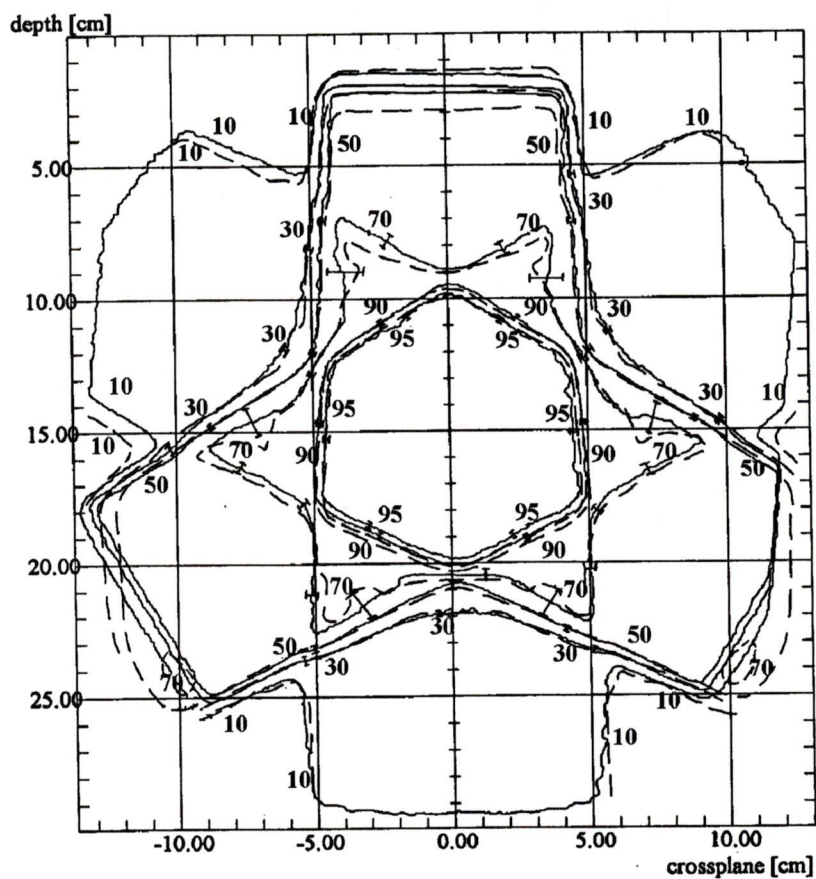


Figure 7-8: Odd isodose distribution for Phantom A as a result of a three field non-coplanar arrangement. Film distribution is indicated by the solid lines. The Target distribution is identified by the dashed lines. No correction algorithm has been employed, since this phantom is homogeneous.

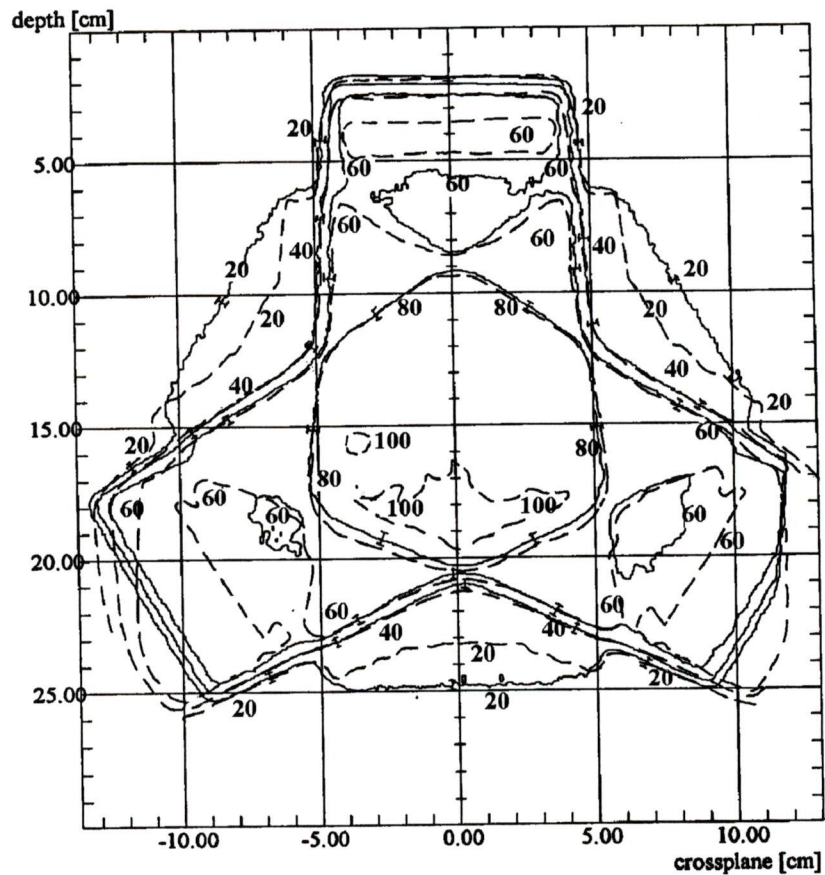


Figure 7-9: Even isodose distribution for Phantom A as a result of a three field non-coplanar arrangement. Film distribution is indicated by the solid lines. The Target distribution is identified by the dashed lines. No correction algorithm has been employed, since this phantom is homogeneous.

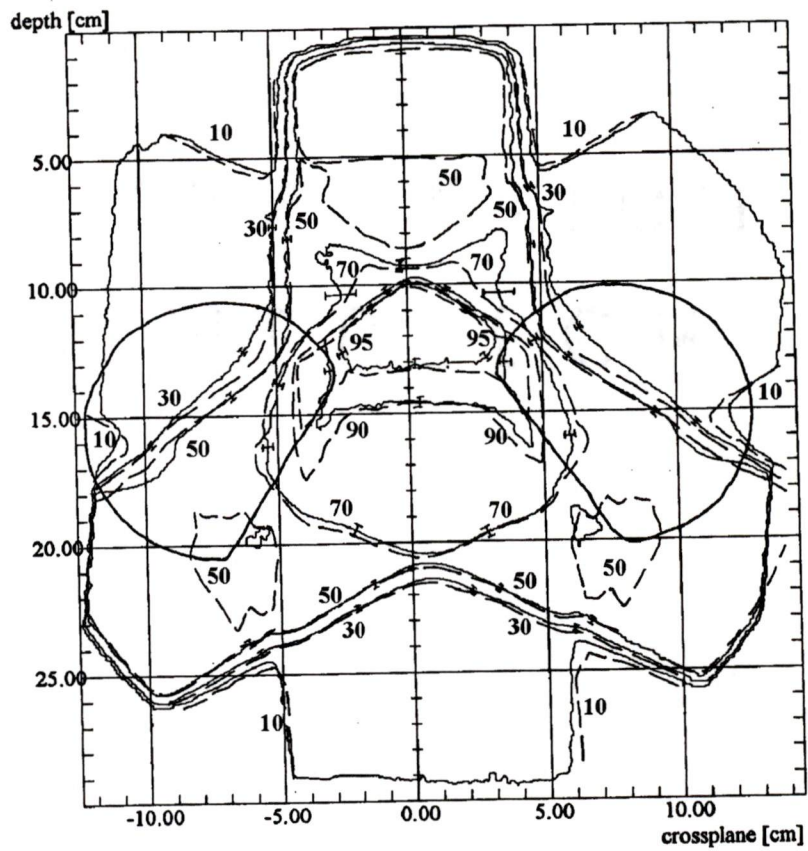


Figure 7-10: Odd isodose distribution for Phantom B as a result of a three field coplanar arrangement. Film distribution is indicated by the solid lines. The Target distribution is identified by the dashed lines. The equivalent path correction algorithm has been employed in an attempt to correct for the presence of the inhomogeneous structure.

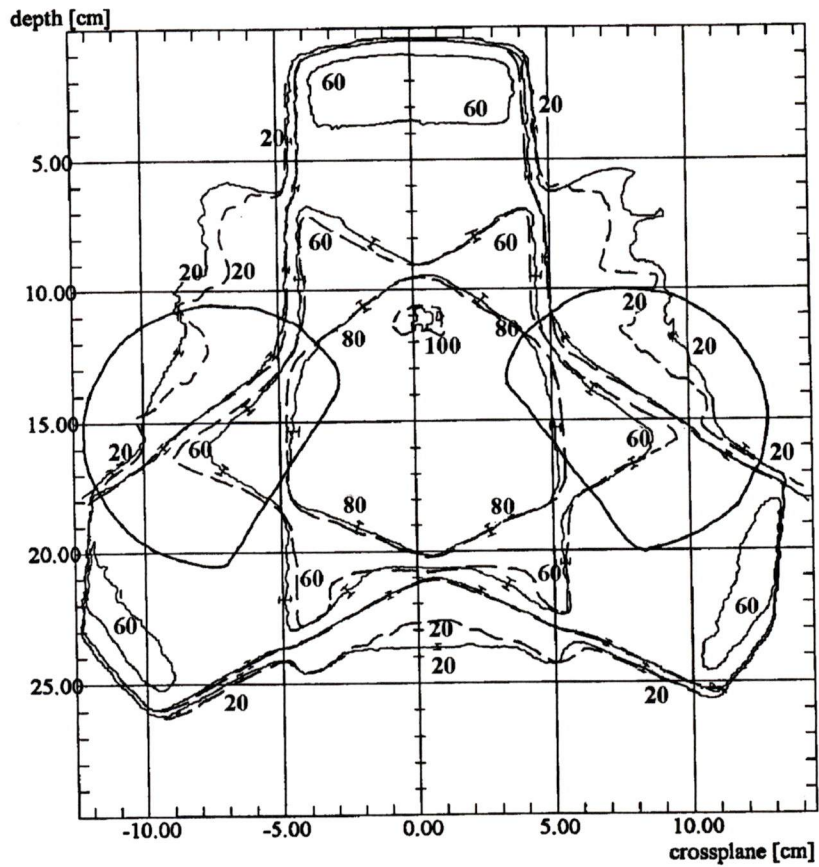


Figure 7-11: Even isodose distribution for Phantom B as a result of a three field coplanar arrangement. Film distribution is indicated by the solid lines. The Target distribution is identified by the dashed lines. The equivalent path correction algorithm has been employed in an attempt to correct for the presence of the inhomogeneous structure.

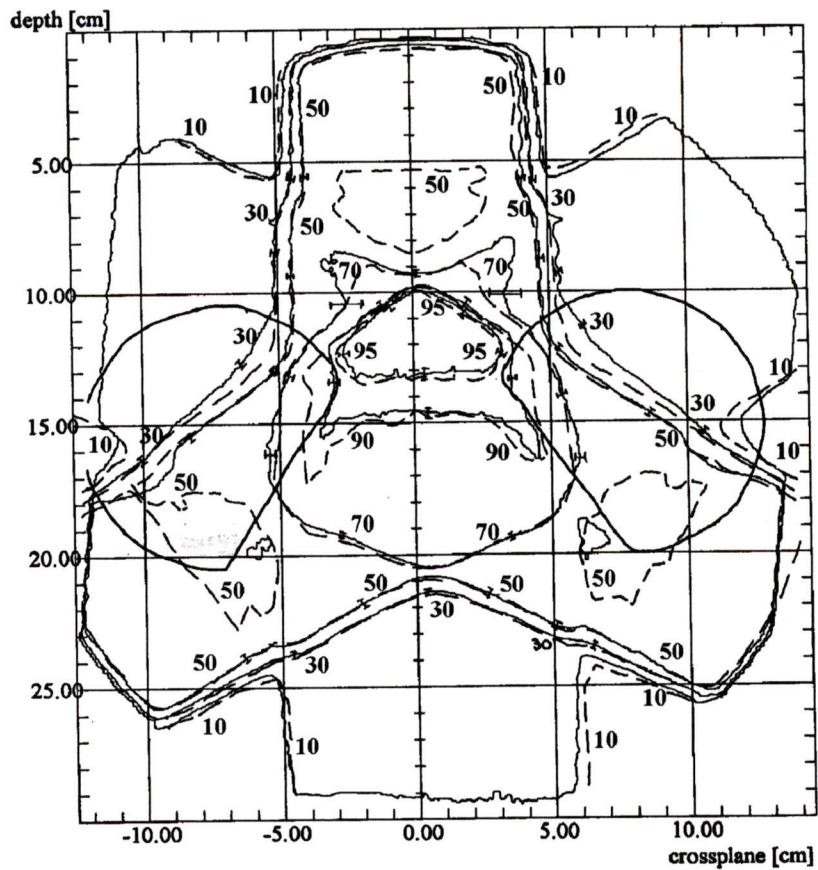


Figure 7-12: Odd isodose distribution for Phantom B as a result of a three field coplanar arrangement. Film distribution is indicated by the solid lines. The Target distribution is identified by the dashed lines. The power law correction algorithm has been employed in an attempt to correct for the presence of the inhomogeneous structure.

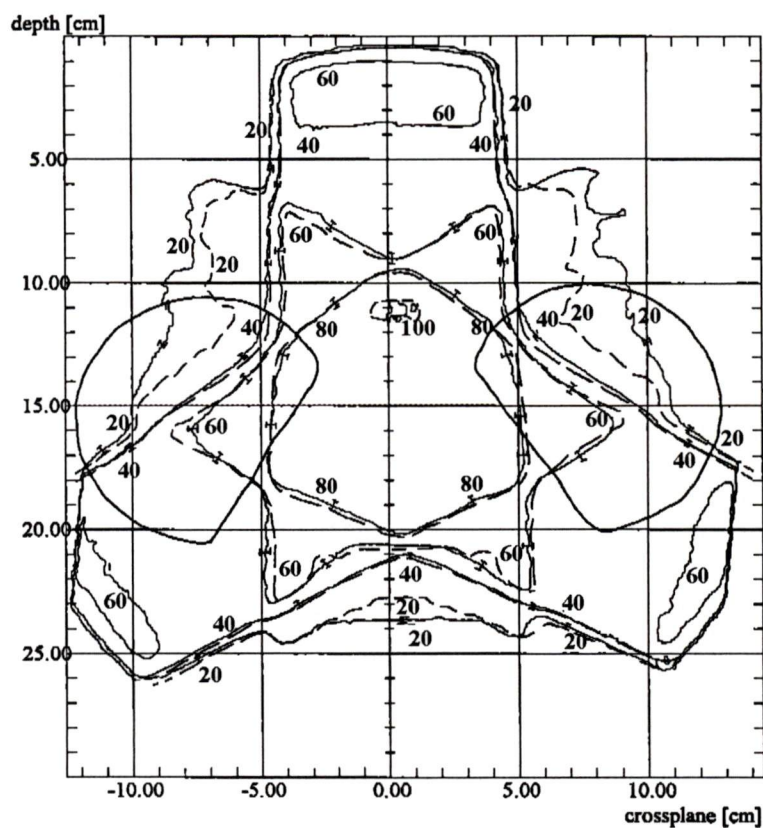


Figure 7-13: Even isodose distribution for Phantom B as a result of a three field coplanar arrangement. Film distribution is indicated by the solid lines. The Target distribution is identified by the dashed lines. The power law correction algorithm has been employed in an attempt to correct for the presence of the inhomogeneous structure.

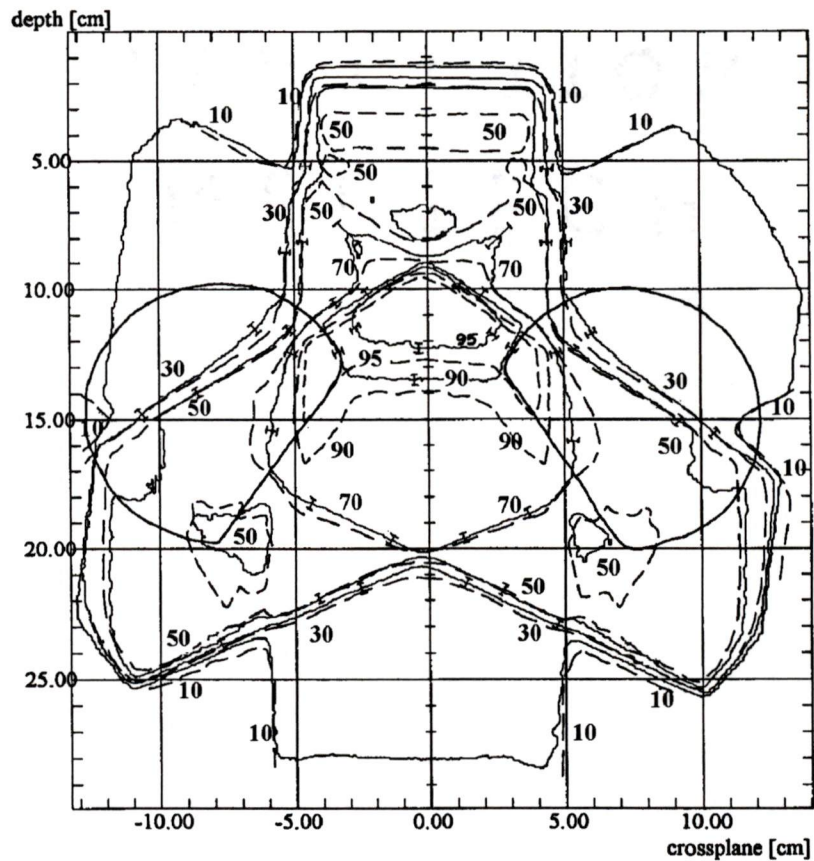


Figure 7-14: Odd isodose distribution for Phantom B as a result of a three field non-coplanar arrangement. Film distribution is indicated by the solid lines. The Target distribution is identified by the dashed lines. The equivalent path correction algorithm has been employed in an attempt to correct for the presence of the inhomogeneous structure.

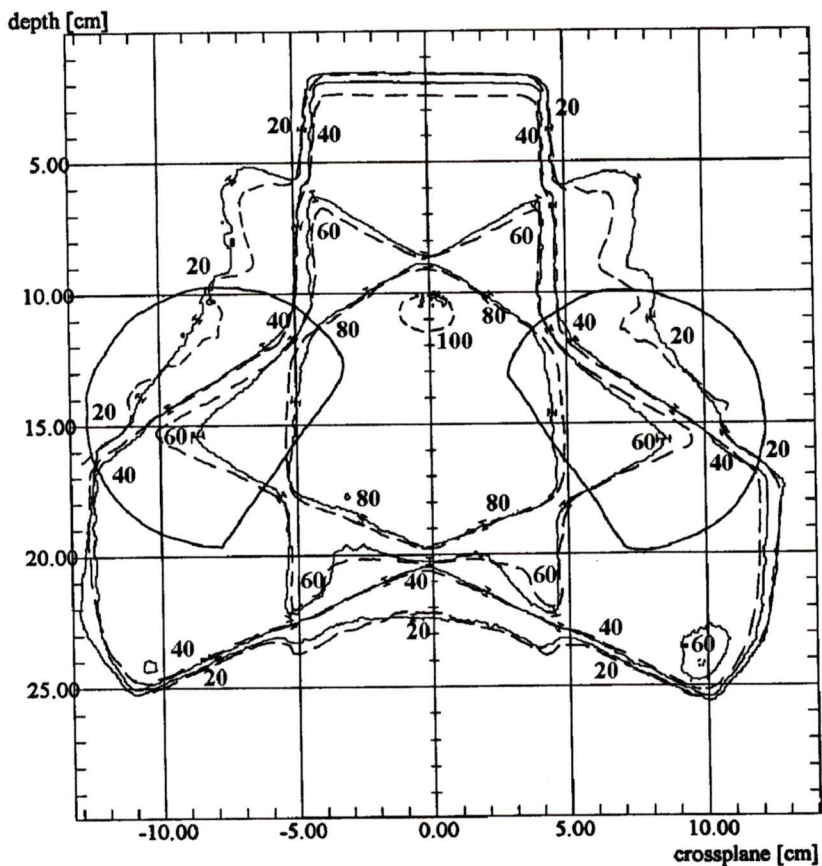


Figure 7-15: Even isodose distribution for Phantom B as a result of a three field non-coplanar arrangement. Film distribution is indicated by the solid lines. The Target distribution is identified by the dashed lines. The equivalent path correction algorithm has been employed in an attempt to correct for the presence of the inhomogeneous structure.

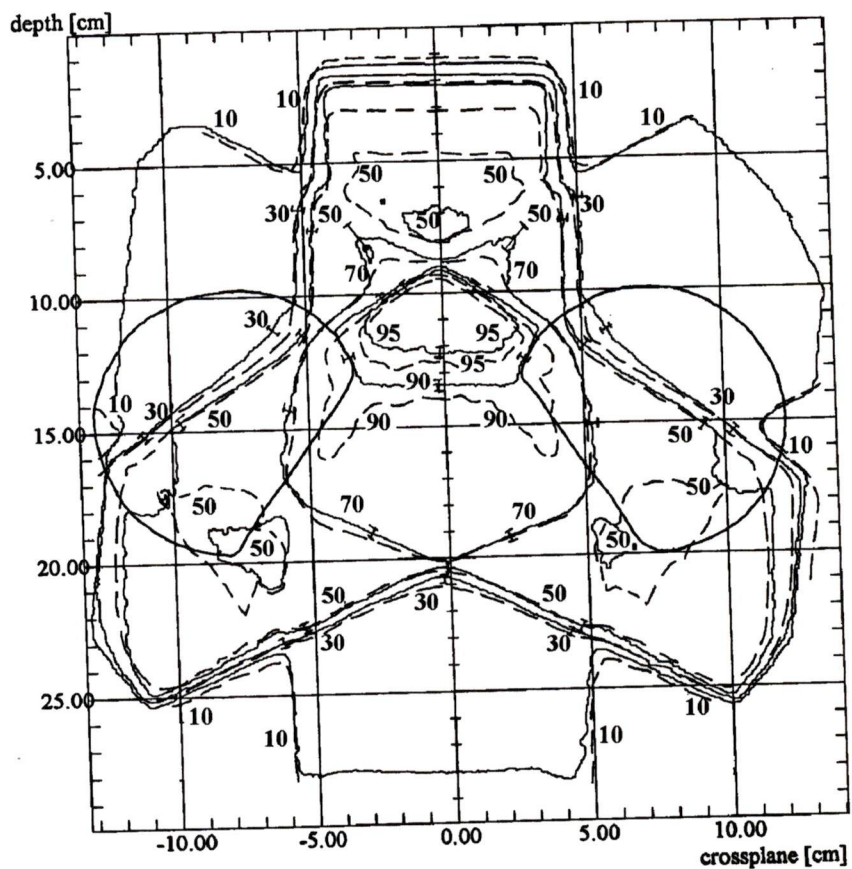


Figure 7-16: Odd isodose distribution for Phantom B as a result of a three field non-coplanar arrangement. Film distribution is indicated by the solid lines. The Target distribution is identified by the dashed lines. The power law correction algorithm has been employed in an attempt to correct for the presence of the inhomogeneous structure.

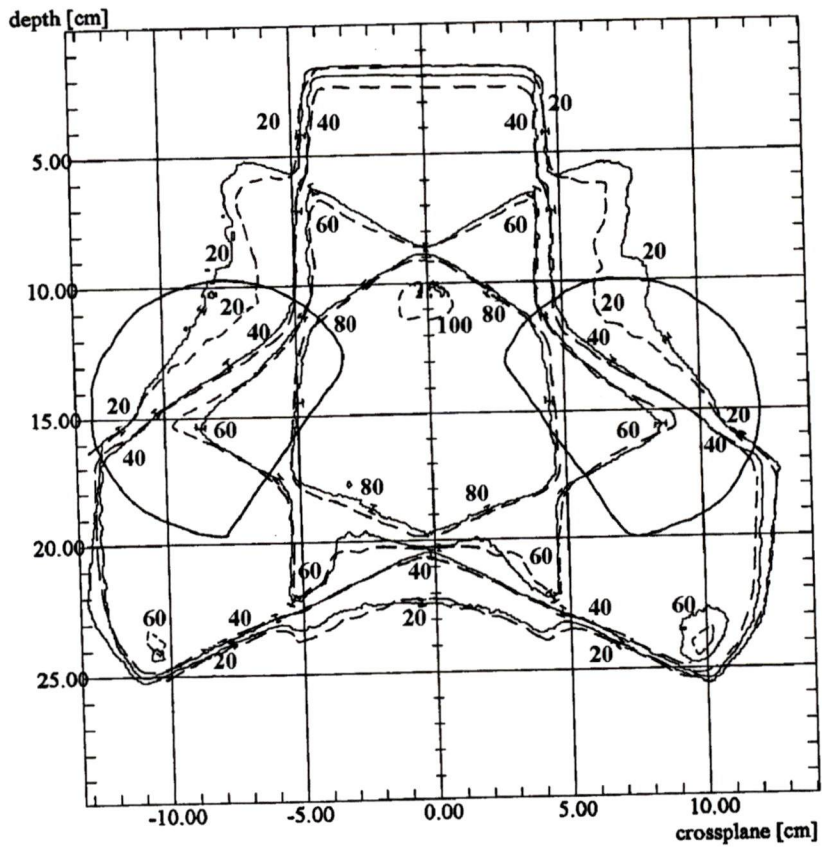


Figure 7-17: Even isodose distribution for Phantom B as a result of a three field non-coplanar arrangement. Film distribution is indicated by the solid lines. The Target distribution is identified by the dashed lines. The power law correction algorithm has been employed in an attempt to correct for the presence of the inhomogeneous structure.

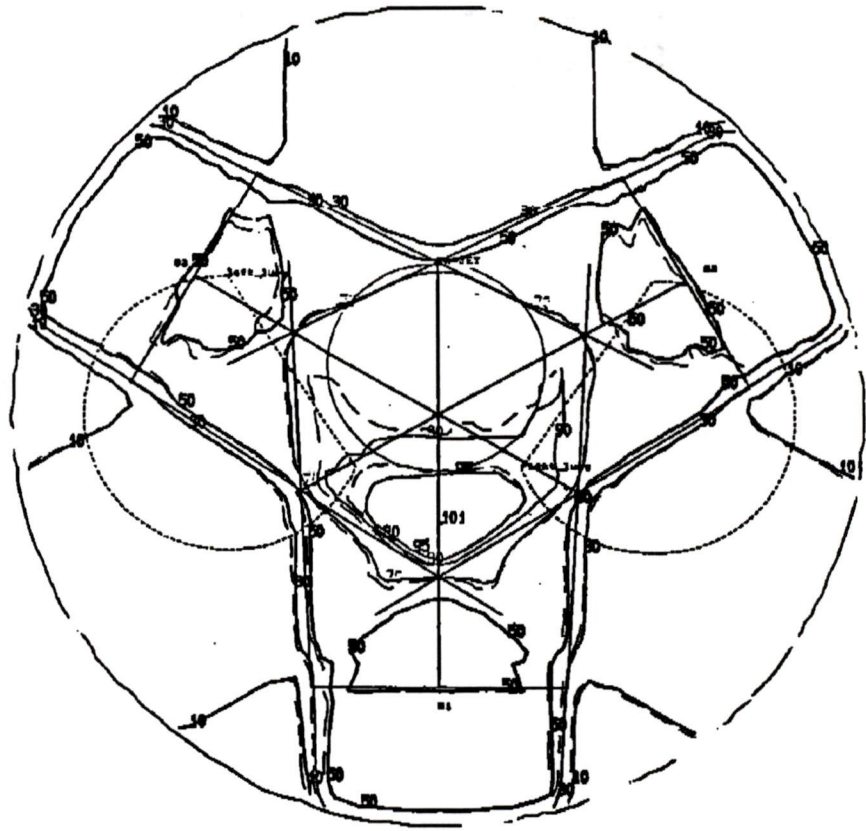


Figure 7-18: Target generated isodose distributions for the power law and ETAR inhomogeneity corrections for Phantom B and a three field, coplanar beam arrangement. The solid lines represent the ETAR distribution. The dashed lines represent the Power Law distribution.

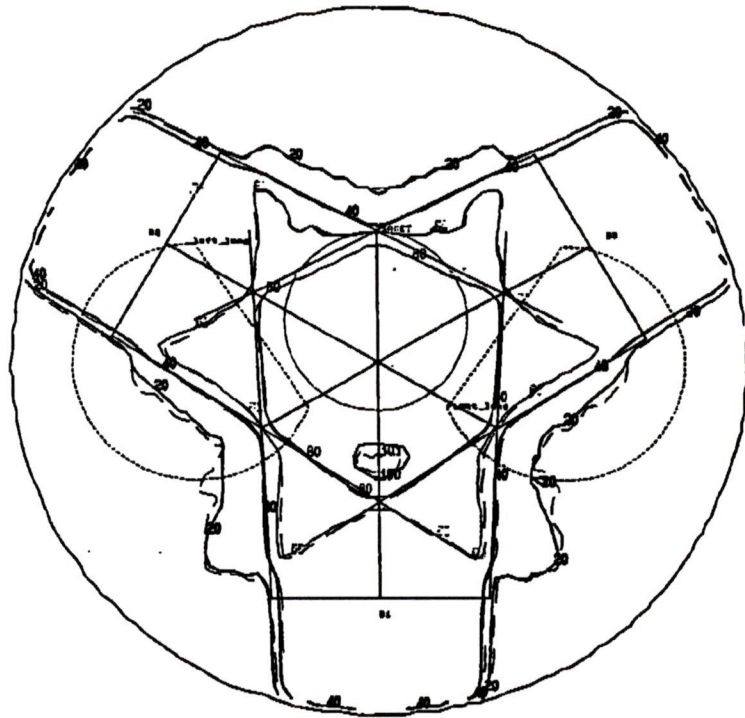


Figure 7-19: Target generated isodose distributions for the power law and ETAR inhomogeneity corrections for Phantom B and a three field, coplanar beam arrangement. The solid lines represent the ETAR distribution. The dashed lines represent the Power Law distribution.

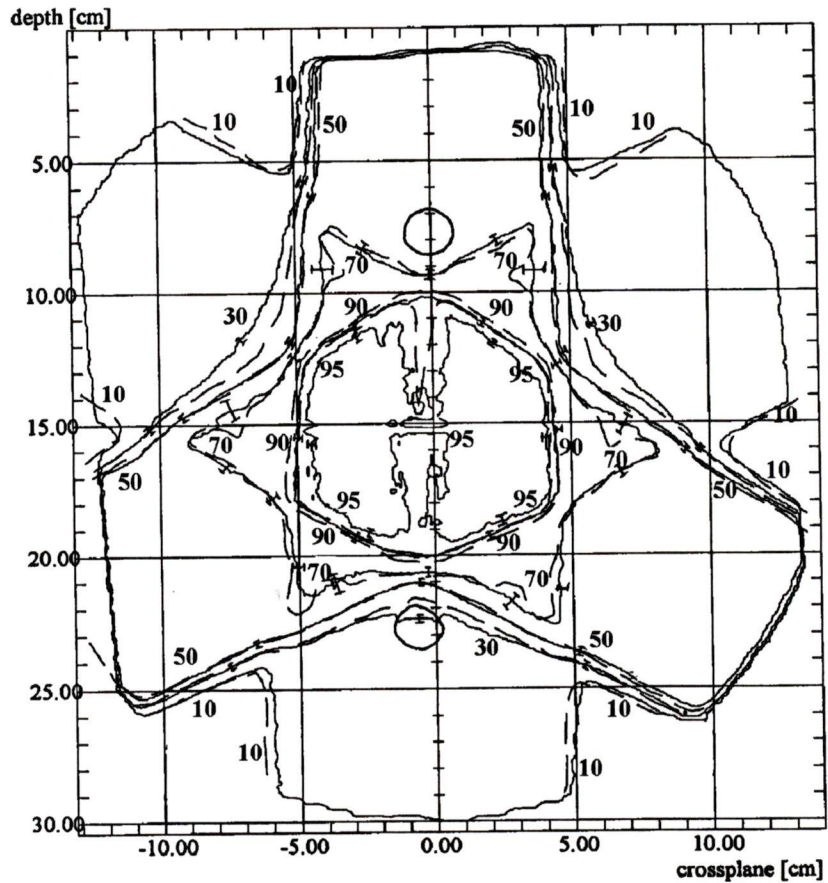


Figure 7-20: Odd isodose distribution for Phantom C as a result of a three field coplanar arrangement. Film distribution is indicated by the solid lines. The Target distribution is identified by the dashed lines. The equivalent path correction algorithm has been employed in an attempt to correct for the presence of the inhomogeneous structure.

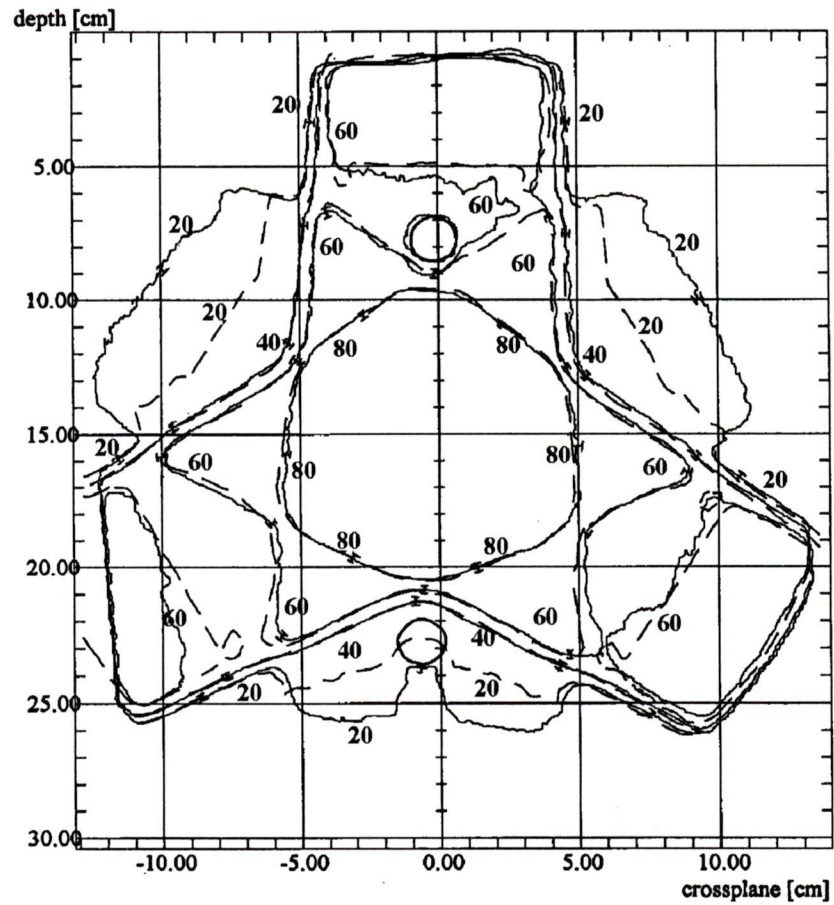


Figure 7-21: Even isodose distribution for Phantom C as a result of a three field coplanar arrangement. Film distribution is indicated by the solid lines. The Target distribution is identified by the dashed lines. The equivalent path correction algorithm has been employed in an attempt to correct for the presence of the inhomogeneous structure.

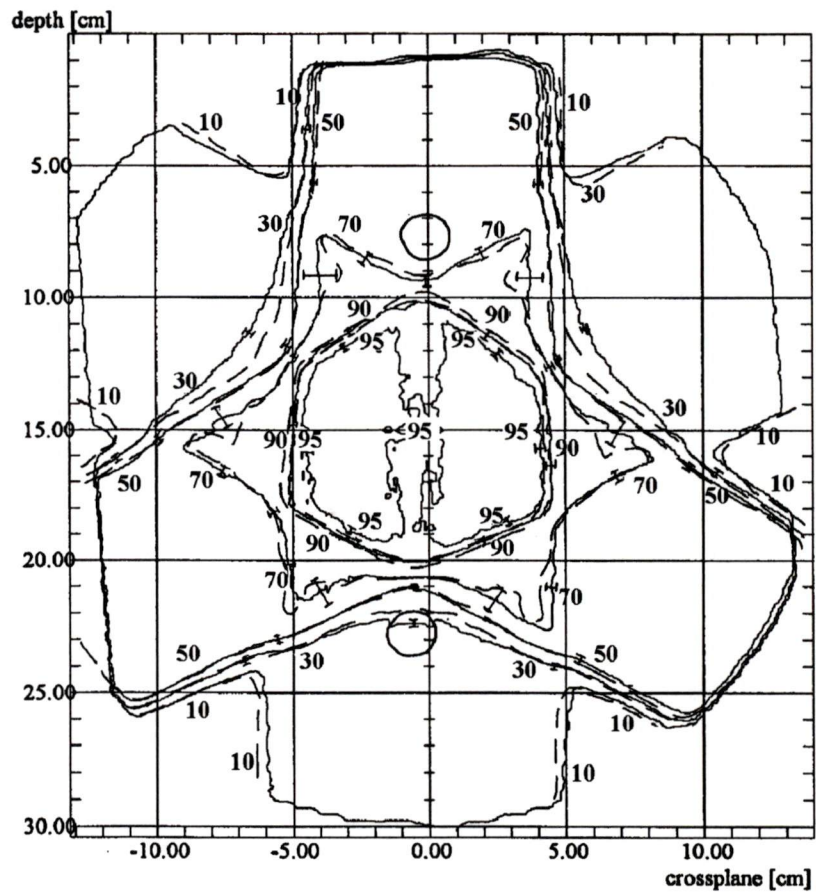


Figure 7-22: Odd isodose distribution for Phantom C as a result of a three field coplanar arrangement. Film distribution is indicated by the solid lines. The Target distribution is identified by the dashed lines. The power law correction algorithm has been employed in an attempt to correct for the presence of the inhomogeneous structure.

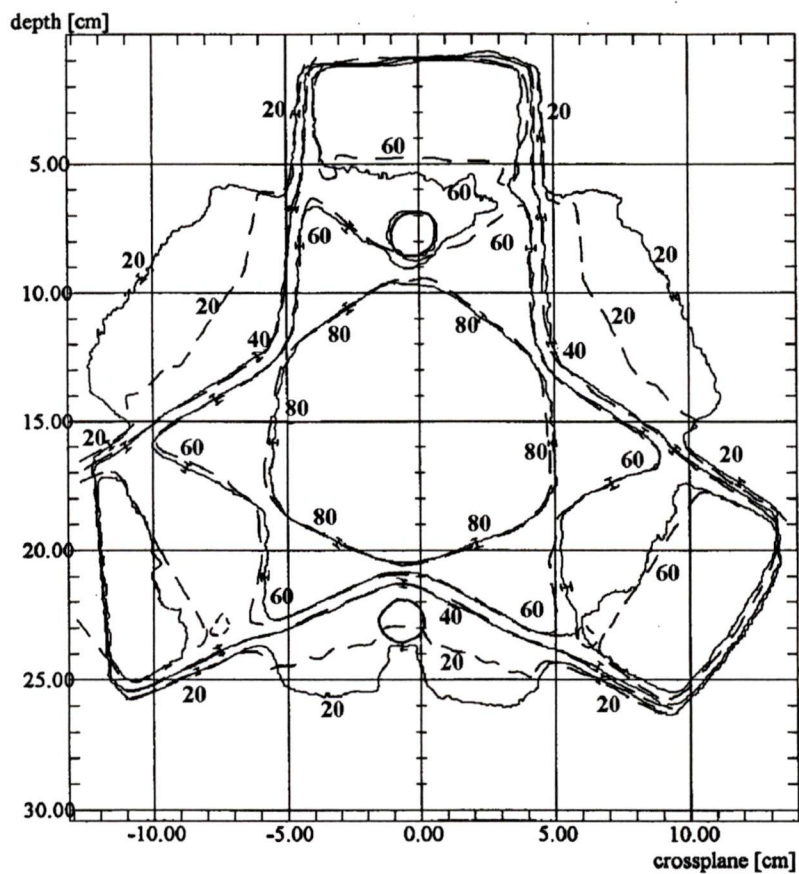


Figure 7-23: Even isodose distribution for Phantom C as a result of a three field coplanar arrangement. Film distribution is indicated by the solid lines. The Target distribution is identified by the dashed lines. The power law correction algorithm has been employed in an attempt to correct for the presence of the inhomogeneous structure.

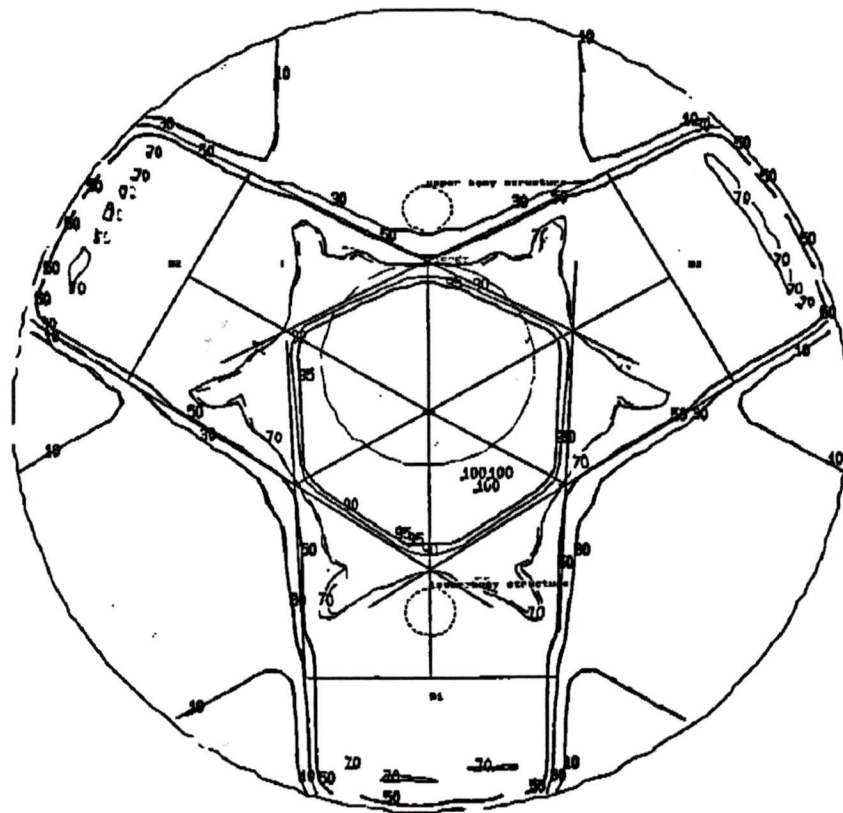


Figure 7-24: Target generated isodose distributions for the power law and ETAR inhomogeneity corrections for Phantom C and a three field, coplanar beam arrangement. The solid lines represent the ETAR distribution. The dashed lines represent the Power Law distribution.

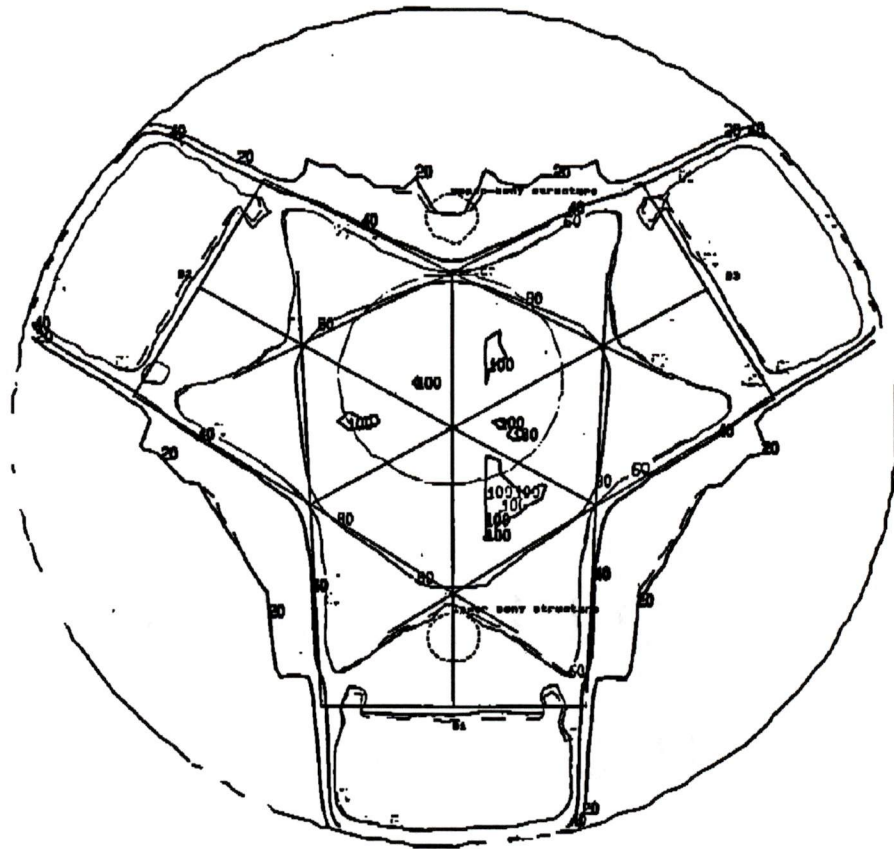


Figure 7-25: Target generated isodose distributions for the power law and ETAR inhomogeneity corrections for Phantom C and a three field, coplanar beam arrangement. The solid lines represent the ETAR distribution. The dashed lines represent the Power Law distribution.

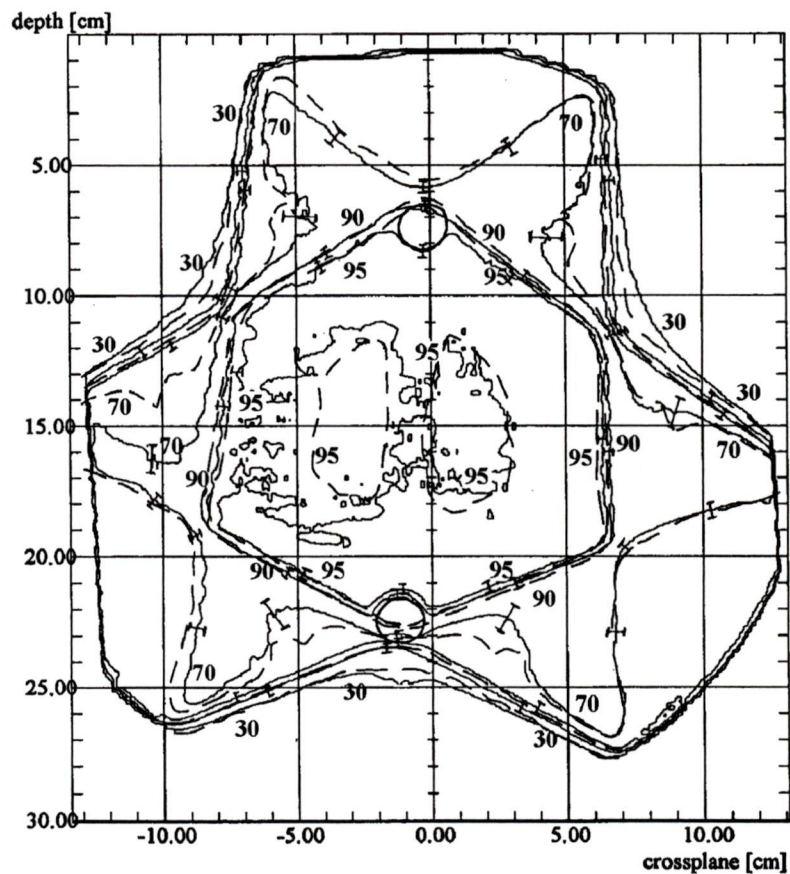


Figure 7-26: Odd isodose distribution for Phantom D as a result of a three field coplanar arrangement. Film distribution is indicated by the solid lines. The Target distribution is identified by the dashed lines. The equivalent path correction algorithm has been employed in an attempt to correct for the presence of the inhomogeneous structure.

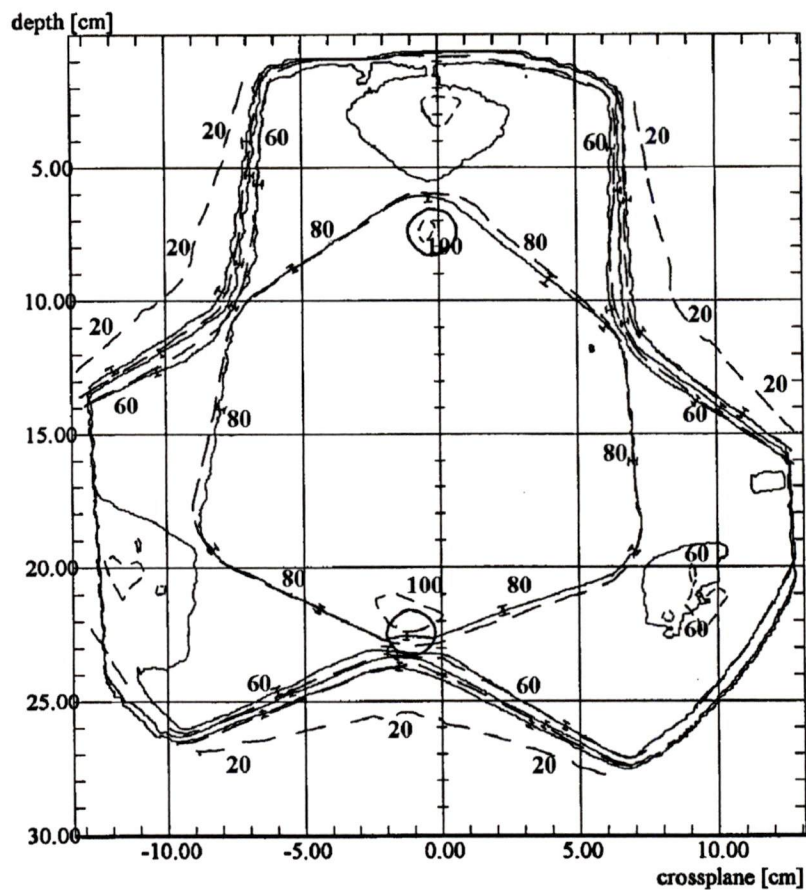


Figure 7-27: Even isodose distribution for Phantom D as a result of a three field coplanar arrangement. Film distribution is indicated by the solid lines. The Target distribution is identified by the dashed lines. The equivalent path correction algorithm has been employed in an attempt to correct for the presence of the inhomogeneous structure.

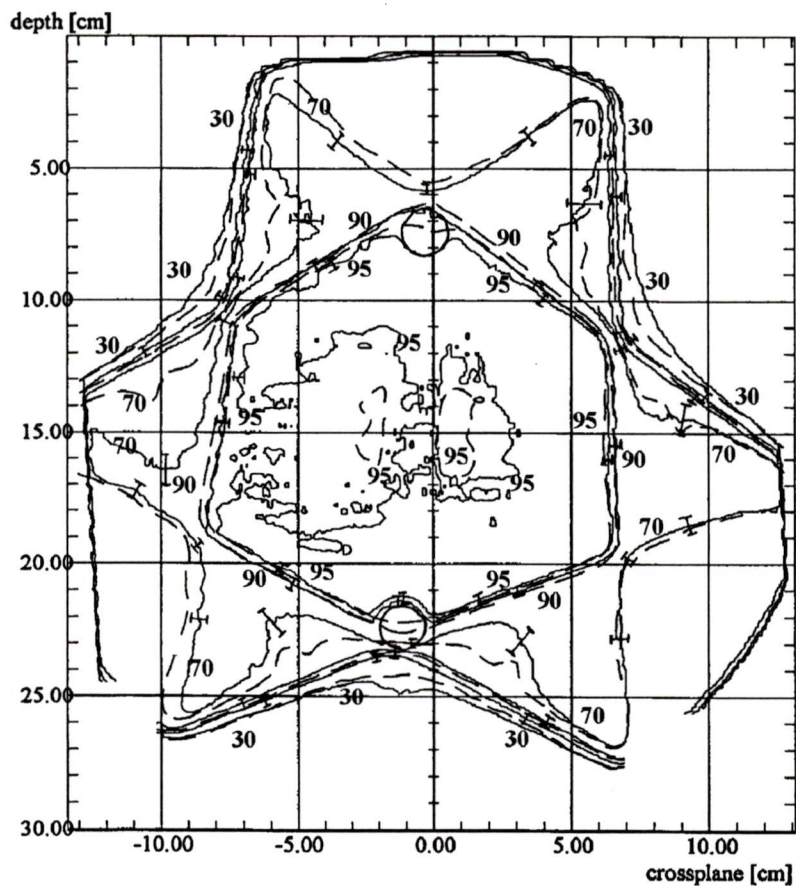


Figure 7-28: Odd isodose distribution for Phantom D as a result of a three field coplanar arrangement. Film distribution is indicated by the solid lines. The Target distribution is identified by the dashed lines. The power law correction algorithm has been employed in an attempt to correct for the presence of the inhomogeneous structure.

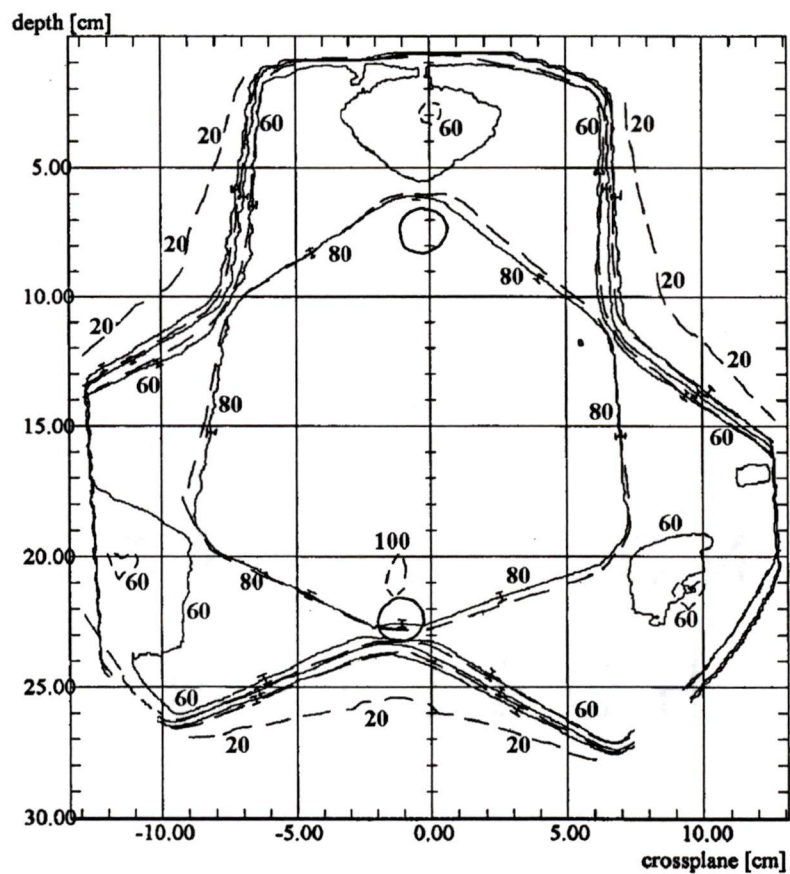


Figure 7-29: Even isodose distribution for Phantom D as a result of a three field coplanar arrangement. Film distribution is indicated by the solid lines. The Target distribution is identified by the dashed lines. The power law correction algorithm has been employed in an attempt to correct for the presence of the inhomogeneous structure.

8. DISCUSSION

In this section, the trends in the data that have been presented in the results section of this thesis will be discussed. The format of this discussion is as follows: Initially, general observations that are drawn from the collection of isodose distributions that are seen in chapter 7. Specific discrepancies that can be seen in the correlation between the measured isodose distributions and those predicted by Target are then identified and discussed.

The preliminary work that was conducted to evaluate the validity of using film as a dosimeter to measure dose distributions within phantoms, consisted of obtaining a calibration curve that would be used to relate the relative film density to dose deposition. This curve was then used to obtain a number of open field isodose curves for comparison with the target generated distributions, over a range of field sizes. Good correspondence was generally achieved between the measured distributions and the ones predicted by the Target software, as exemplified by Figures 7-1 through 7-5, indicating that adequate film calibration can be achieved for a range of open field sizes.

Four phantoms, one homogeneous and the other three having a different inhomogeneity inclusion in each, were subjected to a three field, coplanar beam configuration (see Table 5-1). Phantoms A and B were also subjected to a three-field non-coplanar arrangement (see Table 5-2). The isodose distribution along the mid-plane of the phantom, perpendicular to its long axis, was measured and compared to the distribution predicted by the Target software. In general, with a few exceptions to be discussed, good correspondence was obtained between these distributions.

There was little variation observed between the experimentally measured distributions and the Target distributions for all three inhomogeneity correction algorithms that are included in the Target software, particularly for the coplanar beam arrangement. The degree of correspondence between the distributions for the coplanar beam arrangement did not come as a surprise, as the coplanar aspect of the GE Target treatment planning system has been used in the clinical setting for a number of years. Furthermore, there was virtually no difference between the isodose distributions associated with the

ETAR correction algorithm and the one for the power law correction. Any conclusions that are drawn with regard to the power law correction method can be assumed to apply equally well to the ETAR algorithm. However, this is only true for an “infinite” phantom. All of the phantoms used in this project are “infinite” in the sense that the cross section of the inhomogeneity remains constant along the direction that is perpendicular to the plane of measurement.

The correspondence between our measured distributions and those determined by GE Target are only valid for large phantoms with relatively large inhomogeneity inclusions. There may be discrepancies between the measured and predicted isodose distributions that would arise in situations that have not been investigated in this work. Such situations may be found in areas such as the sinus regions, where there are many small air cavities surrounded by a limited amount of tissue. However, the level of correspondence that has been achieved with this work has instilled enough confidence in the Target algorithms to warrant its application in the clinical setting. As a result we have incorporated the 3-D non-coplanar calculation algorithms into clinical operations where they are routinely used for treatment planning in such areas as the prostate and the thoracic regions.

The largest discrepancies between the measured and Target generated distributions are found in the low gradient regions. Such regions are associated with the lower percentage isodose curves and in regions which lie just above the shoulder portion of the combined, three-field isodose distribution. An example of the latter case would be the 70% curves seen in all three-field distributions. For points in these low gradient regions, a small error in the determination of the percentage value will manifest itself in a relatively large variation in its spatial location. The three-field, non-coplanar isodose distribution for Phantom A, shown in Figure 7-8, represents a typical illustration of this trend. The regions to notice are identified by the 70% curve for a depth of about 8 cm with crossplane distance of about ± 3 cm. The same general trend in the 70% decrement line can be seen for Phantom B coplanar (Figure 7-10) and non-coplanar (Figure 7-14) distributions. The 60% isodose distribution for Phantom B show similar tendencies. These curves are illustrated in figures 7-11 (coplanar) and 7-15 (non-coplanar).

The most significant differences in the inhomogeneity correction methods are seen in the coplanar (Figure 7-10 to 7-13) and non-coplanar (Figure 7-14 to 7-17) distributions for Phantom B. In particular, the 95% isodose line in the vicinity of the lung-like inclusion. These regions of interest are identified with a depth of 13 cm and a crossplane distance of ± 3 cm. Notice that the 95% isodose curve, determined using the equivalent path length correction method (Figure 7-14), is well inside the inhomogeneous region, whereas both the experimental and the power law 95% isodose curves (Figure 7-16) are located outside the inhomogeneity, towards phantom center. The power law 95% decrement line is, within experimental error, almost coincident with the experimentally measured 95% line.

The difference between the location of the power law and the equivalent path 95% decrement lines in this region can be attributed to their respective algorithms. Recall that the equivalent path length algorithm is only able to account for the presence of inhomogeneities that lie somewhere along the path of the beam, without accounting for the distance between the boundary of the inhomogeneity and the calculation point. The power law algorithm makes its correction by considering where the calculation point is with respect to the boundary of the inhomogeneity using weighted TAR values. The result will be, for example, that calculation points that lie downstream from a low density inhomogeneous structures will receive more dose when the power law algorithm is used than when the equivalent path method is employed. In effect, the 95% isodose curve will lie farther from a low density inclusion when the power law correction method is used than when the equivalent path length algorithm is employed. This is the reason for the difference in the 95% isodose curves mentioned above.

Previously, we mentioned that the general trends discussed here are only applicable to situations where large phantoms containing large inhomogeneous structures are modeled and that discrepancies between measured and predicted results may be obtained where this is not the case. Evidence to support this claim can be observed by examining the isodose distributions generated using Phantom D (Figures 7-26 to 7-29). Notice that, in general, good correspondence is observed between the measured and Target predicted isodose distributions. However, a large discrepancy can be seen in the 90% and 95%

distributions in the immediate vicinity of the low density inclusion located at a depth of about 22 cm and a crossplane distance of about -1 cm in Figures 7-26 and 7-28. A similar discrepancy can be seen for the 95% decrement line where the depth is about 7 cm and the crossplane distance is about 0 cm.

Notice that there is not much difference in the spatial location of the isodose curves for any of the Target inhomogeneity correction algorithms in this region (depth = 22 cm and off axis = -1 cm, Figures 7-26 and 7-28), even though the prediction based on the power law method is closer to the experimentally measured distribution. This leads us to believe that problems may arise with the corrections predicted by the Target software in the local region of smaller, low density inclusions, particularly when the 90 or 95% isodose curves fall within or near small, low density inhomogeneities. Further work will be required to fully investigate this phenomenon.

9. CONCLUSIONS

The work presented in this thesis represents an investigation into the ability of the GE Target software system to accurately model dose distributions, within phantoms that contain relatively large inhomogeneous structures, for both coplanar and non-coplanar beam arrangements.

The four phantoms that were used all had a similar right cylindrical geometry with common exterior dimensions. These phantoms were constructed as a series of disks so that sheets of film could be sandwiched between the disks and used to measure the dose distribution in planes perpendicular to the long axis. The first phantom, Phantom A, is composed of a homogeneous, water equivalent material. The other three phantoms, Phantoms B through D, are constructed out of the same water equivalent material, but each contains a different type of inhomogeneity inclusion. Phantom B contains simple lung-like structures, Phantom C has a pair of bone-like inhomogeneities included, and Phantom D contains a pair of small air cavities. All inhomogeneities run the length of the phantom.

The Vancouver Island Cancer Centre 6 MV Linac was used to obtain all of the experimental data for this project. The data essentially consists of isodose distributions, representing the dose deposition pattern within the phantoms for a variety of beam arrangements. These distributions were obtained with the Wellhofer densitometer system.

The GE Target software system was used to predict the distributions that would result from the relevant experimental setup. The inhomogeneity correction algorithms, incorporated into the Target software, were used to generate isodose distributions so that a comparison could be made between these distributions and those experimentally measured.

An analysis of the errors that exist in both the experimental method and the ones that are inherent in Target was completed before comparisons were made between measured dose distributions and those predicted by the Target system. This analysis revealed that although the Target predictions are based on the relatively simple Milan/Bentley beam model, the errors inherent in such a model are relatively small. So

small in fact that there will not be any error bars visible on the isodose distributions generated by the Target software. The most significant errors associated with the experimental method are those due to reproducibility. The magnitude of these errors are dependent on the percent value of the isodose curve and on its spatial location.

Generally, we found that there was good correspondence between the Target predicted isodose distributions and the experimentally measured ones for both the coplanar and non-coplanar configurations. However, there were specific situations where there is a relatively large discrepancy between the two distributions. These situations correspond to points that are in shallow gradients of the distribution, and in the penumbral region of the beams.

There was very little variation in the distributions predicted by any of the inhomogeneity correction algorithms. The largest and most significant was seen in the corrections to the isodose distributions within the lung-like regions of Phantom B for both the coplanar and non-coplanar beam configurations. The power law (and also the ETAR) method provided distributions that, within experimental error, nearly matched those measured experimentally.

Although good correspondence was achieved for most of the isodose distributions, there is the occasional discrepancy between the power law correction isodose distribution and those measured experimentally. This may be due to the fact that the experimental error bars are based on the reproducibility achieved using seven films and so it is possible that a single measurement may lie outside this range. Alternatively, this discrepancy may be due to an inherent limitation in the correction algorithm. However, even though there are some regions where the Target isodose curves lie just beyond the range of experimental measurement, they are close enough to count as a match, especially when we consider that such regions are in a low gradient section of the overall distribution.

The level of correspondence that has been achieved with this work has provided enough confidence in the Target algorithms to warrant its application in the clinical setting. As a result we have incorporated the 3-D non-coplanar calculation algorithms into clinical operations where they are routinely used for treatment planning in such areas as the prostate and the thoracic regions among others.

It should be noted, however, that the correspondence between our measured distributions and those determined by Target are only valid for large phantoms with relatively large inhomogeneity inclusions. There may be discrepancies between the measured and predicted isodose distributions that would arise in situations where this is not true. Evidence supporting this statement was found using Phantom D, the one with the small air cavity inclusions. It was illustrated that when the beam size and geometrical arrangement place the 90% and 95% isodose curves in the vicinity of small, low density inhomogeneities, none of the inhomogeneity correction algorithms could bring the predicted distribution in line with those measured experimentally. Further work will be required to fully investigate this phenomena, since similar situations may arise in areas such as the sinus area where small air cavities exist.

REFERENCES

- Antolak JA 1992 Evaluation and Modification of Electron Beam Treatment Planning Algorithms *PhD thesis* University of Alberta
- Armstrong JG, Burman C, Leibel S, Fontenla D, Kutcher G, Zelefsky M and Fuks Z 1993 Three-Dimensional Conformal Radiation Therapy May Improve the Therapeutic Ratio of High Dose Radiation Therapy for Lung Cancer *Int. J. Radiation Oncology Biol. Phys.* **26** 685
- Batho HF 1964 Lung Corrections in Cobalt 60 Beam Therapy *J. Can. Assoc. Radiol.* **15** 79
- Beard CJ, Kaplan ID, and Coleman CN 1993 The Challenge for Conformal Therapy for Prostate Cancer *Int. J. Radiation Oncology Biol. Phys.* **26** 705
- Benk VA, Adams JA, Shipley WU, Urie MM, McManus PL, Efird JT, Willett CG, and Goitein M 1993 Late Rectal Bleeding Following Combined X-Ray and Proton High Dose Irradiation for Patients with Stages T3-T4 Prostate Carcinoma *Int. J. Radiation Oncology Biol. Phys.* **26** 551
- Epstein BE and Hanks GE 1993 Radiation Therapy Techniques and Dose Selection in the Treatment of Prostate Cancer *Seminars in Radiation Oncology* **3** 179
- GE Target 2 Physics Manual 1993 IGE Medical Systems Ltd. U.K.
- Hanks GE 1993 Conformal Radiation in Prostate Cancer: Reduced Morbidity with Hope of Increased Local Control *Int. J. Radiation Oncology Biol. Phys.* **25** 377
- Horton JL 1987 Handbook of Radiation Therapy Physics
Englewood Cliffs, Prentice Hall.
- Johns HE, Cunningham JR 1983 The Physics of Radiology, 4th edition.
Springfield Illinois, Thomas.
- Leibel SA, Ling CC, Kutcher GJ, Mohan R, Cordon-Cordon C and Fuks Z 1991 The Biological Basis for Conformal Three-Dimensional Radiation Therapy *Int. J. Radiation Oncology Biol. Phys.* **21** 805
- Milan J and Bentley RE 1974 The Storage and Manipulation of Radiation Dose Data in a Small Digital Computer *British Journal of Radiology* **47** 115-121

- Mott DJ 1994 Error Propagation Through the Bentley-Milan Dose Algorithm on Target 2
Proceedings of the XI International Conference on the use of Computers in
Radiation Therapy. Manchester UK March 20-24
- Porter AT and Forman JD 1994 The role of radiotherapy in the management of locally
advanced prostate cancer *Current Oncology* **1** 5
- Sandler H 1993 Can Conformal Radiation Therapy Reduce Side Effects *Radiology &
Imaging Letter* **13** 19
- Sandler HM, McShan DL, and Lichter AS 1992 Potential Improvement in the Results of
Irradiation for Prostate Carcinoma using Improved Dose Distribution *Int. J.
Radiation Oncology Biol. Phys.* **22** 361
- Sandler HM, Perez-Tamayo C, Haken RKT and Lichter AS 1992 Dose Escalation for
Stage C(T3) Prostate Cancer: Minimal Rectal Toxicity Observed using Conformal
Therapy *Radiotherapy and Oncology* **23** 53
- Sontag MR and Cunningham JR 1977 Corrections to Absorbed Dose Calculations for
Tissue Inhomogeneities *Med Phys* **4** 431
- Tait D 1990 Conformal Therapy *British Journal of Cancer* **65** 702
- Wellhofer Dosimtrie Assorted Technical Documentation.
- Zelefsky MJ, Leibel SA and Fuks Z 1993 Conventional External Beam Radiation Therapy
for Prostatic Cancer: Where Do We Go From Here? *Int. J. Radiation Oncology
Biol. Phys.* **26** 365

APPENDIX A: BEAM GENERATING HARDWARE

There are various devices that are used to deliver external beam treatment to patients. The most common are the Cobalt Teletherapy Unit and the Medical Linear Accelerator. These devices are similar in that they both consist of a stand, gantry, head, and treatment couch. Figure A-1 illustrates the basic components that are common to both machines and the motions of which each is capable. Despite the similarities, their operation is fundamentally different. This section will describe both devices.

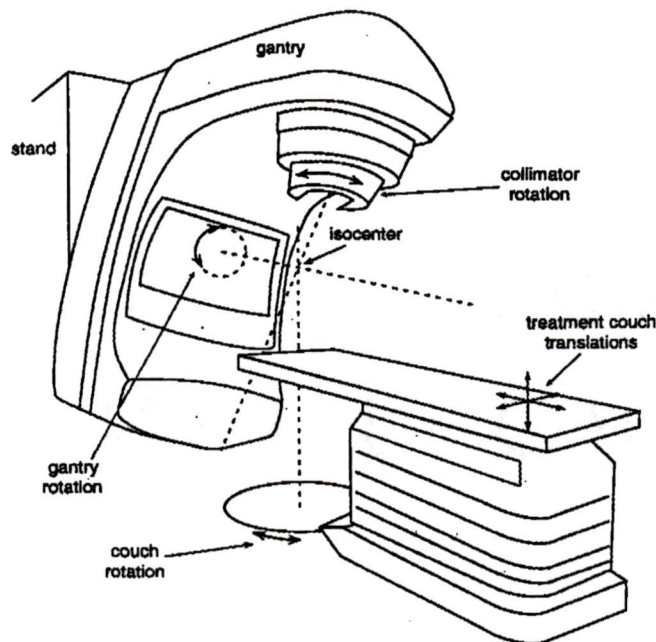


Figure A-1: Illustration of the components that make up a typical medical linear accelerator or a cobalt unit. The illustration is actually a representation of a linac, but the components are common to both linac and cobalt teletherapy units (Antolak 1992).

Cobalt Teletherapy Unit:

The ability of the cobalt teletherapy unit to generate a beam of photons is due to the radioactive decay of a cobalt source. Typically, a cobalt source consists of radioactive ^{60}Co pellets that are doubly encased in a hollow stainless steel cylinder. This steel cylinder is then encased in a cylindrical tungsten shell. Overall, the source cylinder will be about 5 cm long and about 1.5 cm in diameter.

Radioactive ^{60}Co is produced by bombarding ^{59}Co with thermal neutrons in a nuclear reactor. The resulting ^{60}Co will decay, with a 5.26 year half-life, according to the following decay scheme:

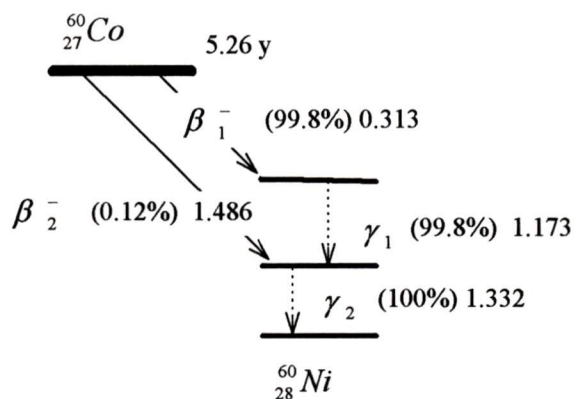


Figure A-2: Cobalt 60 decay scheme.

Notice that the majority of the disintegration (99.8%) are of the β^- type. This decay path produces two gamma's. These two gamma's provide the useful radiation from the cobalt teletherapy unit.

The photon beam emanating from the head of the cobalt machine can be approximated as monoenergetic, with an energy of 1.25 MeV $\left(= \frac{1.33 + 1.17}{2} \right)$.

The cobalt source is stored in a lead shielded enclosure within the gantry of the machine. When the beam is required, the source is forced pneumatically from its shielded enclosure. The photon beam will then emerge through a set of collimators. The collimators consist of two sets of interleaved, depleted uranium jaws. Each set of jaws

can be set independently to provide a rectangular beam. The isocenter for the cobalt machine is typically 80 cm from the source.

Medical Linear Accelerator:

Figure A-1 illustrates the basic modules which make up a typical medical linear accelerator (linac). The stand, gantry and treatment couch are the three major modules that are common to every linac.

The typical linac stand contains a source of microwave power, a waveguide structure for transmitting the microwave power from the stand to the gantry and ultimately to the accelerator structure, a circulator which is used to isolate and protect the microwave source from microwaves that can be reflected from the accelerator structure, and a water cooling system.

There are two types of microwave sources that are used. A magnetron is used in linacs where electrons are accelerated up to about 15 MeV. A klystron is used in linacs operating at energies greater than about 15 MeV.

The microwave power that is generated using either the klystron or the magnetron is transported to the accelerating structure in the gantry through a series rectangular waveguides. Connections between the waveguide and the gantry accelerating structure can cause some of the microwaves to be reflected back towards the microwave generator. If the reflected waves are allowed to reach the microwave generator, they could cause instabilities and damage. To prevent this, a circulator is placed between the microwave generator and the accelerating structure. Basically, a circulator acts as a one way switch allowing microwaves to travel from the microwave generator to the accelerating structure and absorbing microwaves that have been reflected from the accelerating structure.

Referring to Figure A-1, the structure known as the gantry is attached to the stand and is free to rotate about an axis that runs through the isocenter of the machine. The components that are contained in the gantry are: the accelerating structure, the electron gun, the beam bending magnet and the treatment head.

Accelerating structures consist of a long series of evacuated microwave cavities. The primary function of this structure is to convert the energy of the microwaves generated by the magnetron or the klystron to kinetic energy of electrons traveling the

length of the accelerating structure. The first few cavities vary in size and are used to bunch groups of electrons together in a manner similar to that employed by the buncher section of the klystron. The remainder of the cavities are of similar size and are used primarily to increase the energy of the electrons. Initially, the electron energy is increased by increasing the electron velocity. Once the velocity becomes relativistic, energy gain is achieved through an increase in mass.

There are two types of accelerating structures: traveling wave and standing wave. In a traveling wave accelerator, electrons “ride” on the wave much like a surfer will ride on a wave. Bunches of electrons are injected into the accelerating structure via an electron gun. As the electrons enter the accelerating structure, they are subjected to a sinusoidally alternating electric field. Recall that it will be the negative portion of the alternating electric field which will accelerate the electrons. Consequently, electrons that enter the accelerating structure when the electric field is in its positive portion of its cycle will be slowed by the electric field. Electrons which enter the structure when the electric field is zero will not be affected by the field and electrons entering the cavity in the negative portion of the field cycle will be accelerated by the field. Therefore, as the electrons proceed down the structure they will tend to bunch together, since some of them will be accelerating, some decelerating and some unaffected by the electric field.

If a hollow cylindrical tube is used as the accelerating structure, the wave will propagate faster than the electrons will be able to keep up. In order to slow the wave down, the waveguide is loaded with disks to form a corrugated wave guide. As a result, a series of cavities are formed where a large electric field is established that are suitable for electron acceleration. The wave is allowed to propagate from one end of the structure to the other, carrying electrons with it. Once the wave has carried the electrons along the length of the accelerating structure, it must be absorbed.

The other type is the standing wave accelerating structure. In this type of structure, microwaves are allowed to reflect from both ends of the cavity setting up a standing wave pattern. The accelerator structure is similar to the traveling wave one in that it consists of a series of cavities. The difference is that some of the cavities will act as nodes of the standing wave. The node cavities will not contribute any energy to the

advancing groups of electrons and so can be moved out to the side of the overall structure. The result is that the standing wave structures will tend to be shorter than the traveling wave ones, for the same energy imparted to electrons. In this type of structure, the microwave power can be fed in at any point. Typically, the microwaves are fed in at the center of the waveguide.

The electrons that are injected into the front end of the accelerating structure originate from an electron gun. All electron guns operate on the principle of thermionic emission. There are two types of guns that are common to medical linear accelerators: the diode gun and the triode gun. The diode gun, illustrated in Figure A-3, is the type of gun that are used on the linear accelerators at the Vancouver Island Cancer Centre (i.e.: Philips).

There is a large potential gradient between the cathode and the anode. This potential gradient along with the focusing cup focuses the thermionically emitted electrons from the cathode, through the hole in the anode and into the accelerating waveguide. The potential difference between the cathode and the anode is about 50 kV. The high voltage pulses that drive the gun are supplied by the pulse forming network.

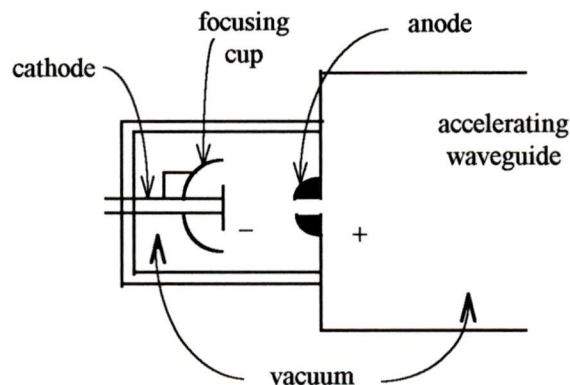


Figure A-3: Diode Gun.

As the electrons leave the accelerating structure, they have to be re-directed through a 90° angle so that they can be used to strike either a target or scattering foil. Re-direction is achieved by using a beam bending magnet through either 90° or 270°.

A 90° bending magnet will lead to a non-uniform beam cross section as the beam exits the magnet. This is due to the fact that in a 90° magnet, the higher energy electrons will not be deflected as much as the lower energy ones.

In a 270° bending magnet the lower energy electrons will be deflected through a smaller radius than the higher energy ones. The result is that all of the electrons will be brought back to the same position, angle and beam cross section as they were when they left the accelerating structure. Such a magnet is referred to as achromatic.

When the electrons leave the beam bending magnet, they enter the treatment head. This part of the machine contains a variety of beam shaping and monitoring devices. Figure A-4 illustrates a typical linac treatment head configuration for generating a photon beam.

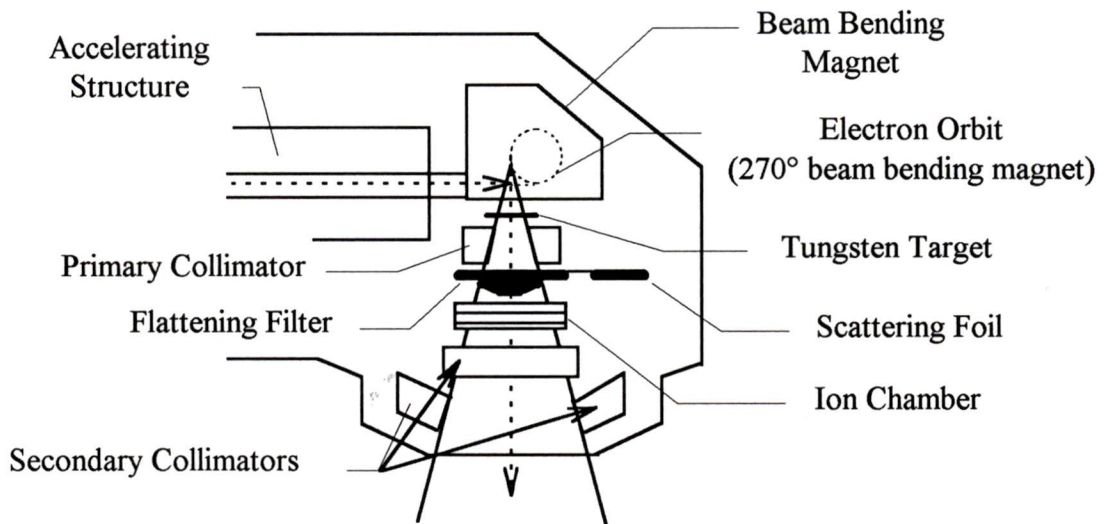


Figure A-4: Cross sectional view of a typical linear accelerator head.

As the electron beam enters the treatment head, it will strike the tungsten target. At this point, the electrons interact with the target and, through the bremsstrahlung process, generate a photon spectrum. A primary collimator is then used to reduce the size of this emitted field. The primary collimator is not adjustable, and will define the largest field available. The beam from the target will be forward peaked. This means that the maximum intensity will be along the central axis of the beam. The forward peaked beam, emerging from the primary collimator, then passes through a flattening filter. The flattening filter is thicker in the center with the thickness tapering off towards the filter

edges to match the beam intensity profile. After the beam passes through the flattening filter, it will have a flatter, uniform profile than it did when it went into this filter. Essentially, it is this field that is used for treatment. After this point, the photon beam passes through an ion chamber and the secondary collimators and emerges from the head. The ion chamber is used to monitor beam uniformity and energy output. It is the adjustable secondary collimators that are used to define the size of the photon field that is used to treat the patient. These are essentially all of the components that are contained in the treatment head if an open field beam is used. If wedges, blocks or beam compensators are used, they will be mounted on a tray that slides into slots just below the secondary collimators.

For the generation of an electron beam, the same basic components are used, but the tungsten target is no longer required. Instead the electron beam, emerging from the beam bending magnet passes through the primary collimator. Also, the flattening filter is replaced by a scattering foil. The scattering foil is used to convert the narrow electron beam, emerging from the beam bending magnet, to a broad uniform electron field which can be used for treatment. The electrons pass through the same ion chamber used for photon beams and on past the secondary collimators. Most medical linac also use an electron applicator, mounted in the accessory tray. This device is used to further collimate the electron field and to supplement the beam profile through electron interactions with the applicator.

APPENDIX B: TISSUE AIR RATIO DETERMINATION

(Johns and Cunningham 1983)

Figure B-1 should be consulted to help in the visualization of the relevant quantities that are required to define the tissue air ratio.

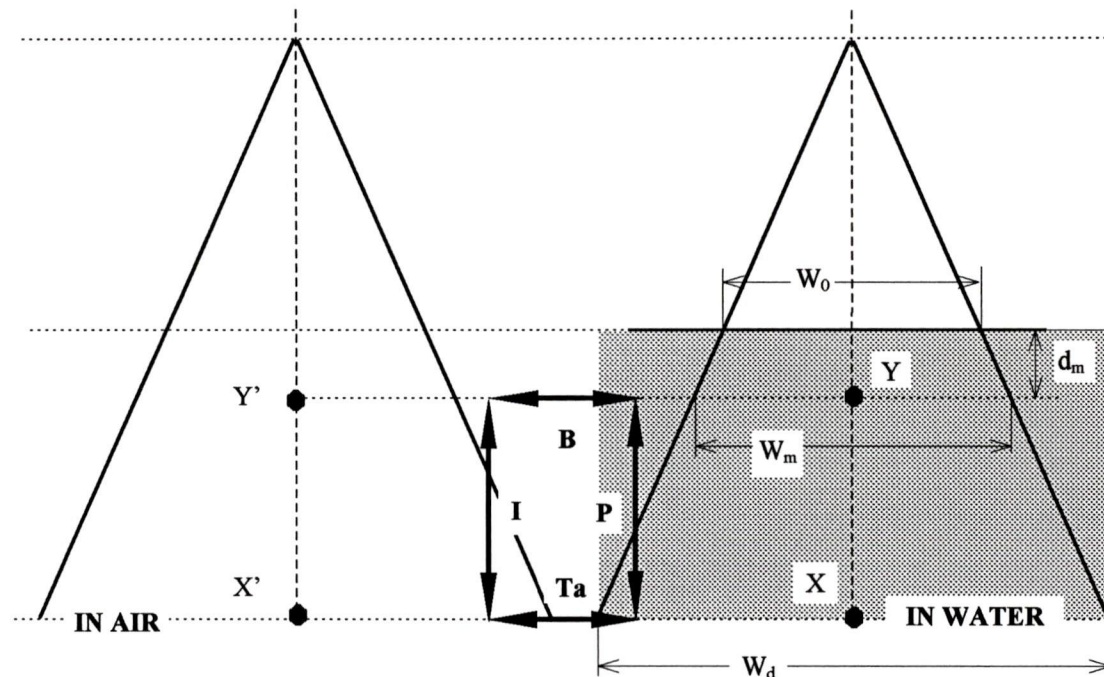


Figure B-1: Diagram illustrating the relevant quantities that are needed to discuss Tissue Air Ratio

Figure B-1 illustrates of two beams. The beam on the right side of the figure is incident on a water surface that is SSD from the effective source. The field width at the surface of the water is defined to be W_0 . The field width at d_{max} is defined as W_m . The point, along the central axis of the beam at d_{max} , is labeled Y . The field size at a distance d from the water surface, along the central axis is labeled W_d . This point has been identified as X . The drawing on the left side of Figure B-1 is for the same configuration with the exception that there is no water present, only air. Points, in air, that correspond to X and Y are identified as X' and Y' , respectively. Dose values, corresponding to X , Y , X' , and Y' are defined as D_X , D_Y , $D_{X'}$, and $D_{Y'}$, respectively. It should be noted that the “in air” measurements ($D_{X'}$, $D_{Y'}$) have to be done using a probe having a large enough build-up cap to ensure that electronic equilibrium is achieved.

From these basic quantities, we are now in a position to define a few functions that are commonly used in dose calculations:

BACKSCATTER FACTOR (B):

The factor by which the radiation dose is increased due to radiation that is scattered back from the phantom:

$$B(W_m, h\nu) = \frac{D_Y}{D_{Y'}}$$

Equation B-1

TISSUE AIR RATIO (Ta):

The ratio of the dose at X to the dose at X':

$$Ta(d, W_d, h\nu) = \frac{D_X}{D_{X'}}$$

Equation B-2

PERCENTAGE DEPTH DOSE (P):

Usually expressed as a percentage with respect to the reference point Y. But the reference point does not have to be Y. If it is not, the ratio may exceed 100%. In this case, we refer to "relative depth doses".

$$P(d, W_m, F, h\nu) = 100 * \frac{D_X}{D_Y}$$

Equation B-3

INVERSE SQUARE LAW (I):

Doses at X' and Y' will be related inversely as the square of their distances from the source. Provided there is no attenuating or scattering material between or near them, and the source dimension is small compared to the SSD distance.

$$I(F, d, d_m) = \frac{D_{X''}}{D_{Y'}} = \left(\frac{SSD + d_m}{SSD + d} \right)^2$$

Equation B-4

Notice that the central portion of Figure B-1 contains a bold rectangle. This is used to relate the various quantities, discussed above, to one another. In fact, we can define relationships between B, Ta, P and I as follows. Going clockwise around the rectangle:

$$D_X = D_{Y'} * B * P$$

And going counter clockwise:

$$D_X = D_{Y'} * I * Ta$$

Dividing these two expressions will provide us with a method of expressing the percent depth dose:

$$P(d, W_m, F) = \frac{100 * Ta * I}{B} * \left(\frac{SSD + d_{max}}{SSD + d} \right)^2$$

Solving for the tissue air ratio term, Ta:

$$Ta = \frac{P(d, W_m, F)}{100} * \frac{1}{I} * \left(\frac{SSD + d}{SSD + d_m} \right)^2 * B$$

Equation B-5

Recall that Target does not store $P(d, W_m, F)$ values, but it does store $P(d, W_0, F)$. If we were to use $P(d, W_0, F)$ instead of $P(d, W_m, F)$, we can use the data already stored in the Target software to generate TAR values. Strictly speaking, the Target data should be corrected for the variation in field size between the these two values. However, the Target designers have not done so, believing that the error introduced as a result of not making these corrections is small.

Previously we have defined the percentage depth dose at a specific SSD and depth below the water surface, d , in terms of an infinite SSD as:

$$DD(SSD, d) = DD(\infty, d) * \left(\frac{SSD + d_m}{SSD + d} \right)^2 = DD(\infty, d) * I$$

Equation B-6

Hence, if we substitute $DD(SSD, d)$ for $P(d, W_m, F)$, we find that:

$$T_a = \frac{DD(\infty, d) * I}{100} * \frac{1}{I} * \left(\frac{SSD + d}{SSD + d_m} \right)^2 * B$$

$$T_a = \frac{DD(\infty, d)}{100} * \left(\frac{SSD + d}{SSD + d_m} \right)^2 * B$$

Equation B-7

Also, the d_{max} CAX value, defined to be 100, is expressed in Target as:

$$DD(\infty, d) * I = 100 * I = DD(SSD, d)$$

Therefore, the expression for T_a can be simplified as:

$$T_a = \frac{DD(d)}{DD(d_{max})} * B$$

Equation B-8

If TAR values are required for points that lie within the build up region of the various boundaries between materials, problems will result due to the lack of central axis depth dose information that is available in the Target data files for buildup regions. In this case, the same cubic interpolation method is employed in a similar manner as was presented in section 3.1 for the determination of the CAX value within the build up region.

APPENDIX C: GLOSSARY

Beam Penumbra:

As far as beam profiles are concerned, the penumbra is defined as the horizontal distance between two reference dose values. The distance is either between the 90% and the 10% values, or between the 80% and 20% values.

Beam Profile:

A beam profile consists of the relative dose distribution along a line that is perpendicular to the beam central axis.

Central Axis of a beam:

The central axis of a beam is the ray that extends from the effective point source through the machine isocenter.

Central Plane of a beam:

The central plane of the beam is defined as any plane containing the beam central axis.

Coplanar Beams:

Beams that have central axes that lie in the same plane are defined to be coplanar.

MU:

MU is an abbreviation for Monitor Unit. The monitor unit is defined for individual linacs. At the Vancouver Island Cancer Centre, the linacs have been calibrated so that 1 MU will deliver 1 cGy to the d_{max} point in a water phantom for a 10 cm x 10 cm field size.

Open Field Isodoses:

These are isodose curves (lines of equal energy deposited per unit mass) that result from a rectangular field that has not been altered by the presence of beam shaping devices such as blocks and/or wedges.

APPENDIX D: COPYRIGHT PERMISSION

THE UNIVERSITY OF TEXAS
MD ANDERSON
CANCER CENTER

CONFIDENTIAL FACSIMILE
Transmission Cover Sheet

DATE: November 3, 1995

TO: Mr. Gregory Gallant

LOCATION: Department of Medical Physics
Vancouver Island Cancer Center

FACSIMILE #: (604) 370-8697

FROM: Dr. John A. Antolak

LOCATION: M.D. Anderson Cancer Center
Radiation Physics - Box 94
1515 Holcombe, Houston, Texas 77030

FACSIMILE #: (713) 794-5272

MEMO:
See attached.

We are transmitting 2 pages, including the cover sheet. If you do not receive the entire transmission, please call the person sending the transmission at telephone number: (713) 792-3292.

Confidential Notice

THE DOCUMENTS ACCOMPANYING THIS FACSIMILE TRANSMISSION CONTAIN CONFIDENTIAL INFORMATION BELONGING TO THE SENDER. THE INFORMATION IS INTENDED ONLY FOR THE USE OF THE INDIVIDUAL OR ENTITY NAMED ABOVE. IF YOU ARE NOT THE INTENDED RECIPIENT, YOU ARE HEREBY NOTIFIED THAT ANY DISCLOSURE, COPYING, DISTRIBUTION OR THE TAKING OF ANY ACTION IN RELIANCE ON THE CONTENTS OF THIS FACSIMILED INFORMATION IS STRICTLY PROHIBITED. IF YOU HAVE RECEIVED THIS FACSIMILE IN ERROR, PLEASE NOTIFY THE SENDER BY TELEPHONING IMMEDIATELY TO ARRANGE FOR RETURN OF THE ORIGINAL DOCUMENTATION.

THE UNIVERSITY OF TEXAS
MD ANDERSON
CANCER CENTER

November 3, 1995

Department of Radiation Physics - 94
(713) 792-3292
(713) 794-5272 FAX

Mr. Gregory Gallant
Department of Medical Physics
Vancouver Island Cancer Center
1900 Fort Street
Victoria, BC, V8R 1J8, Canada

FAX: (604) 370-8697

Dear Gregg,

This letter is regarding your recent request to use a figure from my Ph.D. thesis in an appendix of your thesis.

The figure in question was figure I.3, page 6 of "Electron Beam Treatment Planning", a thesis I submitted to the University of Alberta in 1992. Please consider this letter to be your official permission to use figure I.3 in your thesis.

Sincerely yours,

A black rectangular redaction box covers the signature area, obscuring the name and any handwritten notes.

John A. Antolak, Ph.D.
Assistant Physicist

JAA:par

VITA

Surname: Gallant

Given Names: Gregory Allen

Place of Birth: Winnipeg, Manitoba, Canada

Educational Institutions Attended:

University of Victoria 1994 to 1995

University of Alberta 1989 to 1993

Grande Prairie Regional College 1988 to 1989

Degrees Awarded:

B. Sc. (Engineering Physics) University of Alberta 1993

Honours and Awards:

G.E. Research Grant 1994-95

Publications:

Experimental Validation of Dose Distributions Predicted
by a Treatment Planning System for Complex Models in preparation

Presentations:

<u>Title</u>	<u>Audience</u>	<u>Date</u>
ICRU 50: Prescribing, Recording, and Reporting Photon Beam Therapy	Vancouver Island Cancer Centre: Physics Department	1994
Paris System of Brachytherapy Dosimetry	Vancouver Island Cancer Centre: Physics Department	1995
MATLAB: A mathematical package that can be used in conjunction with treatment planning systems	Western Canadian Medical Physics Conference (Wescan '95)	1995

Supplementary Courses:


Radiation Transport Calculations using the EGS4 Monte Carlo System (Seattle, WA) 1995

PARTIAL COPYRIGHT LICENSE

I hereby grant the right to lend my thesis to users of the University of Victoria Library, and to make single copies only for such users or in response to a request from the Library of any other university, or similar institution, on its behalf or for one of its users. I further agree that permission for extensive copying of this thesis for scholarly purposes may be granted by me or a member of the University designated by me. It is understood that copying or publication of this thesis for financial gain shall not be allowed without my written permission.

Title of Thesis:

Experimental Validation of Dose Distributions Predicted by a Treatment
Planning System for Complex Models

Author: 

Gregory Allen Gallant

27 November, 1995